Bulletin of Romanian Chemical Engineering Society

2 2024

ISSN 2360-4697
Edited by SICR and Matrix Rom
The journal is included in the international database
EBSCO, PROQUEST & INDEX COPERNICUS

ISSN 2360-4697

Bulletin of Romanian Chemical Engineering Society

Volume 11 2024 Number 2

Contents

Iulia-Maria MIRCEA, Gheorghe BUMBAC, Romuald GYŐRGY, Ionut BANU, *1,4-Butanediol synthesis from maleic anhydride – Process analysis*…….2

Iulian BERLADEAN, Irina CÂRLESCU, Yahia BOUSSOUALEM, Abdelylah DAOUDI, Nicolae HURDUC, *Influence of fluorine lateral substitution on photoisomerization process of azobenzene bent-core liquid crystals*……23

Diana HANGANU, Lidia FAVIER, Maria HARJA, *Methods for antibiotics removal: a comprehensive analysis*……...28

Laura NISTOR, Ramona-Elena TATARU-FARMUS, Maria HARJA, *Current researches for organic compounds removal using $BiFeO_3$* ……..38

Eliza-Gabriela MIHĂILĂ (BRETTFELD), Tănase DOBRE, Daria Gabriela POPA, Diana CONSTANTINESCU-ARUXANDEI, Florin OANCEA, *Enhanced carbon capture and biofixation using functionalized deep eutectic solvent and Desmodesmus Communis microalgae*……44

Iuliana CRISTEA, Timur CHIS, Laurențiu PRODEA, *Use of hydrogen mixed with natural gas in industrial and local networks*…….52

Laura PETRAS, Claudia KONCSAG, Oana Cristina PÂRVULESCU, Tănase DOBRE, Iuliana DELEANU, Cristian Eugen RĂDUCANU, *Effect of Axial Mixing in Modelling of Three Phases Steady State Gasoline Hydrofining*……...62

Alla ZEINAB, Sulaiman Khasro Hamza DZAIY**,** Timur CHIȘ, Laurentiu PRODEA, *The effect of acid to natural gas storage rocks*……68

Reem Sabah MOHAMMED, Timur CHIȘ, Dumitru CHISĂLIȚĂ, *Laboratory analysis of oilfield produced water extraction from emulsions*…….82

David NECULA, Nicolae PANAINTE, Ancaelena STERPU, *Effect of temperature and emulsifier dosage on water separation from crude oil emulsion*…….93

1,4-BUTANEDIOL SYNTHESIS FROM MALEIC ANHYDRIDE – PROCESS ANALYSIS

Iulia-Maria MIRCEA[1], Gheorghe BUMBAC[1], Romuald GYŐRGY[1], Ionut BANU[1*]

[1]National University of Science and Technology POLITEHNICA Bucharest, Faculty of Chemical Engineering and Biotechnologies, Department of Chemical and Biochemical Engineering, 1-7 Gh. Polizu, 011061, Bucharest, Romania

Abstract

This paper presents the results of the conceptual design of the process of obtaining 1,4 butanediol from maleic anhydride, obtained based on process modeling and simulation techniques. The production capacity considered in the presented case study was 70,000 t/yr of 1,4 butanediol. In the reaction system proposed for this process, for the intermediate hydrogenation reaction of γ-butyrolactone, it was decided to use two reaction steps, each based on a tubular reactor with solid granular catalyst. Mass and heat balances were performed using the Aspen Plus v10 process simulator, and the main equipment characteristics, as well as the cold and hot utilities amounts were determined and used to estimate the production price for the main products (1,4-butanediol) and the purified by-products. Comparing the predicted production price of 2 EUR/kg with the market price of 5 EUR/kg, the proposed flowsheet is deemed economically feasible.

Key words: 1,4-butanediol, maleic anhydride, gas-solid reactor, extractive distillation, pressure swing distillation.

1. Introduction

1,4-butanediol (1,4-BDO) is widely used in different industrial fields as medicine, textile, paper making, chemical industry as well as medicine [1]. It is usually used as a feedstock for polyesters, polyurethanes and polyethers manufacturing [2]. Many basic chemicals with several used in industrial practice (as tetrahydrofuran-THF, γ-butyrolactone-GBL, polybutylene terephthalate) are currently produced using 1,4-butanediol as raw material [3]. Among these, γ-butyrolactone is used as a solvent, as an alternate solvent to trichloroethane, which is a chemical with greenhouse effect, by destroying the ozone layer [4]. THF can be used as raw material for the manufacturing of spandex, polyether elastomer and thermoplastic polyurethane [1]. There are several routes to obtain 1,4-BDO, both chemical and biochemical. One of the more recent biochemical approaches relies on the conversion of renewable carbohydrate feedstocks to 1,4-BDO. Genomatica company obtained BDO from glucose, xylose, fructose and biomass-derived sugar streams using genetically modified *Escherichia coli* [3, 5]. Another one is based on

Corresponding author email address: ionut.banu@upb.ro

chemical transformation of maleic anhydride and other fossil resources chemicals. Among the main process licenses can be mentioned: (a) Reppe (relying on formaldehyde and acetylene condensation); (b) Arco (isomerization of propylene oxide to allyl alcohol and its further hydroformylation); (c) Mitsubishi Kasei (implementing 1,3-butadiene diacetoxylation); (d) Davy McKee (hydrogenation of diethyl and dimethyl maleates) or its BP alternative which is directly hydrogenates maleic anhydride [6]. In comparison to butadiene acetoxylation with acetic acid followed by hydrogenation, the hydrogenation of maleic anhydride (MA) is the most direct way to manufacture GBL, THF and 1,4-BDO which does not require hazardous compounds (i.e. acetylene) [6, 7]. According to the study of Satam et al. [7] the global market of 1,4-BDO was over 6 billion USD in 2019 and is estimated to grow up to 12 billion USD by 2025. The growth is attributed to the use of spandex in textiles, accounted for 50 % of the market at the level of year 2015. According to the economic reports maleic anhydride consumption in 1,4-BDO and unsaturated polyesters resins applications is going to increase its demand in the following years. The 1,4-BDO production capacity in the Asia Pacific region is currently about 3.2 MT and is expected to surpass 5.5 MT by the year 2032 [8].

To develop an efficient process for maleic anhydride conversion to value added chemicals a proper selection of a catalyst should be carried out. One of the first studies regarding MA hydrogenation was reported by Kanetaka et al. [9] over a nickel-ruthenium catalyst supported on kieselguhr. The authors analyzed the hydrogenation of MA as well as other intermediaries (succinic anhydride-SA, γ-butyrolactone, succinic acid, 1,4-BDO) and evidenced that the secondary reactions produced small quantities of lower organic acids (propionic acid, butyric acid). Another catalysts proposed in the literature was based on a Copper zinc-alumina mixture. Küksal et al. [10] shown that using this catalyst, the complete conversion of MA and SA took place and, for a temperature of 543 K, pressure 8.5 MPa and a GHSV of 10169 h^{-1}, there were obtained yields above 40 % for γ-butyrolactone and above 33 % for 1,4-BD. In a series of studies, Herrmann and Emig [11] investigated the liquid phase hydrogenation of MA and intermediates on copper-based and noble metal catalysts [11-13]. According to their results, hydrogenation of succinic anhydride proceeded with high selectivity to GBL and 1,4-BDO on copper zinc catalyst, whereas other copper catalysts (having spinel structure) had no or limited activity in the formation of 1,4-BDO [11]. The authors developed power law kinetic models for MA and SA hydrogenation, whereas 1,4-BDO and GBL hydrogenation were undergone following a LHHW kinetics.

In the present study, a process for manufacturing 1,4-BDO from maleic anhydride raw material was proposed. The conversion of maleic anhydride towards 1,4-BDO took place in two steps. The first step was carried out in a fixed-bed catalytic reactor with hydrogen in gas phase and maleic anhydride solubilized in a proper solvent to bring it in gas phase. The second step, specific for the present

process, consists in the realization of the GBL hydrogenation reaction towards 1,4-BDO in a fixed bed reactor where the reaction mixture was in gas phase. The behavior of the second reactor was analyzed both at the catalyst pellet and bed level. The process was simulated in Aspen Plus commercial simulator and its economic feasibility emphasized based on the simulated data.

2. Stoichiometry, kinetics and thermodynamics of 1,4-BDO synthesis

The 1,4-butanediol production plants typically use a catalytic fixed-bed hydrogenation reactor with two fluid phases (hydrogen in gas phase and raw-materials and reaction products in liquid phase) (further referred as to gas-liquid-solid-G-L/S- reactor) or a catalytic fixed-bed reactor with the reactants/products in gas phase (referred as gas-solid-G/S-reactor). According to the study of Herrmann and Emig [13], the hydrogenation of MA to 1,4-BDO and GBL is taking place in a gas-liquid-solid reactor according to stoichiometry presented in **Fig. 1**. Maleic to succinic anhydride, as well as the conversion of the latter to GBL are reactions occurring with high selectivity towards GBL [11]. Given the lack of a reliable kinetic model for these transformations, selectivities in the GBL, 1,4-BDO and THF from the published literature were taken into account in our study [10].

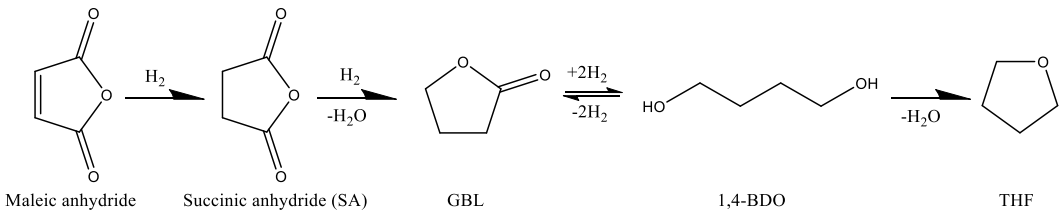

Fig. 1. Reactions taking place in the G-L/S reactor [13]

The conversion of GBL to 1,4-BDO and other by-products can be carried out both in a G-L/S reactor or a G/S reactor. The study reported by Gautier et al. [14], mention that the gas-phase GBL hydrogenation takes place according to the stoichiometry given in **Fig. 2**. According to these reactions, apart from the 1,4-BDO main product, there are produced THF and n-butanol (BuOH) as by products. The operating conditions implemented in this study for the G/S reactor are: a pressure above 35 bar, a GBL to H_2 molar ratio of 1/60, and a reaction temperature of 240°C.

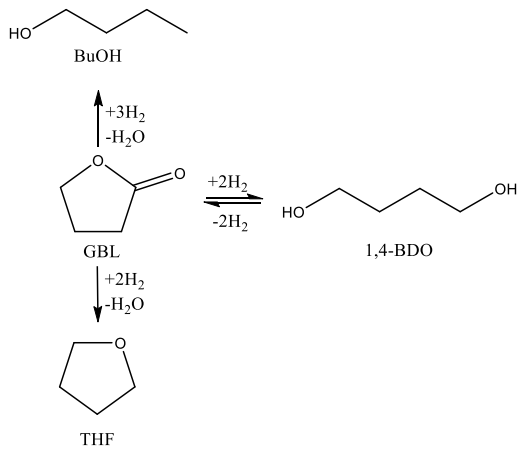

Fig. 2. GBL hydrogenation reactions taking place in G/S reactor [14]

GBL hydrogenation kinetics

The kinetic model for the reaction carried out over a Cu-Zn/Alumina catalyst, with the fluid in gas-phase, used in our study, was developed by Gautier et al. [14]. Their experimental study was performed in operating conditions in which the physical steps influence on the chemical process are negligible. The rate expressions for each compound are given by relations (1)-(4):

$$v_{r,GBL} = k \cdot \left(\frac{1}{K_{eq}} \cdot y_{BDO} \cdot (1-a)^4 - y_{GBL} \cdot a^4 \right) - k_{sp} \cdot y_{GBL} \tag{1}$$

$$v_{r,BDO} = k \cdot \left(y_{GBL} \cdot a^4 - \frac{1}{K_{eq}} \cdot y_{BDO} \cdot (1-a)^4 \right) \tag{2}$$

$$v_{r,BuOH} = \frac{k_{sp}}{2} \cdot y_{GBL};\ v_{r,THF} = \frac{k_{sp}}{2} \cdot y_{GBL} \tag{3}$$

$$v_{r,H_2} = 2 \cdot v_{r,BDO} + 3 \cdot v_{r,BuOH} + 2 \cdot v_{r,THF};\ a = \frac{\sqrt{K_{H_2} \cdot P_{H_2}}}{1 + \sqrt{K_{H_2} \cdot P_{H_2}}} \tag{4}$$

where: y_j – gas-phase molar fraction of compound j (j=GBL, THF, BuOH, BDO); P_{H2} – hydrogen total pressure, bar; k – rate constant for hydrogenation of GBL to BDO, s^{-1}; k_{sp} – rate constant for side reactions, s^{-1}; K_{H2} – adsorption constant for hydrogen on the catalyst, bar.

One aspect that needs to be considered in the separation section is that the mixture in liquid phase presents several azeotrope points, detected both at atmospheric pressure and in vacuum conditions (0.1 atm). The characteristics of the azeotrope points were evaluated using Aspen Plus v10 and are given in Table 1.

According to the solution proposed by Xu and Wang [15], separation of THF from its azeotropic mixture with water can be performed by extractive distillation, using 1,2-propanediol as an entrainer. Another issue in the separation of the complex mixture resulting in the BDO synthesis from maleic anhydride is the separation and recovery of BuOH from its mixture with water. In our work, the two-distillation columns and an intermediary decanter solution proposed by Luyben [16] was implemented. It's important to emphasize that, according to this separating solution, no additional third component, such as a light entrainer or extracting solvent, is required in the separation of the n-butanol/water heterogeneous azeotropic binary mixture.

Table 1

Azeotropes between components in liquid phase

N°	Pressure, atm	Temperature, °C	Azeotrope type	Molar fractions				
				GBL	THF	BDO	H_2O	BuOH
1	1	201.5	Homogeneous	0.827	0	0.173	0	0
2	1	63.4	Homogeneous	0	0.829	0	0.171	0
3	1	91.6	Homogeneous	0	0	0	0.765	0.235
4	0.1	127.1	Homogeneous	0.986	0	0.014	0	0
5	0.1	42.5	Homogeneous	0	0	0	0.788	0.212

3. Design and analysis of the G/S hydrogenation reactor (R-2)

In our proposed process, the MA hydrogenation is carried out in two steps, one in a fixed-bed G-L/S reactor where a high amount of GBL is obtained, and a second step where GBL is hydrogenated in a G/S reactor towards 1,4-BDO, in which THF and BuOH are obtained as by-products. Given the availability of a kinetic model for the G/S reaction process, in this paragraph the GBL G/S hydrogenation reaction was analyzed both at the catalyst particle and catalyst bed level, using the kinetic model proposed by Gautier et al. [14].

Evaluation of GBL hydrogenation at the catalyst particle scale

Temperature and pressure used as operating conditions in process modeling were in the specific ranges established for G/S GBL hydrogenation over the Cu-Zn/alumina catalyst. Equation (5) together with the boundary conditions (6) describes the mass balance of compound "j" in a chemical process occurring in a steady-state regime inside a spherical catalyst particle:

$$\frac{1}{r^2}\frac{d}{dr}\left(r^2 \cdot N_j\right) - v_{r,j} \cdot \rho_p = 0 \tag{5}$$

$$r = R_p, C_j = C_{j,s};\ r = 0,\ \frac{dC_j}{dr} = 0 \tag{6}$$

Expressing the diffusion flux, N_j, by Fick's law, the equation (7) takes the form:

$$\frac{1}{r^2}\frac{d}{dr}\left(r^2 \cdot D_{ef} \cdot \frac{dC_j}{dr}\right) - v_{r,j} \cdot \rho_p = 0 \tag{7}$$

These higher-order differential equations have been transformed into a system of ordinary differential equations with boundary conditions solved using the "bvp5c" function from the MATLAB programming environment.

The effective diffusion coefficient was evaluated by relation (8):

$$D_{ef} = \frac{\varepsilon_p}{\tau} \cdot D_{AB} \tag{8}$$

in which the molecular diffusion coefficients were calculated by Fuller correlation (9) [17]:

$$D_{AB} = \frac{0,00143 \cdot T^{1,75}}{P \cdot M_{AB}^{1/2} \cdot \left[V_A^{1/3} + V_B^{1/3}\right]^2} \tag{9}$$

where D_{AB} - binary diffusion coefficient, cm^2/s; T - temperature, K; M_{AB}, average molecular weight of compounds A and B, g/mol; P- pressure, bar; V_A, V_B - molar volumes of the components A/B; ε_p - porosity of the catalyst pellet, and τ - tortuosity factor.

The simulation of the process behavior at the catalyst particle scale was evaluated using the data in Table 2. Following the solution of the equations, concentration profiles within the granule were obtained for the chemical species involved in the process and presented in Fig.3. The results show that the reactants evolution inside the catalyst particle decreases from the surface towards the center of the spherical particle whereas the concentration of products that are formed inside the particle are increasing in the opposite direction.

Table 2

Catalyst pellet simulation data

Variable	**Value**	**References and observations**
Temperature, T, °C	240	[18]
Pressure, P, bar	35	[18]
GBL/H_2 molar ratio	1/60	[18]
Catalyst pellet radius, R_p, m	$2\cdot10^{-3}$	Proposed value
Catalyst pellet porosity, ε_p	0.3	Gautier et al. [14]
Tortuosity factor, τ	3	Gautier et al. [14]
Surface GBL concentration, mol/L	$9.5\cdot10^{-3}$	Proposed value
Surface hydrogen concentration, mol/L	0.85	Proposed value

In order to take into account, the influence of the internal diffusion one can use the effectiveness factor, calculated by equation (10):

$$\eta_i = \frac{\overline{v_{RA}}}{v_{RA}} \tag{10}$$

Where the average reaction rate inside the spherical particle is evaluated by:

$$\overline{v_{RA}} = \frac{n_A}{V_g} = \frac{3}{R_p} \cdot D_{ef} \cdot \left(\frac{dC_A}{dr} \right)_{r=R_p} \tag{11}$$

where $\overline{v_{RA}}$ -average reaction rate, m/s; v_{RA} - reaction rate of reactant A at the particle's surface, m/s; R_p - particle radius, m; D_{ef} -diffusion coefficient, m/s.

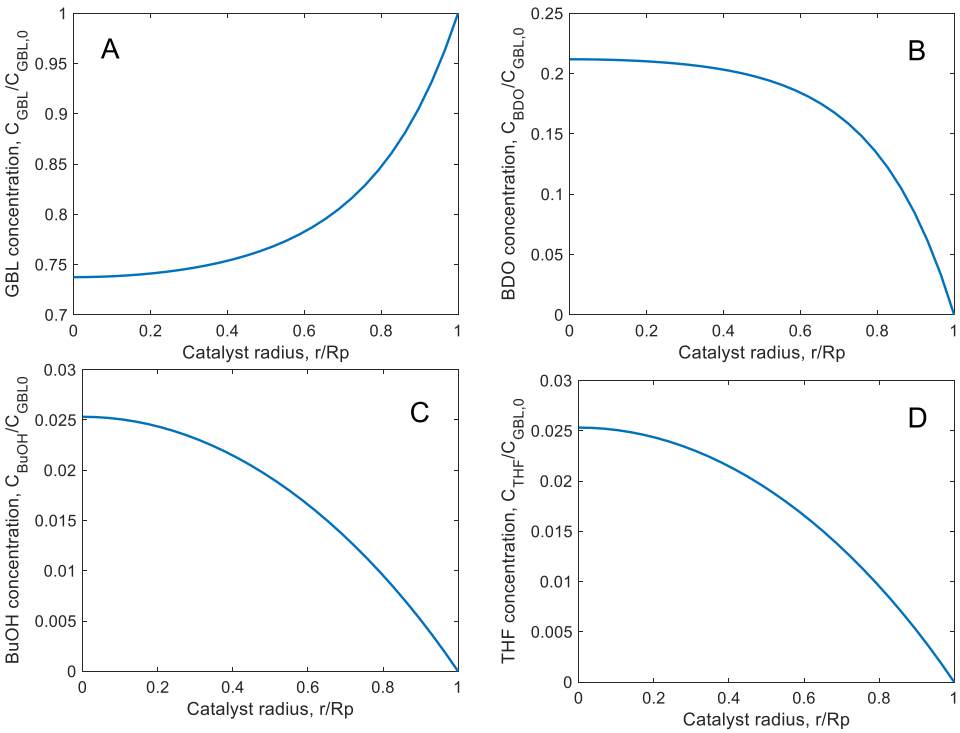

Fig. 3. Profile of chemical compounds concentrations in the catalyst pellet (A – GBL; B – BDO; C – BuOH; D – THF)

The effect of particle size and geometry is essential for the catalytic reactor design, because visualizing the concentration profiles is of utmost importance for understanding the chemical process steps in relation with the catalyst selection [19]. The values of the effectiveness factors calculated by solving the mass balance equations (5) and presented in Table 3, show that this physical phenomenon has an important influence on the process kinetics in the GBL hydrogenation step, and consequently it needs to be taken into account in analyzing the process behavior at the level of the catalyst bed.

Table 3

Calculated effectiveness factors for different catalyst particle sizes

№	**Chemical compound**	**Effectiveness factor, η_j**		
		Catalyst pellet radius, m		
		$1\cdot10^{-3}$	$2\cdot10^{-3}$	$3\cdot10^{-3}$
1	GBL	0.71	0.46	0.34
2	BDO	0.69	0.44	0.31
3	BuOH	0.93	0.86	0.82
4	THF	0.93	0.86	0.82
5	H_2	0.71	0.46	0.34

Evaluation of GBL hydrogenation at the level of catalyst bed

Modeling the GBL hydrogenation reactor involves describing the behavior of both media within the reactor: the process gas phase and solid catalyst. Considering the results presented by Gautier et al. [14], and keeping a WHSV value similar with the experimental one (t_{mV} =0.96 (g · s)/cm^3), a required catalyst weight of 21 t was determined. The G/S reactor model was developed considering the following hypotheses: negligible axial mixing (bed length/catalyst particle diameter > 50 [20]) plug-flow behavior in terms of fluid flow, isothermal operation and isothermal catalyst particle, ideal behavior of the gas phase, constant pressure through the bed and the operating parameters were taken in order to cover the range of the experimental study considered by Gautier et al. [14]. The catalyst particle radius in the present study was $2 \cdot 10^{-3}$ m. The mass balance for the reactor is characterized by equations (12) in which a plug-flow pseudo-homogeneous behavior was considered:

$$\frac{dD_{Mj}}{dV} = v_{Rj}, V = 0, D_{Mj} = D_{Mj,0} \tag{12}$$

The mathematical model of the reactor consists in a system of ordinary differential equations integrated by MATLAB function ode15s. The simulation results are presented in Fig. 4. The GBL conversion increases up to 26 % at the reactor outlet, with a 1,4-BDO yield of 21.9 %. These values suggest that the impact of side reactions on the process behavior is relatively low, the BuOH yield being about 2 %. Another aspect that must be emphasized is the relatively low value of GBL effectiveness factor all along the reactor length (0.46-0.51), stressing that in this type of processes the internal diffusion have to be taken into account.

4. Modeling and simulation of 1,4-BDO synthesis process

In the present study was developed a process flowsheet for the 1,4-BDO synthesis with a production capacity of 70,000 tons. The proposed process entails the hydrogenation of maleic anhydride towards mainly GBL within a G-L/S reactor, operating at 240°C and 75 bar pressure, over a Cu-Zn/Alumina catalyst, as per Herrmann's data [21]. A second reaction step was the GBL hydrogenation to 1,4-BDO in a G/S reactor. This process's appeal lies in its efficiency and adaptability, enabling the simultaneous production of γ-butyrolactone, 1,4-butanediol, tetrahydrofuran, and butanol.

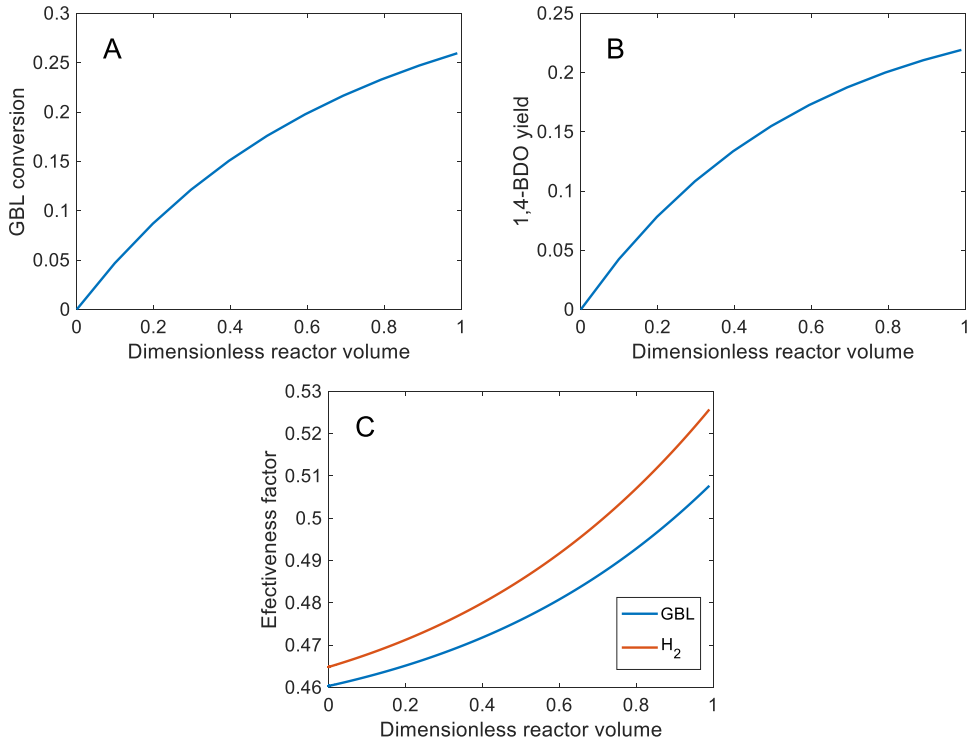

Fig. 4. GBL conversion (A), BDO yield (B) and profiles of effectiveness factor (C) in the hydrogenation reactor.

Process description

In the case of the maleic anhydride hydrogenation process in a G-L/S reactor, according to the study published by Küksal [22], by modifying the reaction conditions, a mixture predominantly consisting of GBL, 1,4-BDO and THF is obtained. The proposed process flowsheet is shown in **Fig. 5**.

Di-n-butyl adipate, hereafter referred to as dibutyl adipate, is a suitable solvent for maleic anhydride [23]. Therefore, maleic anhydride is highly soluble in dibutyl adipate, which is used in this process to solubilize the raw material before the reaction step. The resulting feed from mixing operation (A-1) is fed into the G-L/S hydrogenation reactor. Hydrogen is fed at ambient temperature in the compression step and brought to the required operating conditions (temperature and pressure). The reaction mixture from R-1 hydrogenation reactor is introduced into a gas-liquid separator, where hydrogen is recovered and recycled.

Given the previously mentioned aspects, the mixture obtained in the G-L/S first step hydrogenation is subsequently separated into a series of rectification columns. In rectification column C-1, the THF-water azeotrope is separated at the

top of the column, and the mixture of γ-butyrolactone, 1,4-butanediol, and dibutyl adipate is separated at the bottom. For dibutyl adipate solvent recycling purposes, its recovery operation is carried out in C-2 at vacuum to significantly reduce the boiling temperatures of the involved compounds. The solvent obtained at the top of the column is recycled, while the azeotrope GBL-1,4-BDO is fed to column C-3. A pressure of 0.1 bar is used for this separation to ensure the quality standard of the main product: 99.5 % 1,4-BDO.

A significant amount of γ-butyrolactone is obtained, which is fed into the second step of the hydrogenation reaction in a G/S reactor to be further converted into the desired product, 1,4-butanediol, with the formation of secondary products such as THF, butanol, and water. The gas-phase hydrogenation reaction occurs in the R-2 G/S reactor at 240°C and 40 bar with a GBL/H_2 ratio of 1/60, over a Cu-Zn/Alumina catalyst [18]. Subsequently, the reaction mixture passes into G/L flash separation unit (F-2) from where the recovered hydrogen is recycled to the gas-phase hydrogenation operation. The liquid mixture flow is introduced into C-4 rectification column where a THF-water-butanol mixture is separated and fed into the THF purification section. The resulting γ-butyrolactone and 1,4-butanediol are recycled back to C-3 where purified 1,4-BDO is obtained and a portion of GBL is separated as the final product.

The THF-water-butanol mixture is fed into C-5 rectification column along with 1,2-propanediol, which is an extraction solvent as it removes water from the mixture undergoing separation. At the top of the column, 99% pure THF is separated, while at the bottom, 1,2-propanediol with water and butanol are recovered [15, 24].

In the rectification column C-6, the solvent is recovered and recycled to the extractive distillation, while the butanol-water mixture is fed into the butanol separation section. In the C-7 column, a small water flow is removed according to the azeotrope concentration in a column that operates without its own condenser (there is a common condenser for both the vapors from the top of C7 and for the vapors from the top of C8), and the still-diluted butanol solution is introduced into a decanter (D-3) that separates an upper (light liquid phase) phase of concentrated butanol solution sent as reflux in C-8 and a water phase with a small amount of butanol (heavy liquid phase) which is recycled as a reflux stream to C-7. The concentrated butanol solution from the decanter is further refined into C-8 rectification column, where butanol is separated from water, obtaining butanol as the end product with a purity of 99% [25].

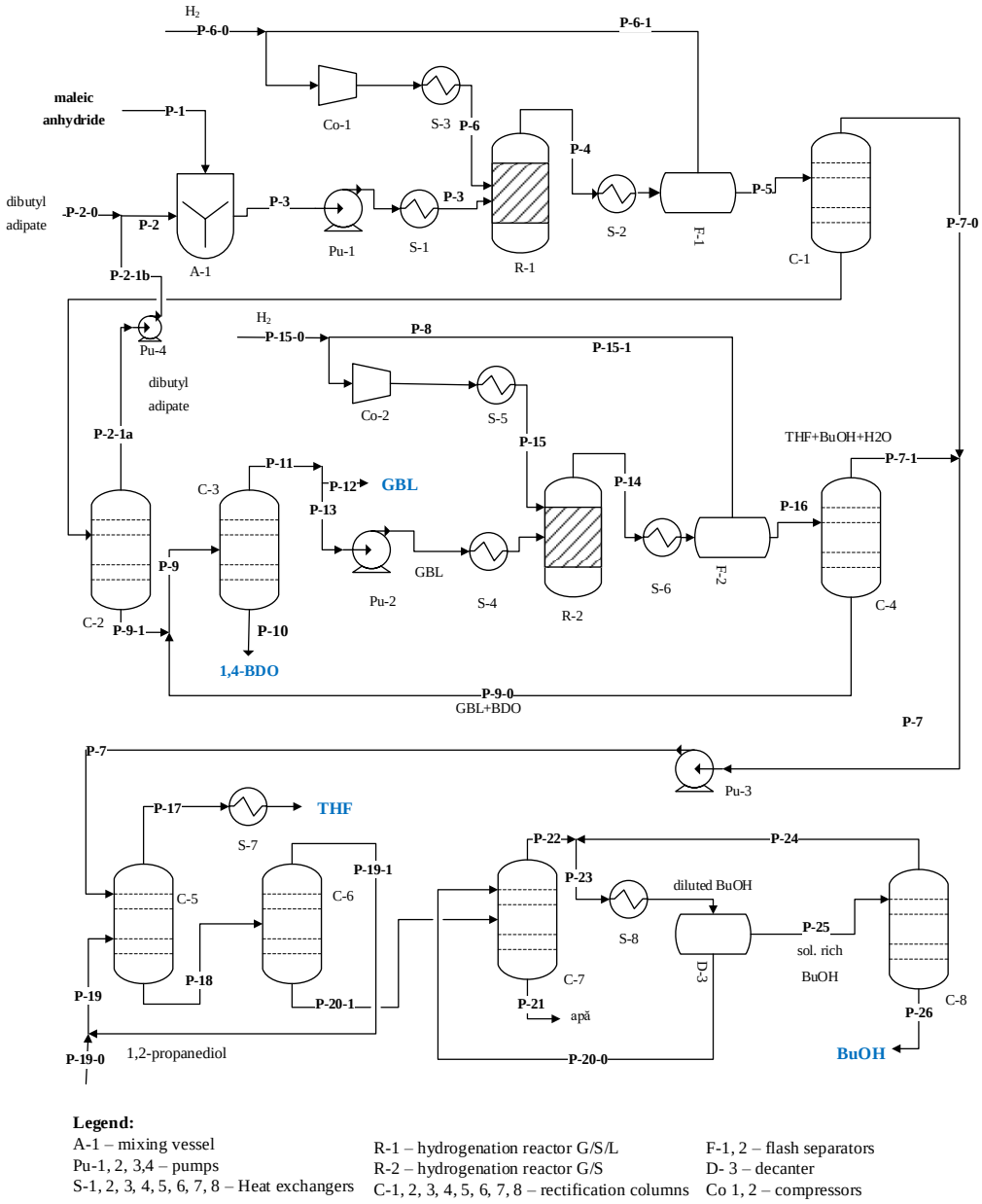

Legend:

A-1 – mixing vessel
Pu-1, 2, 3,4 – pumps
S-1, 2, 3, 4, 5, 6, 7, 8 – Heat exchangers
R-1 – hydrogenation reactor G/S/L
R-2 – hydrogenation reactor G/S
C-1, 2, 3, 4, 5, 6, 7, 8 – rectification columns
F-1, 2 – flash separators
D- 3 – decanter
Co 1, 2 – compressors

Fig. 5. The process flowsheet for 1,4-butanediol production

Mass balance

The mass balance is presented by dividing the plant into three sections: the Reaction section 1, Reaction section 2, and By-products separation section.

Reaction section 1 consists of the raw materials conditioning step and the first hydrogenation reactor (R-1), as well as the solvent recovery. In the G-L/S hydrogenation reactor, complete conversion of maleic anhydride is assumed. The product flow rates are determined using the selectivities of the products from literature [22], and the hydrogen flow rate is calculated using a molar ratio of maleic anhydride to hydrogen of 1:5.

Table 4

Mass balance for the Reaction section 1

Substances	**Input flows, kg/h**						
	P-3	***P-6***	***P-4***	***P-5***	***P-8***		
maleic anhydride	24588	0	0	0	0		
dibutyl adipate	24588	0	24588	24588	24588		
hydrogen	0	2509.8	660.76	0	0		
γ-butyrolactone	0	0.12	14485.9	14485.8	14484.9		
tetrahydrofuran	0	1.76	887.00	885.24	0		
1,4-butanediol	0	0.01	6327.5	6327.5	6327.5		
water	0	27.1	4765.6	4738.5	0		
	49176	2538.8	51714.8	51025.03	45400.41		
TOTAL input	199855						
	Output flows, kg/h						
	P-4	***P-6-1***	***P-5***	***P-7-0***	***P-8***	***P-2-1***	***P-9-1***
maleic anhydride	0	0	0	0	0	0	0
dibutyl adipate	24588	0	24588	0	24588	24563.4	24.588
hydrogen	660.8	660.8	0.00	0	0	0	0
γ-butyrolactone	14485.9	0.12	14485.8	0.87	14484.9	0.00	14484.9
tetrahydrofuran	887	1.76	885.2	885.24	0.00	0	0
1,4-butanediol	6327.5	0.01	6327.5	0.00	6327.50	0.00	6327.5
water	4765.6	27.1	4738.5	4738.5	0.00	0	0
	51714.8	689.80	51025.03	5624.60	45400.41	24563.41	20837.00
TOTAL output	199855						

Reaction section 2 consists of the conditioning of the feed for the second hydrogenation reactor, the hydrogenation phase, and the separation of the desired product (1,4-BDO). The characteristics for each stream are shown in Table 5.

Table 5

Mass balance for the Reaction section 2

Substances	**Input flows, kg/h**						
	P-9-1	***P-9-0***	***P-13***	***P-15***	***P-14***	***P-16***	
dibutyl adipate	24.588	0	0	0	0	0	
γ-butyrolactone	14484.9	11064.7	14564	16.16	11080.9	11064.7	
1,4-butanediol	6327.50	3385.07	332.49	0.07	3385.14	3385.07	
butanol	0.00	6.21	3.54	7.11	261.71	254.61	
hydrogen	0	0	0	20461.66	20290.95	0	
tetrahydrofuran	0	0	0	53.13	297.37	244.24	
water	0	0	0	18.08	140.12	122.04	
	20837	14456	14900	20556.2	35456.19	15070.7	
TOTAL input	121276.1						
	Output flows, kg/h						
	P-11	***P-10***	***P-14***	***P-15-1***	***P-16***	***P-7-1***	***P-9-0***
dibutyl adipate	0	24.588	0	0	0	0	0
γ-butyrolactone	25526.55	23.10	11080.90	16.16	11064.74	0	11064.74
1,4-butanediol	582.75	9129.82	3385.14	0.07	3385.07	0	3385.07
butanol	6.21	0.00	261.71	7.11	254.61	248.40	6.21
hydrogen	0	0	20290.95	20290.95	0	0	0
tetrahydrofuran	0	0	297.37	53.13	244.24	244.24	0
water	0	0	140.12	18.08	122.04	122.04	0
	26115.52	9177.51	35456.2	20385.49	15070.7	614.6789	14456
TOTAL output	121276.1						

The by-products separation section consists of the purification of tetrahydrofuran and butanol. The characteristics for each stream are shown in Table 6.

Table 6

Mass balance for By-products separation section

Substances	**Input flows, kg/h**									
	P-7-1	***P-7-0***	***P-19***	***P-18***	***P-20-0***	***P-20-1***	***P-22***	***P-24***	***P-25***	
γ-butyrolactone	0	0.87	0	0.87	0.01	0.87	0.02	0	0.01	
tetrahydrofuran	248.4	0	0	248.4	84.2	248.4	332.6	79.7	328.08	
1,4-butanediol	244.2	885.24	0	0	0	0	0	0	0	
water	122.04	4738.5	0	4858.2	539.1	4858.2	539.7	61.02	61.62	
1,2-propanediol	0	0	5400	5397.7	0.03	5.4	0.05	0	0.02	
	614.7	5624.6	5400	10505.2	623.4	5112.9	872.4	140.7	389.7	
TOTAL input	29283.6									
	Output flows, kg/h									
	P-18	***P-17***	***P-19-1***	***P-20-1***	***P-22***	***P-21***	***P-20-0***	***P-25***	***P-24***	***P-26***
γ-butyrolactone	0.87	0	0	0.87	0.02	0.86	0.01	0.01	0.00	0.01
tetrahydrofuran	248.4	0	0	248.4	332.6	0.00	84.2	328.1	79.68	248.4
1,4-butanediol	0	1129.5	0	0	0	0	0	0	0	0
water	4858.2	2.3	0	4858.2	539.7	4857.6	539.1	61.62	61.02	0.6
1,2-propanediol	5397.7	2.3	5392.3	5.4	0.05	5.4	0.03	0.02	0	0.02
	10505.2	1134.07	5392.3	5112.9	872.4	4863.85	623.4	389.73	140.7	249
TOTAL output	29283.6									

Heat balance

In order to evaluate the proposed flowsheet from the economic point of view, the thermal balance was carried out for all equipment in the plant. The characteristics of cold and hot utilities used in our flowsheet were taken from the Aspen Plus v10 simulator. Thermal balances on the main heat exchangers in the plant are presented in Table 7, including data on thermal loads and heat transfer agents used.

Table 7

Heat balance of the heat exchangers

Heat exchanger	Type	Working fluid	$T_{in,a}$, K	$T_{ie,a}$, K	$P_{working\ fluid}$, bar	D_m, kg/s	D_a, kg/s	Q, kW
S-1	heating	silicone oil	280	250	1	13.66	35.4	2404.1
S-2	cooling	cold water 2	10	120	6	14.37	20.07	9630.3
S-3	heating	silicone oil	280	250	1	0.71	3.1	278
S-4 + S-5	heating	high pressure steam	250	250	40	9.85	7.4	12729.5
S-6	cooling	cold water 2	10	120	6	0.17	45.9	21421.7
S-8	cooling	cold water 1	10	30	1	0.07	5.8	489.7
S-7	cooling	cold water 1	10	30	1	0.315	0.26	23.8

where $T_{in,a}$ - inlet temperature of the working fluid, K; $T_{ie,a}$ - outlet temperature of the working fluid, K; $P_{working\ fluid}$ - pressure of the working fluid, bar; D_m - mass flow of process fluid, kg/s; D_a - mass flow of the thermal agent, kg/s; Q - heat duty, kW.

5. Economic evaluation

The economic evaluation for the proposed conceptual design unit plant for production of 1,4-butandiol as main product and tetrahydrofuran, γ-butyrolactone and butanol as secondary products was estimated using the Aspen Economic Evaluation facility from Aspen Plus v10 software.

The costs associated with a project can be broadly classified into two main categories: capital costs and operating costs. Capital costs encompass the expenses required for equipment, infrastructure, and construction, predominantly comprising fixed capital. These expenses include land acquisition, site development, design, equipment procurement, construction, and provisions for unforeseen circumstances. Additionally, working capital is essential to initiate production, covering costs for the initial months of operation. On the other hand, operating costs are directly linked to the ongoing operation of the project, primarily involving raw materials and energy utilities. They also encompass maintenance, labor, administrative expenses, and sales-related costs. Thus, while capital costs focus on the initial investments needed for construction and setup, operating costs revolve around the continual expenses associated with production and maintenance.

The utility costs were extracted from Aspen Plus v10 simulator and presented in Table 8.

Table 8

Utilities costs

Utility	Consumption	U.M.	Cost per hour	U.M.
Electricity	$1.08 \cdot 10^4$	kW	840.59	EUR/h
Cold water 1	$1.20 \cdot 10^4$	kW	9.14	EUR/h
Cold water 2	$3.08 \cdot 10^4$	kW	23.49	EUR/h
Cold water 3	$1.37 \cdot 10^4$	kW	10.46	EUR/h
Silicone oil	$1.55 \cdot 10^4$	kW	194.68	EUR/h
High pressure steam	$1.68 \cdot 10^4$	kW	151.35	EUR/h
Generation of low-pressure steam	$7.19 \cdot 10^4$	kW	-489.12	EUR/h
Low pressure steam	$8.93 \cdot 10^4$	kW	6.11	EUR/h
Medium pressure steam	$8.32 \cdot 10^4$	kW	659.08	EUR/h

The costs of the main equipment in the proposed flowsheet are shown in Table 9.

Table 9

The costs of main equipment

Equipment	Buying cost, EUR	Installation cost, EUR
C-1	$6.76 \cdot 10^5$	$1.13 \cdot 10^6$
C-2	$8.44 \cdot 10^5$	$1.73 \cdot 10^6$
C-3	$2.79 \cdot 10^6$	$5.65 \cdot 10^6$
C-4	$1.39 \cdot 10^5$	$3.42 \cdot 10^5$
C-5	$1.73 \cdot 10^5$	$3.51 \cdot 10^5$
C-6	$1.33 \cdot 10^5$	$3.76 \cdot 10^5$
C-7	$8.68 \cdot 10^4$	$2.49 \cdot 10^5$
S-2	$2.48 \cdot 10^5$	$4.58 \cdot 10^5$
S-6	$2.81 \cdot 10^5$	$4.57 \cdot 10^5$
S-8	$1.18 \cdot 10^4$	$6.65 \cdot 10^4$
S-7	$1.05 \cdot 10^4$	$6.39 \cdot 10^4$
S-3	$5.80 \cdot 10^4$	$1.93 \cdot 10^5$
S-4+S-5	$1.14 \cdot 10^4$	$1.50 \cdot 10^6$
F-1	$9.90 \cdot 10^4$	$2.32 \cdot 10^5$
F-2	$2.95 \cdot 10^4$	$1.19 \cdot 10^5$
TOTAL	$\mathbf{6.73 \cdot 10^6}$	$\mathbf{1.29 \cdot 10^7}$

For further analysis of economic feasibility, the market's prices for the raw materials and for the final products were extracted from internet sources and listed in Table 10.

Table 10

Prices for the raw materials and final products

Raw material/ Product	Price, $/kg	Reference
1,4-butanediol (1,4-BDO)	5	[26]
γ-butyrolactone (GBL)	5	[27]
tetrahydrofuran (THF)	6	[28]
butanol (BuOH)	1.5	[29]
maleic anhydride	1.3	[30]
hydrogen	2	[31]
1,2-propandiol	0.7	[32]
dibutyl adipate	2.5	[33]

In analyzing the components of previously assessed costs, the values obtained are presented in Table 11.

Table 11

Economic evaluation data

Total cost of capital, EUR	$4.61 \cdot 10^7$
Total cost of operation, EUR	$3.59 \cdot 10^8$
Total cost of raw materials, EUR	$3.16 \cdot 10^8$
Total sales, EUR	$8.97 \cdot 10^8$
Total equipment cost, EUR	$1.85 \cdot 10^7$
Total cost of installation, EUR	$2.88 \cdot 10^7$
Amortization period, an	10
Margin	$\mathbf{2.17 \cdot 10^8}$

Based on the data provided in Table 11, the production cost of the target products is assessed at 2 EUR/kg. A comparison of these values with their market selling price (approximately 5 EUR/kg for 1,4-butandiol and GBL) demonstrates the economic feasibility of the proposed process scheme.

6. Conclusions

In the present work it was developed a conceptual design study for the synthesis process of 1,4-butanediol, using maleic anhydride as raw material. Following an extensive literature review in the initial chapter, the technological sizing of an industrial facility for synthesizing 1,4-butanediol with a production

capacity of 70,000 tons per year was undertaken. One of the merits of the proposed process lies in its ability to yield secondary products, which, despite their formation, can be purified and marketed as finished goods (tetrahydrofuran, γ-butyrolactone, and butanol). Additionally, this process yields diminished quantities of residual streams, thereby aligning with several tenets of Green Chemistry [34]. Moreover, the process conserves atoms by maximizing the incorporation of raw materials into the final products through internal recirculation within the facility. The solvents employed, such as 1,2-propanediol, exhibit negligible toxicity and enhance safety, thereby adhering to the principles of a process in concordance with "green chemistry" principles.

In this process flowsheet, a subsequent integration of a gas-solid reactor for converting γ-butyrolactone to 1,4-butanediol led to a production capacity of 70,000 tons/year. The reactors used in the technological process were fixed-bed ones using a Cu-Zn/Alumina catalyst.

Employing the commercial simulator Aspen Plus v10, comprehensive mass and energy balances were performed for the entire facility. Based on these balances, the G/S reactor for the conversion of γ-butyrolactone to 1,4-butanediol was appropriately sized. The behavior of this reactor was analyzed both at the catalyst particle and bed level, and the results emphasized that internal diffusion is important. The performances of the GBL gas-solid hydrogenation reactor consisted in a γ-butyrolactone conversion of 25% and a 1,4-butanediol yield of 20%.

These elements collectively furnished the requisite data for the economic evaluation of the feasibility of the proposed process scheme, culminating in a production cost of finished products of 2 EUR/kg. Comparison with the market selling price of 1,4-BDO and GBL at 5 EUR/kg indicates the economic viability of the proposed process scheme.

REFERENCES

1. Luo, P., LI, X. Application and Market of 1,4-butanediol Production of Reppe Method in China, *American Journal of Chemical Engineering*, **2021**, 9*(2)*.34-38.
2. Weissermel, K., Arpe, H.-J., Lindley, C.R., „*Industrial organic chemistry*", Ediția Third completely rev., Weinheim [etc.], VCH, **1997**,
3. Li, F., Lu, T., Chen, B., Huang, Z., Yuan, G. Pt nanoparticles over TiO2–ZrO2 mixed oxide as multifunctional catalysts for an integrated conversion of furfural to 1,4-butanediol, *Applied Catalysis A: General*, **2014**, 478.252-258.
4. Jeong, H., Hwan Kim, T., Ill Kim, K., Haeng Cho, S. The hydrogenation of maleic anhydride to γ-butyrolactone using mixed metal oxide catalysts in a batch-type reactor, *Fuel Processing Technology*, **2006**, 87*(6)*.497-503.
5. Yim, H., Haselbeck, R., Niu, W., Pujol-Baxley, C., Burgard, A., Boldt, J., Khandurina, J., Trawick, J.D., Osterhout, R.E., Stephen, R., Estadilla, J., Teisan, S., Schreyer, H.B., Andrae, S., Yang, T.H., Lee, S.Y., Burk, M.J., Van Dien, S. Metabolic engineering of

Escherichia coli for direct production of 1,4-butanediol, *Nature Chemical Biology*, **2011**, 7*(7)*.445-452.

6. Messori, M., Vaccari, A. Reaction Pathway in Vapor-Phase Hydrogenation of Maleic-Anhydride and Its Esters to Gamma-Butyrolactone, *Journal of Catalysis*, **1994**, 150*(1)*.177-185.
7. Satam, C.C., Daub, M., Realff, M.J. Techno-economic analysis of 1,4-butanediol production by a single-step bioconversion process, *Biofuels Bioproducts & Biorefining-Biofpr*, **2019**, 13*(5)*.1261-1273.
8. https://prismaneconsulting.com/report-details/global-maleic-anhydride-market-study, accesat la data 17.03.2024.
9. Kanetaka, J., Kiryu, S., Asano, T., Masamune, S. Hydrogenation of Maleic Anhydride and Intermediates by Nickel-Rhenium Catalyst Supported on Kieselguhr, *Bulletin of The Japan Petroleum Institute*, **1970**, 12.89-96.
10. Küksal, A., Klemm, E., Emig, G., „*Single-stage liquid phase hydrogenation of maleic anhydride to γ-butyrolactone, 1,4-butanediol and tetrahydrofurane on Cu/ZnO/Al2O3-catalysts"*, din Studies in Surface Science and Catalysis, A. Corma, et al., Editors, Elsevier, **2000,** pp. 2111-2116.
11. Herrmann, U., Emig, G. Liquid phase hydrogenation of maleic anhydride and intermediates on copper-based and noble metal catalysts, *Industrial & Engineering Chemistry Research*, **1997**, 36*(8)*.2885-2896.
12. Herrmann, U., Emig, G. Liquid phase hydrogenation of maleic anhydride to 1,4-butanediol in a packed bubble column reactor, *Industrial & Engineering Chemistry Research*, **1998**, 37*(3)*.759-769.
13. Herrmann, U., Emig, G. Kinetics and mechanism in the liquid-phase hydrogenation of maleic anhydride and intermediates, *Chemical Engineering & Technology*, **1998**, 21*(3)*.285-295.
14. Gautier, V., Champon, I., Chappaz, A., Pitault, I. Kinetic Modeling for the Gas-Phase Hydrogenation of the LOHC γ-Butyrolactone–1,4-Butanediol on a Copper-Zinc Catalyst, *Reactions*, **2022**, 3*(4)*.499-515.
15. Xu, S., Wang, H. Separation of Tetrahydrofuran–Water Azeotropic Mixture by Batch Extractive Distillation Process, *Chemical Engineering Research and Design*, **2006**, 84*(6)*.478-482.
16. Luyben, W.L. Control of the Heterogeneous Azeotropic n-Butanol/Water Distillation System, *Energy & Fuels*, **2008**, 22*(6)*.4249-4258.
17. Reid, C.R., Prausnitz, J.M., Poling, B.E. The properties of gases and liquids, **1987**.587-588.
18. Schlander, J.H., Gasphasenhydrierung von Maleinsäuredimethylester zu 1,4-Butandiol, g-Butyrolacton und Tetrahydrofuran an Kupfer-Katalysatoren, PhD Thesis, Fakultät für Chemieingenieurwesen der Universität Karlsruhe, **2000.**
19. Bozga, G., Brosteanu, A.V., Banu, I., Dimian, A.C. One-stage ethanol to butadiene process: analysis and design of a multi-tubular fixed bed reactor, *Chemical Engineering Research and Design*, **2024**, 203.608-618.
20. Froment, G.F., De Wilde, J., Bischoff, K.B., „*Chemical reactor analysis and design*", Ediția 3rd, Hoboken, N.J., Wiley, **2011**,
21. Herrmann, U., Gerhard, E. Liquid Phase Hydrogenation of Maleic Anhydride and Intermediates on Copper-Based and Noble Metal Catalysts, *Industrial & Engineering Chemistry Research*, **1997**, 36.2885-2896.
22. Kuksal, A., Klemm, E., Gerhard, E. Reaction kinetics of the liquid-phase hydrogenation of succinic anhydride on CuZnO-catalysts with varying copper-to-zinc ratios in a three-phase slurry reactor, *Applied Catalysis* **2001**.237–251.

23. Smith, A.W., Chernyak, Y., Solvent for Recovery of Maleic Anhydride from a Gas Stream, US8940915B2, 27.01.2015.
24. Luyben, W.L. Control of the Heterogeneous Azeotropic n-Butanol/Water Distillation System, *Energy & Fuels*, **2008**, 22.4249–4258.
25. https://www.dow.com/en-us/pdp.dowtherm-a-heat-transfer-fluid.238000z.html, accesat la data 29.06.2023.
26. https://www.indiamart.com/proddetail/1-4-butanediol-1-4-bdo-22232938955.html, accesat la data 25.06.2023.
27. https://www.tradeindia.com/products/gamma-butyrolactone-gbl-96-48-0-c4h6o2-6126994.html, accesat la data 25.06.2023.
28. https://www.alibaba.com/product-detail/Manufacturer-supply-Tetrahydrofuran-THF-CAS-109_1600557850249.html?spm=a2700.galleryofferlist.normal_offer.d_title.1ddd1bddNwWl3H, accesat la data 25.06.2023.
29. https://www.indiamart.com/proddetail/normal-butanol-99-purity-99-9-25744238533.html?pos=4&kwd=butanol&tags=BA||||7533.29|Price|proxy|||TS&prdnmfrm=1, accesat la data 25.06.2023.
30. https://www.alibaba.com/product-detail/High-quality-maleic-anhydride-MA-maleic_1600413785093.html?spm=a2700.galleryofferlist.normal_offer.d_image.257940cbarC78r, accesat la data 25.06.2023.
31. https://theprint.in/india/indias-green-hydrogen-dream-businesses-are-raring-to-go-clean-but-cost-safety-are-concerns/1357203/, accesat la data 25.06.2023.
32. https://www.alibaba.com/product-detail/Top-manufacturer-of-Propylene-Glycol-Tech_1600550800738.html?spm=a2700.galleryofferlist.normal_offer.d_title.6e1e5b3akZUfEP, accesat la data 25.06.2023.
33. https://lonwinchem.en.made-in-china.com/product/CylQDqVThgkA/China-Good-Quality-with-Low-Price-Dibutyl-Adipate-CAS-105-99-7.html, accesat la data 25.06.2023.
34. https://www.acs.org/greenchemistry/principles/12-principles-of-green-chemistry.html, accesat la data 23.06.2023.

INFLUENCE OF FLUORINE LATERAL SUBSTITUTION ON PHOTOISOMERIZATION PROCESS OF AZOBENZENE BENT-CORE LIQUID CRYSTALS

Iulian BERLADEAN[1,2,*], Irina CÂRLESCU[1], Yahia BOUSSOUALEM[2], Abdelylah DAOUDI[2], Nicolae HURDUC[1]

[1]"Gheorghe Asachi" Technical University of Iasi, "Cristofor Simionescu" Faculty of Chemical Engineering and Environmental Protection, Department of Natural and Synthetic Polymers, 73 Prof. Dimitrie Mangeron Street, 700050 Iasi, Romania

[2] Université du Littoral Cote d'Opale, UR 4476 Unite de Dynamique et Structure des Matériaux Moléculaires, 59140 Dunkerque, France

Abstract

This study concerns the photoisomerization process and thermal back relaxation of fluorine substituted azobenzene bent-core liquid crystals. The studied bent-core compounds are resorcinol derivatives with a symmetric molecule, incorporated photosensitive azo linkages in the fluorine-substituted side arms and alkoxy terminal chains. The effect of polar fluorine substituents on the azobenzene side arms of bent core molecules on the photoisomerization process was investigated using UV-Vis spectroscopy. It has been shown that the trans-cis isomerization process by 400 nm UV irradiation is not affected by fluorine substitution. While the thermal back relaxation process is considerably influenced, therefore the thermal relaxation time increased proportionally with the number of side fluorine substituents. Taking into account that thermal relaxation time is of crucial importance for optical storage devices, lateral substitution with fluorine atoms is an efficient method to obtain bent-core photosensitive materials with long thermal back relaxation time.

Key words: bent-core liquid crystals, azobenzene linkage, photoisomerization, fluorine substitution, optical storage devices.

1. Introduction

Photosensitive bent-core liquid crystals compounds have recently attracted attention, due to the unique properties of the photosensitive azobenzene units in combination with liquid crystal properties, such as optical anisotropy and supramolecular chirality of achiral molecules [1,2]. These photosensitive materials can switch from trans (E) to cis (Z) isomer by irradiation with UV light and reverse by thermal back relaxation [3,4]. Numerous applications, including optical storage devices [5], photo-induced phase transitions [6], and optical switching [7], are made possible by these features. In addition, liquid crystalline ferroelectrics and photoswitchable properties of azobenzenes units can be combined to create potentially novel multifunctional materials whose polar response is photo-modulated [8]. Towards the unwrapping domain of photoisomerizable azobenzene liquid crystals, establishing the structure-property relationship is of major importance. A number of studies have already been

*Corresponding author: email address: iulian.berladean@student.tuiasi.ro

reported on this, which describe the relation between electron-donating (-CH_3) or electron-withdrawing (halogen) substitution at the central core or/and at the azobenzene mesogen side units and the photoisomerization properties [3, 5, 8]. The current study is carried out on azobenzene bent-core compounds with lateral fluorine substituents on mesogens, side arms, in order to highlight the effect of substitution on photoisomerization and thermal back relaxation process.

2. Experimental

A Varian Cary 3500 UV-Vis spectrophotometer connected with a small Peltier apparatus was used to perform UV spectroscopy investigations in chloroform solutions at 10^{-5} mol/L using 10 mm path length quartz cuvettes with Teflon stoppers. For the irradiation, two commercial LEDs from Thorlabs, the "M455L2-C4" model with a wavelength of 455 nm and a commercial "Varta" lamp with a maximum wavelength of 400 nm were used.

3. Results and discussions

The synthesis and mesomorphic characterization of bent-core compounds used in this study were reported earlier [9]. Their structure includes the photo-sensitive azo bond (Figure 1a); suitable for photoisomerization process, where the azo group can rotate reversibly and can adopt one of the two conformations (Figure 1b) - the energetically favorable E (trans) conformation or excited Z (cis) isomer.

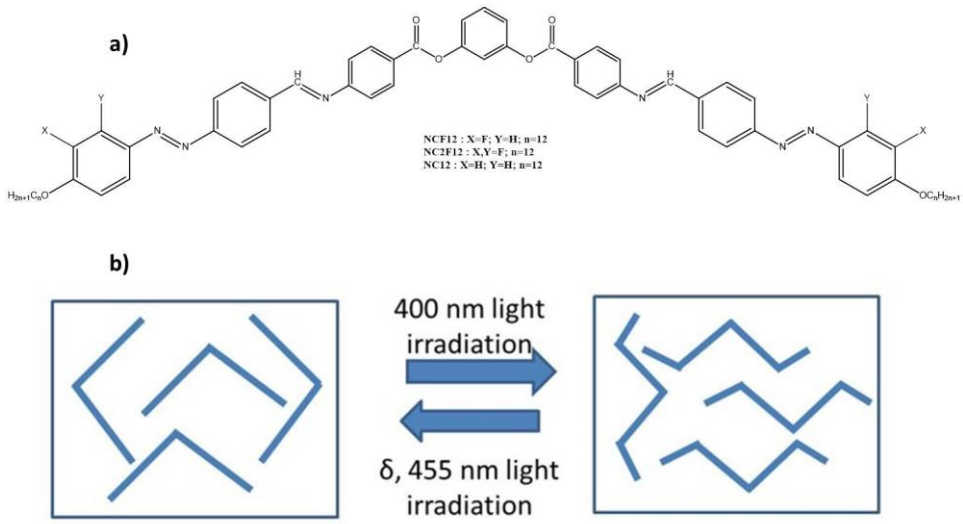

Fig. 1. Molecular structure and schematic representation of studied bent-core compounds: **a)** molecular structure of bent-core azobenzene compounds with fluorine substituted lateral arms; **b)** schematic representation of trans and cis isomers.

This process was observed by UV-vis spectroscopy. In the UV range (376-378 nm), the trans isomer is associated with a significant absorbance band that corresponds to the π-π* transition, while cis isomer associated with weak absorbance band in visible region (450-500 nm) corresponds to n-π* transition (Figure 2).

It was found that all the studied compounds have similar behavior, considering that 20 seconds after being exposed to 400 nm wavelength UV light, they switch to the cis configuration (Figure 2-a,b). The reverse process can be performed by irradiation with visible light (Figure 2-c, d), which requires 20 seconds for 80-90% of total conversion. The total conversion from cis to trans isomer can be achieved by thermal back relaxation in dark conditions. The time required for this process to occur is strictly correlated with the number of polar substituents in the azobenzene units, as demonstrated here by the experimental results (Figure 3).

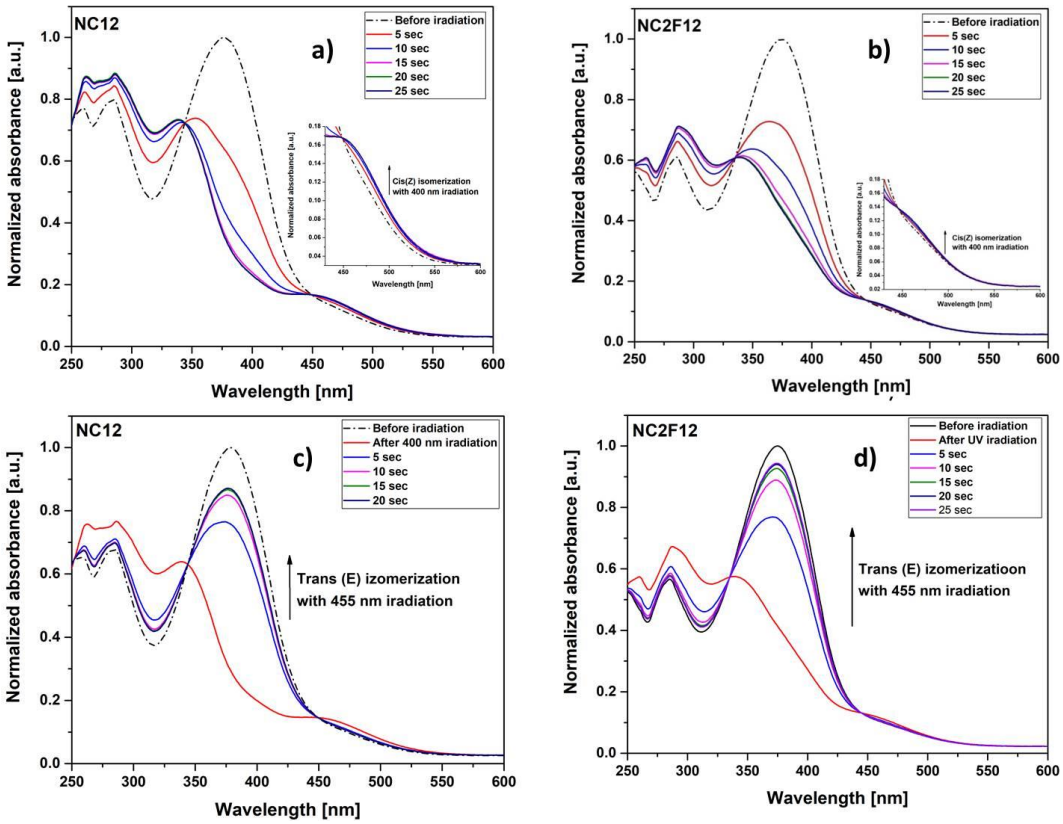

Fig. 2. Absorbance UV-vis bands of studied compounds **a)** trans-cis isomerization by irradiation with UV, 400 nm wavelength lamp of unsubstituted compound **NC12**; **b)** trans-cis isomerization by irradiation with UV, 400 nm wavelength lamp of compound **NC2F12**, containing 4 F atoms; **c)** cis-trans isomerization by irradiation with visible 455 nm blue light of **NC12**; **d)** cis-trans isomerization by irradiation with visible 455 nm blue light of **NC2F12**.

In fact, at 45°C the thermal back relaxation times are the following: 65 minutes for unsubstituted compound (**NC12**), 130 minutes for compound with two fluorine substitutes (NCF12), and 220 minutes for the compound with four fluorine substituents (NC2F12) (Figure 3).
Additionally, it was demonstrated that the photoisomerization of the studied compounds remained stable and reversible, following at least 30 cycles of repeated irradiation (Figure 3d).

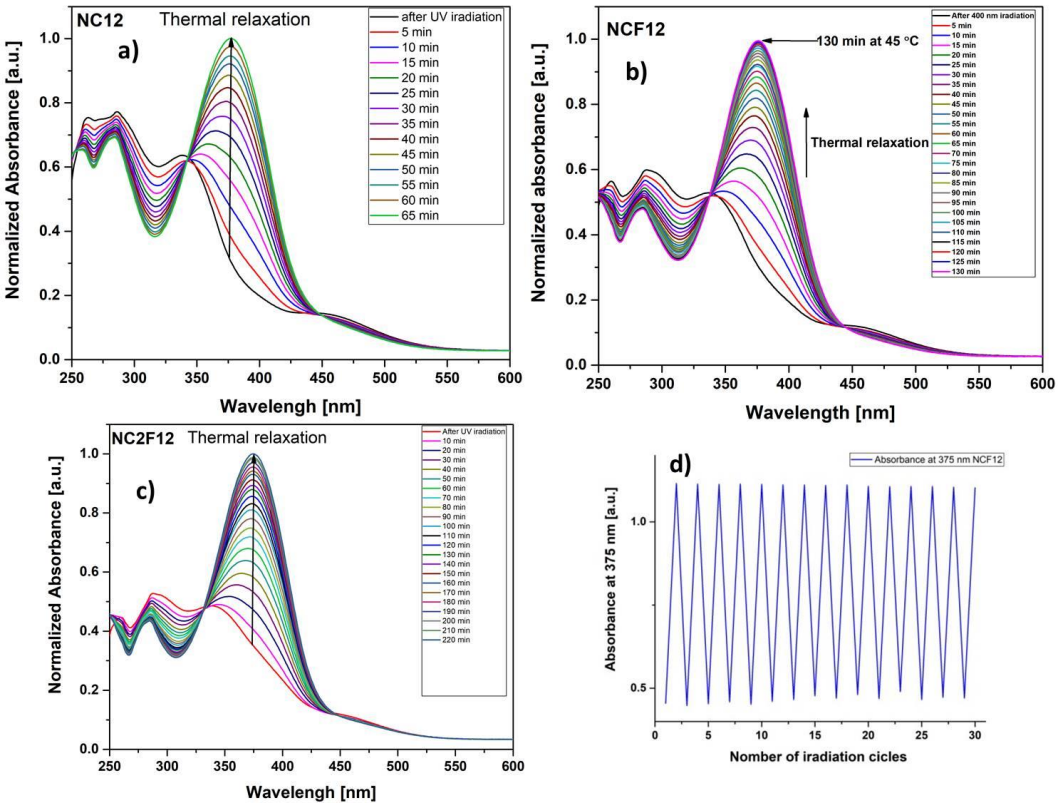

Fig. 3. Absobance UV-vis bands of studied compounds of thermal relaxation at 45 °C after irradiation with UV light for: **a)** unsubstituted **NC12** compound; **b)** substituted with 2 F atoms, **NCF12**; **c)** substituted with 4 F atoms **NC2F12**; **d)** graph of repeated trans-cis isomerization process by irradiation with UV-visible light for 30 cycles for compound **NCF12**.

4. Conclusions

The reported bent-core azobenzene compounds are photoisomerizable and the process can be done in 20 seconds by irradiation with UV or visible light. The conversion time for this process is not significantly affected by polar substituents. On the other hand, the thermal back relaxation process is strongly influenced by the lateral substitution with fluorine atoms and lasts from 65 to 220 min,

depending on the number of substituents. Besides the fact that photoisomerization is a simple way to change the conformation of bent core azobenzene compounds, this is stable under repeated irradiation. In addition, the efficient extension period of the thermal relaxation process for bent-core azobenzene compounds with lateral fluorine substituents has been demonstrated.

REFERENCES

[1] Srinivasan, M. V., Kannan, P. & Roy, A. Photo and electrically switchable B-7 mesophase exhibiting asymmetric bent-core liquid crystals. *New J. Chem*. 37, (2013), 1584-1590.

[2] Cigl, M. et al. Photosensitive chiral self-assembling materials: significant effects of small lateral substituents. *J. Mater. Chem. C,* 4, (2016), 5326-5333.

[3] Ting, T. X., Sarjadi, M. S. & Rahman, M. L. Influences of Central Units and Terminal Chains on the Banana-Shaped Liquid Crystals. *Crystals* 10, (2020), 857.

[4] Vijaysrinivasan, M., Kannan, P. & Roy, A. Dual switchable six-ring bent-core liquid crystals with azo linkages exhibiting B-1 and B-2 mesophases. *Liq. Cryst*. 39, (2012), 1465–1475.

[5] Sunil, B. N. et al. Effective tuning of optical storage devices using photosensitive bent-core liquid crystals. *J. Mol. Liq*. 304, (2020), 112719.

[6] Prasad, S. K., Nair, G. G. & Rao, D. S. S. Photoinduced phase transitions. *Liq. Cryst*. 36, (2009), 705–716.

[7] Saravanan, C., Senthil, S. & Kannan, P. Click chemistry-assisted triazole-substituted azobenzene and fulgimide units in the pendant-based copoly(decyloxymethacrylate)s for dual-mode optical switches. *J. Polym. Sci. Part Polym. Chem.* 46, (2008), 7843–7860.

[8] Alaasar M. Azobenzene-containing bent-core liquid crystals: an overview. *Liq Cryst*. 43, (2016), 2208.

[9] Berladean, I. et al. Novel antiferroelectric materials with resorcinol-based symmetrical fluorinated bent-core mesogens. *J. Mol. Liq.* 388, (2023), 122753.

METHODS FOR ANTIBIOTICS REMOVAL: A COMPREHENSIVE ANALYSIS

Diana HANGANU[1], Lidia FAVIER[2], Maria HARJA[1*]

[1]"Gheorghe Asachi" Technical University of Iasi-Romania, Faculty of Chemical Engineering and Environmental Protection, 73 Prof. D. Mangeron Blvd., 700050, Iasi, Romania

[2] Univ. Rennes, Ecole Nationale Supérieure de Chimie de Rennes, CNRS, UMR 6226, 35708 Rennes Cedex 7, France

Abstract

Antibiotics are essential pharmaceuticals utilized globally for the treatment of bacterial infections. However, their widespread use has led to the presence of antibiotic residues in water bodies, posing environmental and health concerns. This article provides an overview of various classes of antibiotics and their impact on water quality. Furthermore, it explores the effectiveness of three primary removal methods: adsorption, advanced oxidation, and electrochemical processes. Advantages and disadvantages of each method are discussed, considering factors such as efficiency, cost-effectiveness, and environmental impact. Understanding the complexities and trade-offs associated with these removal techniques is crucial for the development of sustainable water treatment strategies aimed at mitigating antibiotic contamination in aquatic ecosystems.

Key words: antibiotics, comparison, removal methods

1. Introduction

Each year, the pharmaceutical industry shows extensive growth, largely attributable to scientific development, increased life expectancy, and the prevalence of medical conditions among patients.

The study of antibiotics is expanding to examine their concentrations in nature and how they affect the ecosystem. They prevent the growth of pathogenic bacteria cultures or their destruction after the invasion of the human or animal body [1]. Antimicrobials can treat infections in patients when they reach the minimum inhibitory concentration. Nevertheless, when antibiotic concentrations fall below the minimum inhibitory level, bacteria develop resistance to the antibiotic, leading to an increasingly common issue. Consequently, infections become more complex to treat. The toxic effects of antibiotics in water include treatment failure, prolonging the duration of illnesses, and increasing mortality rates, which are causing high human and economic costs to society [2]. Hospital effluents, wastewater effluents, and soils treated with manure or soils used for livestock typically have the highest quantities.

* Corresponding author: Email address: maria.harja@academic.tuiasi.ro

As can be seen in Figure 1, pharmaceutical substances reach the environment through human consumption either directly through direct elimination or after metabolism, through urine and excretions [3]. Following contamination of water bodies, these pharmaceuticals eventually permeate the soil and plants, impacting not only aquatic organisms such as fish and algae but also terrestrial life. This contamination contributes to heightened bacterial resistance to antibiotics and triggers adverse reactions in humans [4].

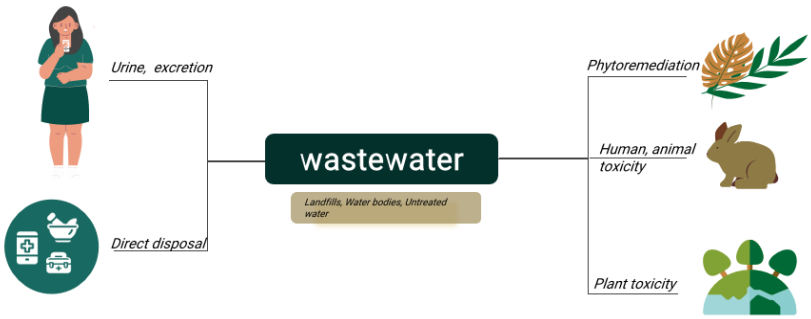

Fig. 1 Antibiotics disposal to wastewater.

The classification of antibiotics can be done according to the chemical structure, the mechanism of action, the bacterial spectrum of action, but also according to the generations in which they were discovered. According to the chemical structure can be seen in fig 2, they are divided into beta lactams, macrolides, tetracyclines, quinolones, aminoglycosides [5]. These are the antibiotics that are currently the most commonly used. The presence of ciprofloxacin at a concentration of 31 mg/L near a pharmaceutical manufacturing site was discovered [6].

Antibiotics: classification based on their molecular structures	
Beta lactams	Penicillins, Cephalosporines, Carbapenems, Monolactams
Macrolides	Erithromycin, Azithromycin, Clarithromycin
Tetracycline	First generation: tetracycline, chlortetracycline, oxytetracycline Second generation:doxycycline, methacycline, rolitetracycline
Quinolones	Norfloxacin, Ciprofloxacin, Ofloxacin,
Aminoglycosides	Gentamycin, Neomycin, Tobramycin
Sulphonamides	Sulfamethoxazole, Sulfanilamide, Sulfacetamide

Fig. 2 Antibiotics classification.

The antibiotic effect of pharmaceutical substances encompasses various mechanisms aimed at inhibiting bacterial growth or even eradicating bacteria.
These mechanisms include:

- Inhibition of protein synthesis or cell wall synthesis;
- Degradation of cell membrane structure;
- Interference with the structure and function of nucleic acids;
- Interference with essential metabolic pathways [5].

Examples of antibiotics for each mode of action can be observed in Figure 3.

Antibiotics: mechanisms of action		
	Inhibition of cell wall synthesis	Cycloserine, penicillins, cephalosporines, monobactams
	Inhibition of the structure and function of nucleic acids	Quinolones (Nalidix acid, ciprofloxacin)
	Protein synthesis (505, 305 inhibitors	Erythromycin, chloramphenicol, lincomycintetracyclines, streptomycin
	Blockage of key metabolic pathways: Folic acid metabolism	Trimethroprim, sulfonamides
	Cytoplasmic membrane structure	Polymyxins, daptomycin

Fig. 3 Antibiotics: mechanism of actions.

2. The methods for antibiotics removal from wastewater

Currently, numerous experimental methods exist for removing antibiotics from wastewater, including chemical methods like ion exchange, physical methods lid adsorption and precipitation, advanced oxidation like fenton oxidation or electrochemical oxidation and biological treatment (Fig 4.)
Afterward, non-biological experimental methods will be described for removing antibiotics from the water, mostly researched drugs being beta lactam and glycopeptide [1]. Each method has its advantages and limitations [7, 8].

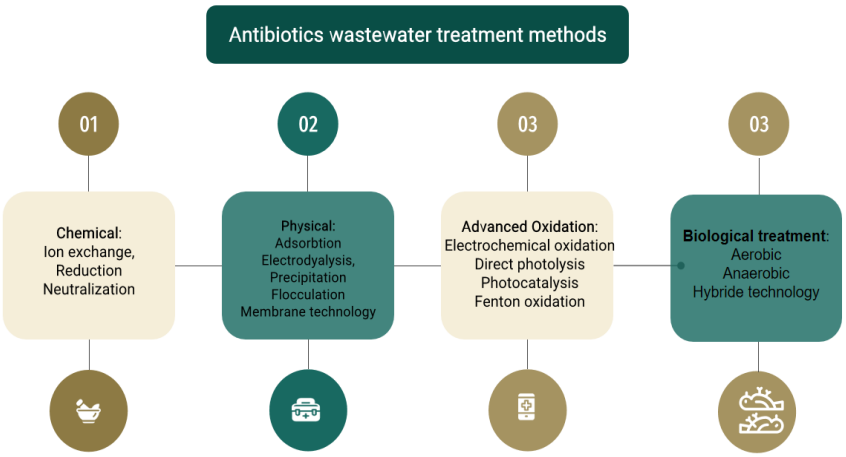

Fig. 4 Wastewater treatment methods for antibiotics removal

2.1.Adsorption method

Renowned for its widespread adoption, affordability, and environmentally friendly nature, the adsorption method stands out as a highly efficient approach, characterized by its rapid regeneration rates for adsorbents. The adsorbents commonly used for antibiotic removal include activated charcoals, bentonite, biochars, carbon nanotubes and ion-exchange resins [9].

Throughout the process of adsorbing pharmaceutical substances, the interactions between the adsorbent and the active compound encompass a variety of bonding mechanisms, such as physical bonds, weak chemical bonds, electrostatic interactions or donor-acceptor interactions.

As can be seen in fig 5, chemical interactions include acid-base interaction (H^+, OH^-), coordinative bonding (shared pair of electrons, forms when both electrons originate from the same atom) or chemical bonding between different functional groups (ionic bonding), while physical interactions adsorbent- drugs are weaker intermolecular forces such as hydrogen bonding and van der Waals forces. The physical interactions are reversible and non-specific [5].

The adsorption process includes several steps [10]:

- Adsorbate molecules are transported through the external layer of the adsorbent;
- The particle diffuses along the film;
- The molecules adsorption through the porous structure to the active sites;
- Interactions between the particle and the active sites of the adsorbent.

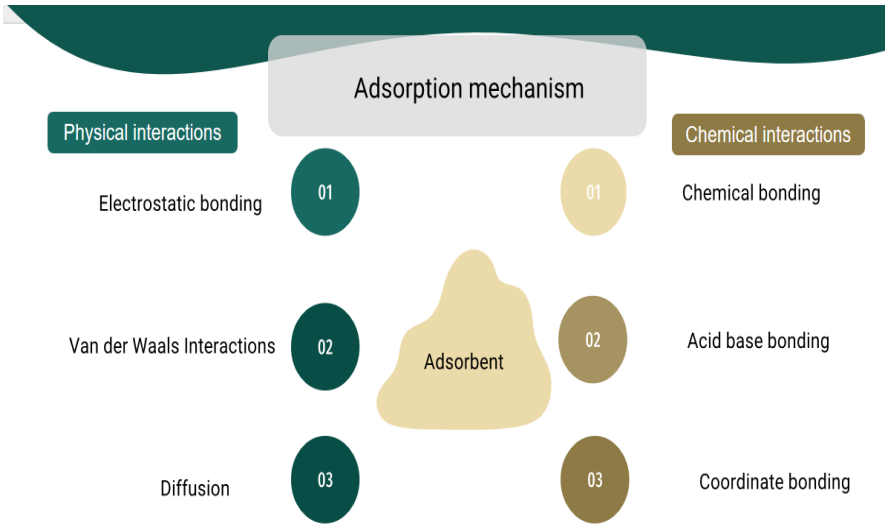

Fig. 5 Adsorption mechanisms.

The number of aromatic rings present in antibiotics was identified as the primary factor influencing the rate of adsorption. The main mechanism of adsorption is attributed to the interactions of the π-π bond [5]. Another significant parameter is pH because when the solution pH is below the pharmaceutical's pKa value, the drug molecules remain ionized and negatively charged, facilitating their adsorption onto negatively charged adsorbents through electrostatic linkage. This phenomenon is crucial for effective removal of pharmaceuticals from water using adsorption processes [11].

The adsorption of amoxicillin was made on activated carbon and bentonite by Putra et al. [12] using a concentration of 300 mg/L of antibiotic, while Méndez-Díaz et al. [13] achieved 90% removal of dimetridazole, metronidazole, tinidazole using activated carbon.

2.2.Advanced oxidation process (AOP)

AOPs are classified into two categories: non-photochemical AOPs (such as ozonation, Fenton, and electrolysis) and photochemical AOPs (such as photolysis, photocatalysis, and photo-Fenton).

The use of photocatalysis can result in several advantages, such as cost reduction, increased efficiency, and enhanced degradation of active substances [14]. In the process of advanced oxidation, a group of activated species, specifically hydroxyl radicals, break down pharmaceutical substances into less toxic intermediates or completely oxidize them to CO_2 and H_2O.

(1) Pharmaceutical ingredient + h$\nu \rightarrow e^- + h^+$

(2) $H_2O \rightarrow OH^- + H^+$

(3) O_2 *(adsorbed)* + $e^- \rightarrow O_2^{*-}$

(4) $O_2^{*-} + e^- \rightarrow HOO^*$

(5) $2HOO^* + O_2 \rightarrow H_2O_2$

(6) $H_2O_2 \rightarrow 2OH^*$

(7) $h^+ + OH^- \rightarrow OH^*$

(8) $h^+ + H_2O \rightarrow OH^* + H^+$

(9) OH^* + RH → Less toxic compound

(10) Intermediate compound → $\boldsymbol{H_2O} + \boldsymbol{H_2}$

An important aspect regarding the advanced oxidation of organic compounds is represented by the presence of other ions in the solution, which interfere with the reactive species formed in water through hydrophobic, electrostatic or even size exclusion interactions. Following the photolysis process, the stability of the pharmacotoxicity of the obtained intermediate or even final compounds is also necessary, so that the final solution has a lower toxicity than the initial one. The use of enzymes extracted from organisms or fungi is utilized to demonstrate the safety of the disposal method [15].
A specific example of advanced oxidation is Fenton oxidation, which utilizes iron ions and hydrogen peroxide in the initial solution to generate reactive hydroxyl ions. These hydroxyl ions are highly reactive and capable of breaking down antibiotic molecules. Fenton oxidation has practical experimental advantages and high effectiveness due to the non-toxic nature of iron ions and the low purchase cost of oxygenated water.

2.3.Electrochemical oxidation

The electrochemical oxidation process involves the degradation of the medicinal active substance, typically occurring on the surface of an anode composed of materials such as graphite, TiO_2, Ti-based alloys, Ru or Ir oxides, or boron-doped diamond. This degradation can occur through direct oxidation, where electrons are transferred directly from the contaminant to the electrode, resulting in the formation of cationic radicals [5]. Alternatively, the degradation can occur indirectly, where the molecule is degraded in solution by electrons transferred between electrodes in the presence of electroactive species. These electroactive species may include metallic redox couples such as Ag(II), Fe(III), Ce(IV), Mn(III), or strong oxidants such as H_2O_2, O_3, persulfates, percarbonate, perphosphate, and chlorinated species [10]. Various anode materials are utilized in electrochemical degradation, including platinum, TiO_2, graphite, activated carbon, and combinations like Sn/Sb/Ni. These

materials offer advantages such as low voltage operation, short reaction times, complete mineralization of contaminants, and sometimes require no pH adjustments [16].

Key aspects of the electrochemical degradation process/experiment encompass several factors [9]. These include:

- Selection of Anode Materials: Anodes like platinum, TiO_2, graphite, and activated carbon, as well as composite materials such as Sn/Sb/Ni, are commonly used;
- Generation of Indirect Oxidants: Indirect oxidants, such as chloride or hypochlorite ions, play a significant role in the degradation process;
- Distance Between Anode and Cathode;
- Choice of Electrolyte: Electrolytes, such as NaCl, Na_2SO_4, and KCl, are employed to enhance conductivity in the electrolyte solution.

3. Comparison of methods and its performances

In recent years, there has been significant progress in the removal of medicinal substances from water, driven by experimental advancements. This development is particularly crucial due to the rising concentrations of antibiotics in water sources. Table 1 outlines the advantages and disadvantages of the methods utilized for this purpose.

Table 1

Comparison between antibiotics removal methods

Removal method	Method's advantages	Method's disadvantages
Adsorption	Simple equipment, high effective process, highly used for different molecules	Non-selective method, influenced by pH, hight cost of regeneration
Photocatalysis	Non-toxicity, low cost, fully destroy the organic compound, good stability of photocatalyst	Poor efficiency for high concentrations, toxic intermediate compounds, fast electron hole recombination
Fenton	Rapid degradation, in-situ production of reactive radicals, without sludge	Ferrous sludge produced, formation of unknown intermediate molecules, technical constrains
Electrochemical oxidation	Unselective or selective function of the electrochemical cell; zero sludge	Expensive

Biological treatment	High performance, lower biomass yield	High energy consumption and operating cost; not digest all type of antibiotics

Additionally, understanding the correlation between the chemical structure of antibiotics and the physico-chemical removal methods employed is essential for effective characterization.

The aromatic compounds were found to adsorb onto graphene and graphene oxide through π-π stacking, as reported in earlier literature. Tetracycline (TC) consists of four aromatic rings, each with various functional groups such as amino, ketone, alcohol, and phenol. Based on Phoon et al. [5] review, adsorption appears to be a more effective removal method for tetracycline compared to sulfamethoxazole. Tetracycline exhibited strong adsorption behavior, indicating that it binds well to soil surfaces, making it more likely to be effectively removed through adsorption processes. On the other hand, sulfamethoxazole showed low adsorption behaviour, implying that it does not bind as strongly to soil surfaces. Therefore, while adsorption may still contribute to the removal of sulfamethoxazole, it may not be as effective as it is for tetracycline.

The predominant technique employed for eliminating antibiotics belonging to the macrolide class involves adsorption, utilizing a variety of materials such as goethite biochar, commercial resins, mesoporous silica SBA-15, activated carbon derived from filiculoides, graphene derived from banana peel, zeolite/cellulose acetate fiber, as well as biochar derived from organic waste feedstocks [17].

Titanium dioxide has demonstrated efficacy in the photodegradation of quinolone antibiotics present in water sources [18]. Oxidation stands out as the predominant method utilized for removing antibiotics from the quinolone class. Notably, visible light removal studies have been conducted, with removal efficiencies of 50% for levofloxacin (using visible light with Ag/TiO_2), 83% with TiO_2 alone, 87.79% for norfloxacin (with $TiO_2/Bi_2WO_6/rGO$) [19], and 89% for ciprofloxacin (using visible light with TiO_2: Au-NSs) [20].

In the matter of fluoroquinolones, studies have shown that electrochemical oxidation of the piperazinyl ring has significant limitations, as the toxicity of the final solution remains unchanged or may even increase [10].

4. Conclusions

As evident, there exist numerous methods for removing antibiotics from water, each with its own set of advantages and disadvantages. The selection of a particular method depends on factors such as the chemical structure of the pharmaceutical substance and the composition of the solution. Recent research demonstrates the utilization of combined approaches for drug removal from water, aiming to

establish correlations between chemical structure, activity, and physical-chemical separation methods.

REFERENCES

[1] Zhuang M., Achmon Y., Cao Y., Liang X., Chen L., Wang H., Siame B. A., Leung K. Y. Distribution of antibiotic resistance genes in the environment. *Environ. Poll.*, 285, (2021), 117402.

[2] Bueno I., Williams-Nguyen J., Hwang H., Sargeant J. M., Nault A. J., Singer R. S., Impact of point sources on antibiotic resistance genes in the natural environment: a systematic review of the evidence. *Animal Health Res. Rev.*, 18(2), (2017), 112-127.

[3] Mlunguza N., Ncube S., Mahlambi P., Chimuka L., Madikizela L., Adsorbents and removal strategies of non-steroidal anti-inflammatory drugs from contaminated water bodies. *J. Env. Chem. Eng.*, 7, (2019), 103142.

[4] Szymańska U., Wiergowski M., Sołtyszewski I., Kuzemko J., Wiergowska G., Woźniak M. K. Presence of antibiotics in the aquatic environment in Europe and their analytical monitoring: Recent trends and perspectives. *Microchem. J.*, 147, (2019), 729-740.

[5] Phoon B. L., Ong C. C., Saheed M. S. M., Show P. L., Chang J. S., Ling T. C., Lam S. S., Juan J. C. Conventional and emerging technologies for removal of antibiotics from wastewater. *J. Hazard. Mater.*, 400, (2020), 122961.

[6] Etebu E., Arikekpar I., Antibiotics: Classification and mechanisms of action with emphasis on molecular perspectives. *Int. J. Appl. Microbiol. Biotechnol. Resch.*, 4 (2016), 90-101

[7] Derakhshan Z., et al., Removal Methods of Antibiotic Compounds from Aqueous Environments – A Review. *J. Environ. Health Sust. Develop.*, 1(1), (2016), 51-74.

[8] Favier L., Simion A. I., Hlihor R. M., Fekete-Kertész I., Molnár M., Harja M., Vial, C. Intensification of the photodegradation efficiency of an emergent water pollutant through process conditions optimization by means of response surface methodology. *J. Env. Manag.*, 328, (2023), 116928.

[9] Lu Z.-Y., Ma Y.-L., Zhang J.-T., Fan N.-S., Huang B.-C., Jin R.-C. A critical review of antibiotic removal strategies: Performance and mechanisms. *J. Water Proc.*, (2020), 38(3):101681.

[10] Homem V., Santos, L. Degradation and removal methods of antibiotics from aqueous matrices - A review. *J. Environ. Manag.*, 92, (2011), 2304-2347.

[11] Natarajan R., et al. Understanding the factors affecting adsorption of pharmaceuticals on different adsorbents - A critical literature update. *Chemosphere*, 287(Pt 1), (2022), 131958

[12] Putra E.K., Pranowo R., Sunarso J., Indraswati N., Ismadji S., Performance of activated carbon and bentonite for adsorption of amoxicillin from wastewater: mechanism, isotherms and kinetics. *Water Res*. 43, (2009), 2419e2430.

[13] Méndez-Díaz J.D., Prados-Joya G., Rivera-Utrilla J., Leyva-Ramos R., SánchezPolo M., Ferro-García M.A., Medellín-Castillo N.A., Kinetic study of the adsorption of nitroimidazole antibiotics on activated carbons in aqueous phase. *J. Colloid Interf. Sci.* 345, (2010), 481-490.

[14] Apostolescu N., Tataru Farmus R. E., Harja M., Vizitiu M. A., Cernatescu C., Cobzaru C., Apostolescu G. A., Photocatalytic removal of antibiotics from wastewater using the CeO2/ZnO heterojunction. *Materials*, 16(2), (2023), 850.
[15] Saravanan P., Senthil Kumar S., Jeevanantham M., Anubha S., Jayashree S., Degradation of toxic agrochemicals and pharmaceutical pollutants: Effective and alternative approaches toward photocatalysis. *Environ. Pollut.*, 298, (2022), 118844.
[16] Kurt A., et al. Electrochemical Removal of Cefazolin from Aqueous Media by Novel Composite Anodes: Effects of Electrolytes and Operating Parameters. *Int. J. Electrochem. Sci., 16(11)* (2021).
[17] Shearer L., Pap S., Gibb S. W. Removal of pharmaceuticals from wastewater: A review of adsorptive approaches, modelling, and mechanisms for metformin and macrolides. *J. Environ. Chem. Eng.*, 10(4), (2022), 108106.
[18] Sowik P., Kowalska K., Felis E. Solar-Driven Degradation of Ciprofloxacin in the Aquatic Environment. *Journal of Ecological Engineering*, 25(3) (2024).
[19] Zhao Y., Kong L., Li S., Zhao Z., Wang N., Pang, Y., Research progress on composite material of bismuth vanadate catalyzing the decomposition of Quinolone antibiotics. *Sci. Reports*, 14(1), (2024), 1591.
[20] Luo M. Q., Liu H. J., Yang L. X., Wang W. J., Zeng C. L., Precisely dominating oxygen vacancy of Magnéli phase titanium suboxides to efficiently remove quinolone antibiotics under visible light. Sep. Purif. Technol., 341, (2024), 126626.

CURRENT RESEARCH FOR ORGANIC COMPOUNDS REMOVAL USING $BiFeO_3$

Laura NISTOR, RAMONA-Elena Tataru-Farmus, Maria Harja*

”Gheorghe Asachi” Technical University of Iasi-Romania, Faculty of Chemical Engineering and Environmental Protection, Bd D. Mangeron 73, 700050 Iasi, Romania

Abstract

An overview of the synthesis, characteristics and potential applications of $BiFeO_3$ perovskite materials is provided in this communication. The enhanced photocatalytic activity of $BiFeO_3$ compound synthesized via sol-gel method for phenol degradation in direct sunlight is preferred versus the co-precipitation or hydrothermal methods. Its advantageous characteristics, such as a reduced energy band gap and effective charge carrier separation are responsible for $BiFeO_3$'s improved performance. The $BiFeO_3$ sample also shows good stability and recyclability, which makes it a viable option for environmental applications. These results advance our knowledge of $BiFeO_3$-based photocatalysts and their mechanisms of pollutant degradation.

Key words: Photocatalysis, $BiFeO_3$, pollutant degradation, perovskites, synthesis methods

1. Introduction

The work identifies topics for further investigation and offers insights into the optimization of $BiFeO_3$ - based photocatalysts for removal of organic compounds from industrial waters [1]. In order to better understand how to improve the photocatalytic characteristics and synthesis techniques of $BiFeO_3$ perovskite-type materials, a comparative investigation of their efficacy in eliminating organic contaminants from wastewater is conducted. $BiFeO_3$ perovskites' special qualities and potential for environmental remediation have drawn attention to them as prospective photocatalysts.

The effects of several synthesis procedures, including sol-gel, hydrothermal, and co-precipitation approaches, on the properties of the materials and photocatalytic activity are contrasted. The efficiency of several techniques in enhancing light absorption, charge separation, and catalytic efficiency is also evaluated, including doping, heterojunction creation, surface modification, and nanostructuring. Effective remediation solutions are necessary due to the enormous dangers that organic contaminants in water sources cause to both human health and the environment [2].

Because of their special characteristics, such as ferroelectricity, magnetism, and photocatalysis, materials of the $BiFeO_3$ perovskite class have become attractive options for the photocatalytic removal of organic contaminants [3].

* Corresponding author: Email address: maria.harja@academic.tuiasi.ro

However, a deep comprehension of synthesis techniques and photocatalytic performance enhancement tactics is necessary for the development of $BiFeO_3$-based photocatalysts for water treatment. The efficiency of many synthesis approaches, including sol-gel, hydrothermal, and co-precipitation processes, in generating $BiFeO_3$ perovskite-type materials with the required structural, morphological, and optical properties is compared. Each synthesis method's benefits, drawbacks, and final material properties are assessed to see if it is suitable for use in photocatalytic applications [4]. Having excellent crystal structure properties, easily adjustable structural morphology and photocatalytic activity in visible light, bismuth ferrite ($BiFeO_3$) is mostly recommended for degradation of organic compounds from wastewaters. Photocatalytic technology has occurred as a recommending approach for environmental remediation [5].

Therefore, in order to examine the impact of BiFeO3 materials on morphological, optical, photoelectrochemical, and photocatalytic capabilities, it is imperative to synthesize them using various ways. In the current study, $BiFeO_3$ materials with a range of morphologies and average particle sizes between nanometers and micrometers were created using three different synthesis processes. Many methods were employed to ascertain the physicochemical, optical, and electrochemical properties of the as-synthesized materials. Using phenol as a model organic pollutant, the photocatalytic activity of the materials as produced were examined. Finally, electrochemical measurements and the detection of reactive species and hydroxyl radicals during the photodegradation process were used to study the recycling capability and potential photocatalytic mechanism over $BiFeO_3$ material [6].

2. Methods

Three processes are used to produce $BiFeO_3$ nanoparticles: sol-gel, hydrothermal, and co-precipitation. The crystal structure and phase purity of the produced materials are ascertained using XRD examination. To investigate the morphological characteristics and particle size distribution, SEM imaging is used. By observing how organic contaminants degrade in the presence of visible light, the photocatalytic activity of the $BiFeO_3$ samples is assessed.

Using a straightforward hydrothermal method, bismuth ferrite ($BiFeO_3$) photocatalysts were created. The size and shape of the catalysts were customized by varying the concentration of KOH in the precursor solution. The reported phase evolution, particle size, and morphologies in relation to various KOH Mineralizer concentrations. Additionally, rhodamine B (RhB) was completely degraded under the influence of visible light in order to assess the photocatalytic activity and stability test of the generated samples. The ideal conditions for single phase $BiFeO_3$ and enhanced degrading efficiency are 4M KOH concentrations.

Even after five recycling experiments, the material continues to exhibit great stability and photocatalytic activity without losing any of its characteristics [7].

To efficiently reduce the size of BFO from microscale (~25 μm) to nanoscale (~45 nm), a straightforward hydrothermal approach was suggested. The BFO would significantly inhibit the recombination of electrons and holes, perhaps providing a more efficient pathway for photo-generated carriers to move to the surface and engage in photocatalytic activities. The Methyl Orange photodegradation rate of the nanoscale-BFO is 6.161 h^{-1}, which is over 5 times higher than the microscale-BFO's, as predicted. The work offers a viable synthesis method for creating iron oxide semiconductors at the nanoscale that could be used in more effective photocatalytic applications [8].

3. Results and discussions

In this field, $BiFeO_3$ (BFO) is a well-known material. With a tiny bandgap of 2.1 eV, it is a single-phase semiconductor with outstanding chemical stability. Chang et al. conducted a study on the use of BFO for the photocatalytic degradation of phenol, Fig. 1. The researchers generated sheet-like, coral-like, and rod-like structures by hydrothermal, sol–gel, and coprecipitation synthesis techniques, respectively. The sample made with the sol-gel technique showed improved phenol degradation (98.9%) in 120 minutes under direct sunlight. The removal efficiencies of the BFO samples produced by hydrothermal and coprecipitation techniques were 77.4% and 66.9%, respectively [6].

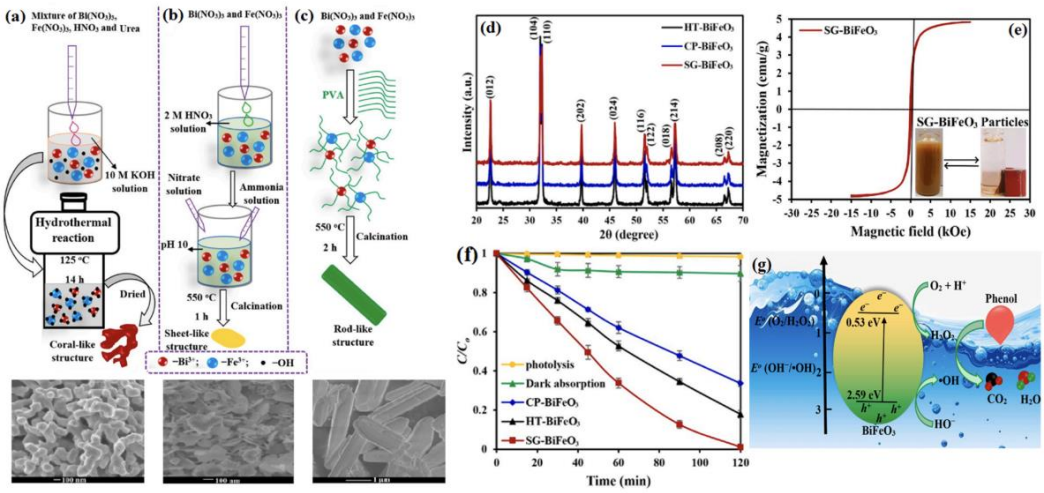

Fig. 1 $BiFeO_3$ (BFO) synthesis via the (a) hydrothermal route, (b) coprecipitation method, (c) sol–gel technique (d) X-ray diffraction patterns of the BFO samples, (e) M–H loop of the sol–gel BFO, (f) photocatalytic degradation of phenol via photolysis, and (g) a proposed schematic diagram for the photodegradation process. Adapted from [6].

Fig.1 (d) The highly crystalline nature of the as-synthesized $BiFeO_3$ materials was shown by the strong and sharp peaks. Furthermore, there was no discernible foreign distinctive peak for impurity in the synthesized samples, suggesting a high degree of product purity [6].

Fig.1 (e) shows the synthesized BiFeO3 sample's M − H loops. The synthesized sample was found to be superparamagnetic, as evidenced by the M − H loops' minimal coercivity and remanence magnetization when no external magnetic field was present [9]. Superparamagnetic materials, in contrast to other magnetic materials, have reversible magnetic interaction, which makes them potentially very beneficial in environmental applications. The BiFeO3 particles were redistributed in the aqueous solution, indicating the possibility of their recycling characteristics, when the externally supplied magnetic field was removed. A distinct specific saturation magnetization of 4.91 emu/g was observed, surpassing the value reported in the $BiFeO_3$ literature [10-12].

Fig. 1 (f) The comparison investigations revealed that a negligible quantity of phenol was removed when the phenol solution was agitated in the dark while the BiFeO3 sample was present, or when the phenol solution was exposed to radiation while the $BiFeO_3$ samples were absent. When exposed to direct sunshine for 120 minutes, the phenol content of the $BiFeO_3$ samples decreased by 66.9% and 77.4%, respectively, when CP-$BiFeO_3$ and HT-$BiFeO_3$ samples were used [13]. In contrast, following a comparable amount of sun exposure, the SG-$BiFeO_3$ particles caused a 98.95% phenol degradation. Because of their well-defined rod-like shape and narrower energy bandgap, $BiFeO_3$ particles may have a greater photodegradation performance [14]. This is because they may have fewer photogenerated charge carrier recombination and more active sites on the photocatalyst surface [6, 15].

Fig. 1 (g) The $BiFeO_3$ sample with a rod-like structure appears to have a stronger photocatalytic degradation because of the formation of h^+, H_2O_2, and •OH radicals, according to the results mentioned above. The surface-adsorbed phenol molecules were then gradually destroyed by these h^+, H_2O_2, and •OH radicals, which transformed them into non-toxic mineralization products [6].

4. Conclusions

In conclusion, the enhanced photocatalytic activity of $BiFeO_3$ in direct sunlight indicates its amazing potential as a photocatalyst for the breakdown of organic contaminants. The synthesis of $BiFeO_3$ in a variety of morphologies by different methods emphasizes how crucial morphology control is to maximize photocatalytic efficiency. The remarkable stability and recyclable nature of $BiFeO_3$ emphasizes even more how well-suited it is for real-world uses. Subsequent studies on photocatalysis involving $BiFeO_3$ ought to concentrate on augmenting its photocatalytic efficacy, comprehending the fundamental

principles, and investigating innovative synthesis approaches to customize its characteristics for distinct environmental remediation predicaments. To fully realize the promise of $BiFeO_3$ photocatalysts in tackling global water pollution challenges, it will also be imperative to scale up production and incorporate them into practical water treatment systems.

REFERENCES

[1] Nassereddine Y., Benyoussef M., Asbani B., El Marssi M., Jouiad M., Recent Advances toward Enhanced Photocatalytic Proprieties of $BiFeO_3$-Based Materials. *Nanomaterials*, *14*(1), (2023), 51.

[2] Chawla H., Chandra A., Ingole P. P., Garg S., Recent advancements in enhancement of photocatalytic activity using bismuth-based metal oxides Bi_2MO_6 (M= W, Mo, Cr) for environmental remediation and clean energy production. *Journal of Industrial and Engineering Chemistry*, *95*, (2021), 1-15.

[3] da Cruz Severo E., Dotto G. L., Silvestri S., dos Santos Nunes I., da Silveira Salla J., Martinez-de la Cruz A., Foletto E. L., Improved catalytic activity of EDTA–modified BiFeO3 powders for remarkable degradation of procion red by heterogeneous photo–Fenton process. *Journal of Environmental Chemical Engineering*, *8*(4), (2020), 103853.

[4] Huang L., Huang X., Yan J., Liu Y., Jiang H., Zhang H., Liu Q., Research progresses on the application of perovskite in adsorption and photocatalytic removal of water pollutants. *Journal of Hazardous Materials*, *442*, (2023), 130024.

[5] Zhou T., Zhai T., Shen H., Wang J., Min R., Ma K., Zhang G., Strategies for enhancing performance of perovskite bismuth ferrite photocatalysts ($BiFeO_3$): A comprehensive review. *Chemosphere*, (2023), 139678.

[6] Chien S. W. C., Ng D. Q., Kumar D., Lam S. M., Jaffari, Z. H., Investigating the effects of various synthesis routes on morphological, optical, photoelectrochemical and photocatalytic properties of single-phase perovskite BiFeO3. *Journal of Physics and Chemistry of Solids*, *160*, (2022), 110342.

[7] Rajitha B., Rao K. V., Suvarna R. P., Synthesis of multiferroic BiFeO3 microcrystals for photocatalytic activity and stability performance. *Materials Today: Proceedings*, *26*, (2020), 126-129.

[8] Li Y., Wang X. T., Zhang X. Q., Li X., Wang J., Wang C. W., New hydrothermal synthesis strategy of nano-sized BiFeO3 for high-efficient photocatalytic applications. *Physica E: Low-dimensional Systems and Nanostructures*, *118*, (2020), 113865.

[9] Raha S., Ahmaruzzaman M., Enhanced performance of a novel superparamagnetic g-C_3N_4/NiO/ZnO/Fe_3O_4 nanohybrid photocatalyst for removal of esomeprazole:

Effects of reaction parameters, co-existing substances and water matrices. *Chemical Engineering Journal*, *395*, (2020), 124969.

[10] Cheng S., X, Q., Ha, X., Wan, Z., M, N., Du P., Formation of nano-Ag/BiFeO3 composite thin film with extraordinary high dielectric and effective ferromagnetic properties. *Journal of Materials Science: Materials in Electronics*, *28*, (2017), 5652-5662.

[11] Haruna A., Abdulkadir I., Idris, S. O., Photocatalytic activity and doping effects of BiFeO3 nanoparticles in model organic dyes. *Heliyon*, 6(1) (2020).

[12] Zhang L., Li X., Chen J., Jin D., Cheng J., Enhanced photocatalytic activity in ferroelectric BiFeO3 nanoparticles treated by a corona poling method. *Ceramics Internationa*l, 48(11), (2022), 15908-15912.

[13] Sharmin F., Basith M. A., Highly efficient photocatalytic degradation of hazardous industrial and pharmaceutical pollutants using gadolinium doped $BiFeO_3$ nanoparticles. *Journal of Alloys and Compounds*, 901, (2022), 163604.

[14] Gupta G., Kansal S. K., Umar A., Akbar S., Visible-light driven excellent photocatalytic degradation of ofloxacin antibiotic using $BiFeO_3$ nanoparticles. *Chemosphere*, 314, (2023), 137611.

[15] Ponraj C., Vinitha G., Daniel J., Visible light photocatalytic activity of Mn-doped BiFeO3 nanoparticles. *International Journal of Green Energy*, 17(1), (2020), 71-83.

ENHANCED CARBON CAPTURE AND BIOFIXATION USING FUNCTIONALIZED DEEP EUTECTIC SOLVENT AND *DESMODESMUS COMMUNIS* MICROALGAE

Eliza-Gabriela MIHĂILĂ (BRETTFELD)[1,2], Tănase DOBRE[2], Daria Gabriela POPA[1,3], Diana CONSTANTINESCU-ARUXANDEI[1], Florin OANCEA[1,3*]

[1] INCDCP-ICECHIM Bucharest, 202 Spl. Independentei, 6th District, Romania

[2] UNST Politehnica Bucharest, Faculty of Chemical Engineering and Biotechnology

[3] USAMV Bucharest, Faculty of Biotechnologies

Abstract

This study investigates the utilization of a functionalized deep eutectic solvent (DES) comprising choline chloride, ethylene glycol, and monoethanolamine for CO_2 capture integrated with biofixation by Desmodesmus communis microalgae. Efficient CO_2 desorption, recovering nearly 90% of captured CO_2, was achieved. We explore the application of the tricomponent solvent for promoting microalgal cultivation, observing heightened growth rates and biomass production in microalgae exposed to DES-desorbed CO_2. This research highlights the potential of DES-driven CO_2 capture for sustainable microalgal biomass cultivation, contributing to CCUS strategies and environmental sustainability through efficient CO_2 capture and conversion into valuable biomasses.

Key words: CO_2 sequestration, CCUS, environmental sustainability, biomass

1. Introduction

Anthropogenic activities, driven by industrialization and urbanization, have led to unprecedented levels of CO_2 accumulation in the Earth's atmosphere. The resultant greenhouse effect amplifies global warming, disrupts climate patterns, and accelerates environmental degradation with far-reaching consequences for ecosystems, biodiversity, and human societies. Recognizing the urgency of this issue, concerted efforts are underway worldwide to curb CO_2 emissions and transition towards a low-carbon economy.

The urgent need to mitigate CO_2 emissions has prompted extensive research into innovative technologies and strategies aimed at carbon capture, utilization, and storage (CCUS) [1,2]. Among these approaches, the integration of deep eutectic solvents (DESs) [3-8] with microalgae-based CO_2 biofixation [9-14] emerges as a promising avenue for addressing both the challenges of CO_2 emissions and the demand for sustainable bioresources. CCUS technologies have emerged as pivotal strategies in mitigating CO_2 emissions from various point sources [15-17]. These technologies aim not only to capture CO_2 emissions but

*Corresponding author: email address:florin.oancea@icechim.ro

also to utilize captured CO_2 in value-added processes and safely store it to prevent its release into the atmosphere. Deep eutectic solvents have garnered significant attention in recent years as efficient and eco-friendly solvents for CO_2 capture due to their low cost, low volatility, and tunable properties.

In parallel, microalgae have emerged as a promising biological platform for CO_2 biofixation. These microorganisms possess the remarkable ability to convert CO_2 into biomass through photosynthesis, offering a sustainable and renewable approach to carbon capture. Microalga high growth rates, ability to thrive in diverse environments, and potential for producing valuable products such as biofuels, food supplements, and pharmaceuticals further enhance their appeal as a CO_2 mitigation strategy [14,18].

We have previously shown that an integrated system of CO_2 capture in DES and desorption into a *Chlorella* sp. culture is a promising technology that leads to higher biomass production [19]. Encouraged by these results, we aimed to test if other microalga species could be used as well. This study explores the integration of DES-based CO_2 capture with the CO_2 biofixation capacity of *Desmodesmus communis*. By harnessing the unique properties of DES and leveraging the inherent capabilities of microalgae, this series of research seeks to advance the development of efficient and sustainable CCUS technologies. Through comprehensive analysis and experimentation, we aim to elucidate the potential of this integrated approach in mitigating CO_2 emissions while simultaneously contributing to the production of valuable biomass and fostering environmental sustainability.

2. Experimental

Materials

The preparation of the deep eutectic solvent (DES) involved the utilization of high-purity reagents [8,19-23]. Choline chloride (ChCl, +98% purity grade) was procured from Alfa Aesar (USA), monoethanolamine (MEA) and ethylene glycol (EG) with a purity of 99.9% were sourced from Merck (Germany). These reagents underwent blending (ChCl:EG:MEA, 1:2:1 molar ratio), the DES (CEM 1:2:1) was confirmed by FT-IR spectroscopy, and was subjected to testing protocols to assess its efficacy as in our previous work [19]. The microalga strain used was *D. communis* NIVA-CHL 7, obtained from the Norwegian Culture Collection of Algae (NORCCA), Norwegian Institute for Water Research (Oslo, Norway).

The growth medium utilized for the cultivation of *D. communis* was Z8. The Z8 medium recipe [24], formulated for a volume of 1 liter, with reactives purchased from Merck (Germany), entails the preparation of four stock solutions. Stock Solution 1 comprises 46.7 g of $NaNO_3$, 6.0 g of $Ca(NO_3)_2{\cdot}4H_2O$, and 2.5 g

of $MgSO_4 \cdot 7H_2O$. Stock Solution 2 consists of 3.1 g of K_2HPO_4 and 2.10 g of Na_2CO_3. Stock Solution 3 is composed of 2.80 g of $FeCl_3 \cdot 6H_2O$ and 3.90 g of EDTA. Stock Solution 4 is a combination of various compounds, each measured in micrograms per 0.1 liter or per liter, including $Na_2WO_4 \cdot 2H_2O$, $(NH_4)_6Mo_7O_{24} \cdot 4H_2O$, KBr, $Cd(NO_3)_2 \cdot 4H_2O$, $Co(NO_3)_2 \cdot 6H_2O$, $CuSO_4 \cdot 5H_2O$, $ZnSO_4 \cdot 7H_2O$, $NiSO_4(NH_4)_2SO_4 \cdot 6H_2O$, H_3BO_3, V_2O_5, KI, $Cr(NO_3)_3 \cdot 9H_2O$ and $KAl(SO_4)_2 \cdot 12H_2O$.

CO_2 absorption-desorption process

The CO_2 capture process using the DES was conducted in a laboratory vapor–liquid equilibrium (VLE) system. This setup included a cylinder containing 99.999% pure CO_2 gas (Siad, Romania), a glass reactor with a ceramic bubbler for precise gas dispersion and a magnetic stirrer for enhancing gas-liquid contact. The absorption process was maintained at 40°C, under atmospheric pressure until saturation with CO_2 was achieved. Gravimetric analysis quantified the captured CO_2, reaching equilibrium when the increase in DES mass was less than 10 mg.

For CO_2 desorption, a controlled procedure was implemented using a stainless-steel container resistant to depressurization. The DES, CEM 1:2:1, was heated to 80°C for optimal CO_2 desorption, with rotational agitation at 200 RPM ensuring efficiency. A full vacuum minimized the pressure, aiding complete desorption. A pump was used to ensure vacuum, and the desorbed gas was passed through a BIOGAS 5000 gas analyzer to determine the CO_2 concentration at the system outlet. The desorbed gases were intermittently bubbled for 14 days to prevent acidification of the growth medium. This critical step precedes subsequent CO_2 biofixation processes within microalgal photobioreactors (Figure 1).

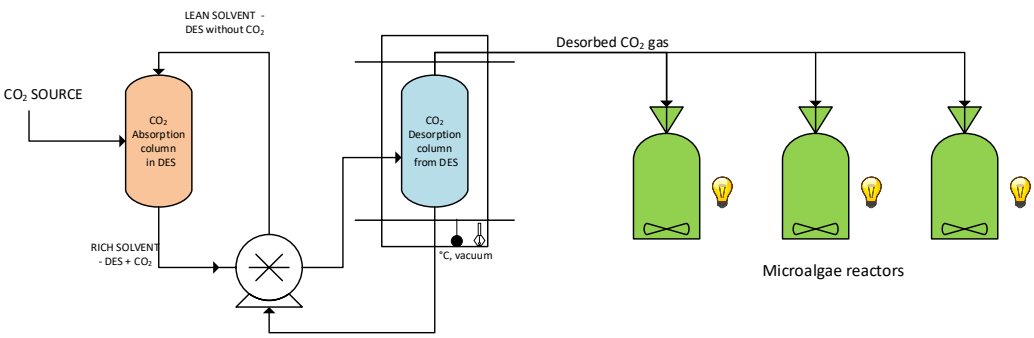

Fig. 1. Integrated CO_2 capture system using deep eutectic solvent (DES) and biofixation of the desorbed CO_2 in microalgae

Microalgal cultivation

In this study, an experimental setup was devised, consisting of six 2 liters (L) Duran GLS80 bioreactors, six magnetic stirrers, a flowmeter, and LED illumination. These were configured to operate at working parameters of 200 RPM, 25°C, and a luminosity of 10 μmol/m^2·s with a day/night photoperiod of 13/11 h. To biofix CO_2 from the DES during desorption, three photobioreactors were employed in series, alongside three air-aerated photobioreactors supplied with atmospheric air at a flow rate of 0.5 L/min.

Microalgal growth [25] was assessed by monitoring optical density and biomass accumulation at intervals of two days. Optical density measurements were conducted using a UV–Vis spectrometer (UV–VIS–NIR DH-2000-BAL, Ocean Optics, The Netherlands), whereas biomass was determined gravimetrically. The experiment was performed in triplicate.

Statistical analysis

SPSS 26 software package (IBM, Armonk, NY, USA) was used for statistical analysis. The data were analyzed in evolution. A least significant difference (LSD) test was used at a significance level of $p < 0.05$.

3. Results and discussions

The mechanism of CO_2 capture by microalgae such as *D. communis* involves a process known as photosynthesis, whereby microalgae absorb CO_2 from the surrounding environment and convert it into organic matter using light energy [24,26,27]. During photosynthesis, microalgae utilize their photosynthetic pigments, such as chlorophyll, to capture solar energy and convert it into chemical energy. This energy is then used to convert CO_2 and water into sugars and oxygen. *D. communis* possesses the ability to regulate its own CO_2 content within cells through complex biochemical processes [10]. For instance, an increase in the concentration of CO_2 in the surrounding environment can lead to an elevation in intracellular carbonate concentration in microalgae, potentially enhancing photosynthetic efficiency. Additionally, microalgae can regulate gene expression for enzymes involved in the CO_2 fixation cycle to adapt to variations in CO_2 levels in the environment.

It is noteworthy that, in addition to photosynthesis, some species of microalgae, including *D. communis*, can also undergo a process called heterotrophic CO_2 assimilation, whereby they absorb CO_2 from the surrounding environment in the absence of sunlight and utilize it to produce organic matter.

The concentration of the desorbed CO_2 was measured at 1.4% using BIOGAS 5000 gas analyzer (UK). Growth monitoring of microalga was conducted through optical density and biomass analysis.

Figure 2 depicts the optical density (OD) of *D. communis* microalga cultures at different time intervals. Optical density is a measure of light absorption by a solution, which can be used to estimate the cell density of microorganisms.

An increase in OD was observed for both microalgal cultures, i.e. control and CO_2-enriched. In the control culture, the OD increased from 0.1110 to 0.3509 over 14 days, representing a total increase of 0.2399. For the CO_2-treated culture, the OD increased from 0.1107 to 0.4120 over 14 days, indicating a total increase of 0.3013. In conclusion, a higher OD was observed for the CO_2-treated culture compared to the control culture. Significant increase of OD induced by the CO_2-treatment compared with control was noticed starting from day 4 of culture.

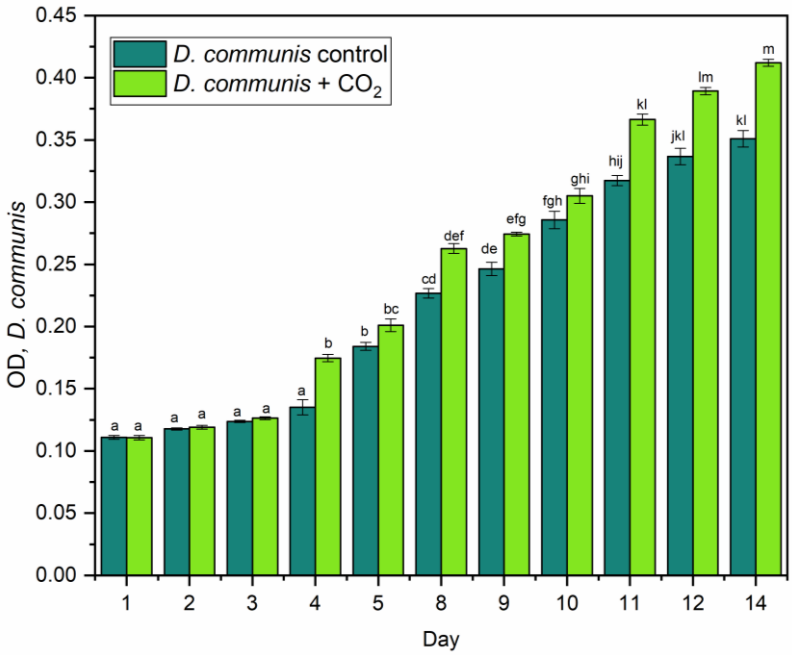

Fig. 2. Optical density (OD) – *D. communis*, measured over 14 days of incubation; the values are mean ± standard error, n = 3. Values with different letters are significantly different at $p < 0.05$.

Figure 3 presents data regarding the gravimetrically-determined biomass formed by the microalga *D. communis* under two different conditions: control and CO_2-treated. The values are expressed in g/L and are measured at various time intervals (every two days), ranging from day 3 to day 14. It is observed that there was an increase in biomass in both culture conditions over time, higher in the case of CO_2 treatment. The data correlate with the OD analysis, with statistically significant differences between the CO_2-treatment and control observed from day 5. Both analysis, OD and biomass, indicate that the desorption of CO_2 from CEM

1:2:1 was efficient in stimulating the growth of *D. communis*. These preliminary results represent a promising starting point that will be further optimized.

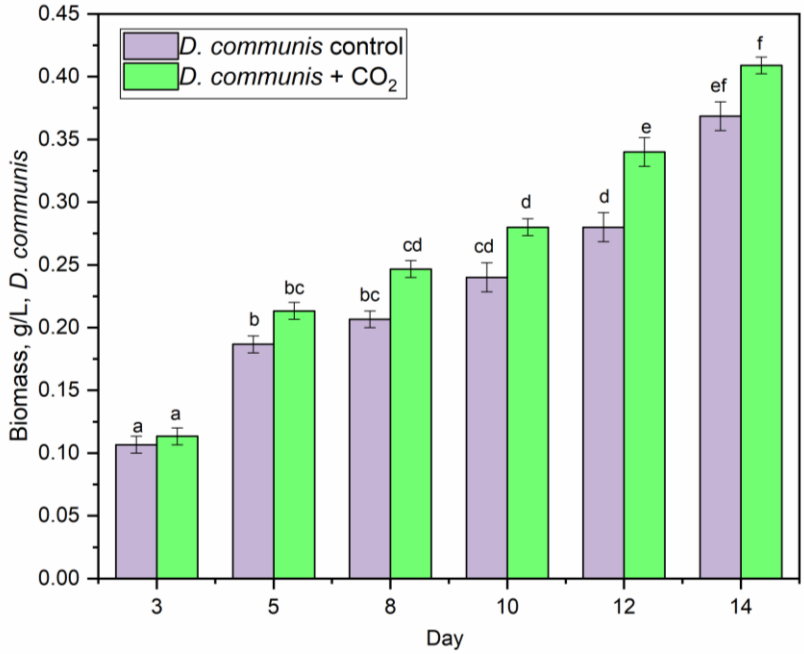

Fig. 3. Biomass – *D. communis*, measured over 14 days of incubation; the values are mean ± standard error, n = 3. Values with different letters are significantly different at $p < 0.05$.

3. Conclusions

In conclusion, an experimental model that could be used for selecting efficient microalgal cultures for CO_2 fixation desorbed from DES was established. In the case of *D. communis*, the optical density and biomass increased in both control and CO_2-treated variants, but the CO_2-treated culture exhibited higher optical density and biomass accumulation than the control culture. The study highlights the positive impact of adding desorbed CO_2 on the growth of *D. communis* microalgae. By using microalgae to convert atmospheric CO_2 or combustion gases captured and desorbed from DES, greenhouse gas emissions can be reduced, contributing to ecosystem preservation. In addition to these benefits, microalgae can be utilized for energy production from renewable sources (such as biogas) and for the production of valuable co-products, such as food supplements or fertilizers.

***Acknowledgements**: The research leading to these results has received funding from the NO Grants 2014-2021, under Project RO-NO-2019-540, contract no. 14 / 2020. We also acknowledge financial support from Ministry of Research, Innovation and Digitization, Core Program, project PN.23.06.02.01 InteGral.*

REFERENCES

1. Chen, S.; Liu, J.; Zhang, Q.; Teng, F.; McLellan, B.C. A critical review on deployment planning and risk analysis of carbon capture, utilization, and storage (CCUS) toward carbon neutrality. *Renewable and Sustainable Energy Reviews* **2022**, *167*, 112537.
2. Jiang, K.; Ashworth, P. The development of Carbon Capture Utilization and Storage (CCUS) research in China: A bibliometric perspective. *Renewable and Sustainable Energy Reviews* **2021**, *138*, 110521.
3. Pasha, M.; Zhang, H.; Shang, M.; Li, G.; Su, Y. CO2 absorption with diamine functionalized deep eutectic solvents in microstructured reactors. *Process Safety and Environmental Protection* **2022**, *159*, 106-119.
4. Jafari, K.; Fatemi, M.H.; Lugo, L. An experimental study of novel nanofluids based on deep eutectic solvents (DESs) by Choline chloride and ethylene glycol. *Journal of Molecular Liquids* **2022**, *360*, 119521.
5. Hansen, B.B.; Spittle, S.; Chen, B.; Poe, D.; Zhang, Y.; Klein, J.M.; Horton, A.; Adhikari, L.; Zelovich, T.; Doherty, B.W.; et al. Deep Eutectic Solvents: A Review of Fundamentals and Applications. *Chemical Reviews* **2021**, *121*, 1232-1285.
6. Alizadeh, V.; Esser, L.; Kirchner, B. How is CO2 absorbed into a deep eutectic solvent? *The Journal of Chemical Physics* **2021**, *154*, 094503.
7. Aldawsari, J.N.; Adeyemi, I.A.; Bessadok-Jemai, A.; Ali, E.; AlNashef, I.M.; Hadj-Kali, M.K. Polyethylene glycol-based deep eutectic solvents as a novel agent for natural gas sweetening. *PLOS ONE* **2020**, *15*, e0239493.
8. Zhang, Y.; Ji, X.; Lu, X. Choline-based deep eutectic solvents for CO2 separation: Review and thermodynamic analysis. *Renewable and Sustainable Energy Reviews* **2018**, *97*, 436-455.
9. Lu, H.; Liu, Y.; Chinnathambi, A.; Almoallim, H.S.; Jhanani, G.K.; Brindhadevi, K.; Boomadevi, P.; Xia, C. Production and utilization of the Chlorella vulgaris microalgae biochar as the fuel pellets combined with mixed biomass. *Fuel* **2024**, *355*, 129395.
10. Jin, X.; Gong, S.; Chen, Z.; Xia, J.; Xiang, W. Potential microalgal strains for converting flue gas CO2 into biomass. *Journal of Applied Phycology* **2021**, *33*, 47-55.
11. Lee, S.Y.; Khoiroh, I.; Vo, D.-V.N.; Senthil Kumar, P.; Show, P.L. Techniques of lipid extraction from microalgae for biofuel production: a review. *Environmental Chemistry Letters* **2021**, *19*, 231-251.
12. Hepburn, C.; Adlen, E.; Beddington, J.; Carter, E.A.; Fuss, S.; Mac Dowell, N.; Minx, J.C.; Smith, P.; Williams, C.K. The technological and economic prospects for CO2 utilization and removal. *Nature* **2019**, *575*, 87-97.
13. Pourjamshidian, R.; Tehran, U.o.; Abolghasemi, H.; Tehran, U.o.; Esmaili, M.; Tehran, U.o.; Amrei, H.D.; Bojnord, U.o.; Parsa, M.; et al. CARBON DIOXIDE BIOFIXATION BY Chlorella sp. IN A BUBBLE COLUMN REACTOR AT DIFFERENT FLOW RATES AND CO2 CONCENTRATIONS. *Brazilian Journal of Chemical Engineering* **2019**, *36*, 639-645.
14. Cheah, W.Y.; Show, P.L.; Chang, J.-S.; Ling, T.C.; Juan, J.C. Biosequestration of atmospheric CO2 and flue gas-containing CO2 by microalgae. *Bioresource Technology* **2015**, *184*, 190-201.

15. Anyaoha, K.E.; Krujatz, F.; Hodgkinson, I.; Maletz, R.; Dornack, C. Microalgae contribution in enhancing the circular economy drive of biochemical conversion systems – A review. *Carbon Resources Conversion* **2024**, *7*, 100203.
16. Imani, M.; Tahmasebpoor, M.; Sánchez-Jiménez, P.E.; Valverde, J.M.; Moreno, V. Improvement in cyclic CO2 capture performance and fluidization behavior of eggshell-derived CaCO3 particles modified with acetic acid used in calcium looping process. *Journal of CO2 Utilization* **2022**, *65*, 102207.
17. Razzak, S.A.; Hossain, M.M.; Lucky, R.A.; Bassi, A.S.; de Lasa, H. Integrated CO2 capture, wastewater treatment and biofuel production by microalgae culturing—A review. *Renewable and Sustainable Energy Reviews* **2013**, *27*, 622-653.
18. Bhola, V.; Swalaha, F.; Ranjith Kumar, R.; Singh, M.; Bux, F. Overview of the potential of microalgae for CO2 sequestration. *International Journal of Environmental Science and Technology* **2014**, *11*, 2103-2118.
19. Brettfeld, E.G.; Popa, D.G.; Dobre, T.; Moga, C.I.; Constantinescu-Aruxandei, D.; Oancea, F. CO2 Capture Using Deep Eutectic Solvents Integrated with Microalgal Fixation. *Clean Technologies* **2024**, *6*, 32-48.
20. González-Rivera, J.; Husanu, E.; Mero, A.; Ferrari, C.; Duce, C.; Tinè, M.R.; D'Andrea, F.; Pomelli, C.S.; Guazzelli, L. Insights into microwave heating response and thermal decomposition behavior of deep eutectic solvents. *Journal of Molecular Liquids* **2020**, *300*, 112357.
21. Sarmad, S.; Nikjoo, D.; Mikkola, J.-P. Amine functionalized deep eutectic solvent for CO2 capture: Measurements and modeling. *Journal of Molecular Liquids* **2020**, *309*, 113159.
22. Gautam, R.; Kumar, N.; Lynam, J.G. Theoretical and experimental study of choline chloride-carboxylic acid deep eutectic solvents and their hydrogen bonds. *Journal of Molecular Structure* **2020**, *1222*, 128849.
23. Sarmad, S.; Xie, Y.; Mikkola, J.-P.; Ji, X. Screening of deep eutectic solvents (DESs) as green CO2 sorbents: from solubility to viscosity. *New Journal of Chemistry* **2017**, *41*, 290-301.
24. Samorì, G.; Samorì, C.; Guerrini, F.; Pistocchi, R. Growth and nitrogen removal capacity of Desmodesmus communis and of a natural microalgae consortium in a batch culture system in view of urban wastewater treatment: Part I. *Water Research* **2013**, *47*, 791-801.
25. Gao, J.; Jebrane, M.; Terziev, N.; Daniel, G. Evaluation of Wood Quality Traits in Salix viminalis Useful for Biofuels: Characterization and Method Development. *Forests* **2021**, *12*.
26. Palanisami, S.; Lee, K.; Balakrishnan, B.; Nam, P.K.-s. Flue-gas-influenced heavy metal bioaccumulation by the indigenous microalgae Desmodesmus communis LUCC 002. *Environmental Technology* **2015**, *36*, 463-469.
27. Vanags, J.; Kunga, L.; Dubencovs, K.; Galvanauskas, V.; Grīgs, O. Influence of Light Intensity and Temperature on Cultivation of Microalgae Desmodesmus Communis in Flasks and Laboratory-Scale Stirred Tank Photobioreactor. *Latvian Journal of Physics and Technical Sciences* **2015**, *52*, 59-70.

USE OF HYDROGEN MIXED WITH NATURAL GAS IN INDUSTRIAL AND LOCAL NETWORKS

Iuliana CRISTEA[1], Timur CHIS[2*], Laurențiu PRODEA[3]

[1]Ph. D. School, Oil and Gas University, Ploiești, Romania,

[2] Oil and Gas Engineering Department, Oil and Gas University, Ploiești, Romania

[3]Mechanical Engineering Department, Lucian Blaga University, Sibiu, Romania

Abstract

Hydrogen gas pipelines are technically feasible and have operated for decades in various locations, including the US, Germany, the Netherlands, France, and Belgium. However, the scale of these pipeline systems could be improved, and they need to provide an extensive basis for the modernization and rapid growth of the implementation of new hydrogen transport systems. In some parts of the world, significant infrastructure exists for transporting and distributing natural gas. Such infrastructure can facilitate low-cost transportation, distribution, supply, and hydrogen storage. The article presents the natural gas-hydrogen blending projects in Europe under study.

Key words: Natural gas, hydrogen, blending

1. Introduction

Hydrogen and natural gases have different physicochemical characteristics (calorific value, flow properties, density, flame propagation speed, combustion properties, heat characteristics, and network interaction).

Experiments have shown that mixing hydrogen into the natural gas stream slightly changes its characteristics, but this process should not be a barrier if a program is established to decarbonize the gas network step-by-step.

Hydrogen is lighter than air, highly flammable, easy to ignite, heats up at low pressure, and is one of the most challenging gases when sealing vessels, pipes, or equipment.

Hydrogen burns in the air with a pale blue, almost invisible flame that increases the risk of injury in a fire.

* Corresponding author: timur.chis@gmail.com

The lower and upper flammability limits in air are 4% and 75%. Hydrogen-air mixtures are extremely easy to ignite, requiring only 0.017 mJ of ignition energy, compared to 0.25 mJ for hydrocarbons.

The maximum flame propagation rate is up to 3 m/sec in air [1].

The realization of hydrogen-compatible gas transport networks involves a series of adaptations and problems to be addressed and solved for each of their components, which include the transport and distribution network and storage and utilization facilities.

Several important elements regarding the gas network are the material from which the pipe is made, polyethylene vs. steel, compressors, regulating, measuring, and safety equipment, and mixture levels, all of which must be adjusted to transport a mixture of hydrogen and natural gas.

Another issue to address is seasonal, long-term underground storage. Salt caverns are considered more suitable than porous structures. Several such facilities are currently in operation for the storage of pure hydrogen, but existing geological facilities must be adapted to store natural gas-hydrogen mixtures or pure hydrogen.

Natural gas/hydrogen mix in existing infrastructure [2].

Mixing natural gas with hydrogen is carefully researched and studied throughout the European Union. This combination of the two gases is believed to reduce the greenhouse effect produced by fossil fuels, mainly when hydrogen is obtained through renewable sources. The mixture obtained from the two gases is intended to be transported and distributed to consumers through the existing infrastructure.

It is widely accepted that, in theory, pipeline systems can be converted from natural gas to hydrogen gas, and the investment to do so can be minimal compared to building a hydrogen-only infrastructure from scratch, depending on the various specific situations.

The fit of transport and distribution systems varies from case to case; for example, plastic pipes are generally suitable for hydrogen gas.

The main challenge lies in the work that has to modify or replace the equipment in the gas industry in order to be able to use the gas-hydrogen mixture. International standards limit the amount of hydrogen that can be introduced into natural gas pipeline systems.

2. Materials and Methods

A recent study in the Netherlands concludes that its gas pipelines can be converted for hydrogen gas by replacing gas compressors and seals.

Likewise, in Great Britain, detailed studies are conducted, which take into account the fragility of the current high-pressure natural gas transport

pipelines if they will transport pure hydrogen and the changes that must be made to the operating and safety regulations.

The presence of hydrogen in the existing natural gas pipelines will cause their walls to be much more strongly influenced by the demands to which they are subjected. The phenomenon is closely related to pressure variations in the pipelines and is essential to analyze and comply with over time.

Research has so far shown that this phenomenon of hydrogen embrittlement does not have as great an influence as originally thought, and the process of transporting hydrogen through the existing pipeline system can be carried out safely and reliably [3].

Currently, acceptable hydrogen mixture volumes of 10 vol.%, 15 vol.%, or values up to a maximum of 30 vol.%, are considered feasible for certain appliances, stoves, and boilers used in local applications.

Problems may arise in some industries, such as chemical companies, that use hydrogen as a raw material for production. Moreover, separation technologies must be developed and implemented to allow the extraction of hydrogen or methane from the gas mixture to accommodate different end-user compatibilities.

Developed countries have prioritized driving down costs in the production of hydrogen from renewable sources. The gradual increase in the share of hydrogen that the gas infrastructure can accommodate may provide long-term friendly signals for the large-scale deployment of electrolytic hydrogen from renewable electricity.

These changes must be analyzed and put into practice after careful assessment to analyze whether the facilities and equipment, including end-use ones such as boilers, gas turbines, and cooking appliances, could support such a transition.

Hydrogen gas is the lightest element; it is colorless, odorless, tasteless, non-toxic, and non-poisonous; it is not corrosive but can embrittle some metals. Natural gases are odorized with ethyl mercaptan to detect their leakage, but in the case of hydrogen, no odorants are light enough to mix and obtain the same dispersion rate. In an outdoor environment, hydrogen has the advantage of being 14 times lighter than air; it will quickly disperse into the air. In a closed environment, hydrogen, a tiny molecule with low viscosity, is prone to leaks; these are a concern, being impossible to detect by human senses and having that extensive flammability range. Adequate ventilation and detection sensors can be safety measures in using hydrogen [4].

Hydrogen has a high energy content by weight rather than by volume, presenting a particular challenge for storage. Hydrogen gas is compressed and stored at high pressures in order to store it. For safety, the hydrogen tanks will be equipped with pressure reduction devices to prevent the increase above the permissible limit.

The auto-ignition temperatures of the two gases are close, as seen in the previous table. The auto-ignition temperature of a substance is the lowest temperature at which it will ignite spontaneously without the presence of a flame or spark. In daylight, the pale blue flame of hydrogen is almost invisible, so both hydrogen detectors and flame detectors are almost always installed with hydrogen systems. Liquid hydrogen has different characteristics than gaseous hydrogen and presents additional potential hazards. It is stored at -245°C, pressure up to 1000 kPa (150 psi). The volume ratio of liquid to gas is about 1:848, so leaking liquid hydrogen is extremely dangerous.

Mixing natural gas with hydrogen requires thorough study and research due to the different physicochemical characteristics (calorific value, flow properties, density, flame propagation speed, combustion properties, heat characteristics, and interaction with the environment in which it is found) (Table 1).

The mixing of hydrogen in the natural gas stream is known to slightly change the characteristics of the gas. However, this process should not be a barrier if a program is established by gradually decarbonizing the gas network [5].

Table 1

Hydrogen-methane comparison

Property	U.M.	Methane	Hydrogen	Comparasion H_2
Density	Kg/m^3	0,68	0,09	1/8 of methane
Molecular mass	Kg/kmol	16,043	2,016	1/8 of methane
Flash domain	%	4,4 -17	4 – 75	*6 of methane
Laminar burning speed	m/s	0,4	3,1	*8 of methane
Minimum ignition energy	mJ	0,210	0,016	1/13 of methane
Auto ignition temperature	°C	600	560	
Superior caloric value	MJ/m^3	39,8	12,7	1/3 of methane
Inferior caloric value	MJ/m^3	25,8	10,8	1/2,5 of methane
Superior caloric value	MJ/kg	55,5	141,7	*3 of methane
Inferior caloric value	MJ/kg	50.0	120,0	*2,5 of methane
Combustion temperature	°C	1946	2101	whith 155°C of methane
The minimum amount of O_2	mol/mol	2,0	0,5	1/4 of methane
The minimum amount of air	mol/mol	9,52	2,38	1/4 of methane
Fuel air stoichiometry	$Kg_{comb.}/kg_{aer}$	0,058	0,029	1/2 of methane
Methane index	%	100	0	-
Melting temperature	°C	-182,5	-259,35	cu 77°C of methane
Boiling temperature	°C	-164	-252,9	Cu 88°C of methane
Solubity in water	Vol/Vol	0,054	0,0214	1/2 of methane
Difusivity in air	cm^2/s	0,2	0,63	*3 of methane

A challenge will be keeping the percentage of hydrogen constant across the grid throughout the year due to fluctuating renewable, wind, and solar power sources, which lead to varying levels of output [6].

In the first phase, it is necessary to take into account priorities for research and development of testing techniques to accurately identify the impact of hydrogen on materials, as well as remedial techniques for phenomena such as steel quality, welded joints, embrittlement, and crack propagation, as well as the quality of the existing materials in the distribution network.

In order to answer as many of these questions and others as possible, work is being done through various pilot projects, especially in Germany, the Netherlands, and Great Britain, but also in other parts of Europe (France et al., the Netherlands).

Following the studies and the specialized literature, the following advantages and disadvantages were found in reusing the pipes.

In the case of existing gas pipelines, the main strengths are related to the need for limited pipeline modifications, namely the installation of new hydrogen-adapted compression stations and gas pressure regulation stations [6].

Furthermore, the cracking of the material can be reduced when operating under static load. The accelerated rate of crack expansion will hurt the strength of the material, thus influencing the cost of maintenance and operation of the pipeline.

Another under-researched method may be to protect surfaces by coating.

This process is well known but has no usable on-site procedures that could be applied to coating already installed pipelines. In this case, the procedure would require the excavation of the existing pipes, which would lead to a complex and expensive process.

The use of inhibitors leads to a process similar to the coating procedure because the mixture of inhibitors prevents hydrogen adsorption to the pipe material. Inhibitors can be easily mixed into the hydrogen stream.

This procedure presents toxicity and safety risks associated with each type of inhibitor used.

Depending on the subsequent processing and application of hydrogen, an additional purification step may be required [7].

In the case of the pipe-in-pipe procedure, the benefits of two pipes are combined, the one on the outside having the role of safety and the one on the inside specially designed for hydrogen transport.

This would involve an expensive approach, as additional efforts would be required to install it in existing pipes.

It would require excavation of the pipes, thus leading to a complex and expensive process, as in the case of surface coating [8].

By simulating several economic indicators, it was concluded that using pipelines in hydrogen transport can reduce costs by up to 60%.

An analysis at the level of Germany and pipeline availability constraints for 2030 shows a 30% reduction in transport system costs compared to a new hydrogen pipeline system.

Close cooperation between legislators, investors, infrastructure operators, and the hydrogen industry is needed to correct the necessary developments and ensure that project deadlines are met (Table 2).

Due to the ever-increasing demand for energy, in the context of reducing greenhouse gases and considering the long-term climate objectives of the EU in recent years, more and more projects on mixing hydrogen with natural gas have been implemented.

Hythane comes from the English language of the two gas components, hydrogen, and methane, and refers to a fixed fraction of hydrogen mixed with natural gas.

This term originated around the 2000s in studies that referred to the effect of hydrogen addition on the performance of methane-fueled vehicles.

Those who introduced the term see it as a transition gas based on a cheap and proven technology that can contribute to a 50% reduction in NOx emissions.

Table 2

Advantages and disadvantages of pipeline reuse in the transport of natural gas-hydrogen mixture

Reuse option	Advantajes	Disadvantajes
Natural gases used	Not much is needed. Limited material cracking under static load.	Increased material degradation.
Coating pipes	A specific protective layer against embrittlement caused by hydrogen. Industrial processes developed on metal surfaces	No on-site coating procedures are known Excavation of pipes will probably be required.
Inhibitors (O_2, CO, SO_2)	Limited changes are required. The protective layer undermines hydrogen permeability.	Safety and toxicity risks. Purity requirements for hydrogen and fuel cell processing.
Pipe-in-pipe	A mix of benefits for inner and outer pipe	Additional material required. Excavation of pipes will probably be required.

The mixture of 20% hydrogen by volume with Hythane® brand natural gas has been extensively evaluated and demonstrated in Montreal (Canada) in the EURO – Québec project scope (Figure 1).

Two buses from NOVABUS ran in the city for nine months. Following the project, the 20% hydrogen mixture recorded CO2 emissions reduced by 7.5% through increased efficiency. NOx- emissions were reduced by 40% without any increase in unburned hydrocarbons in the exhaust gases.

SUNLINE later operated these buses in Palm Springs (California), and no incident was reported.

Fig. 1. Hydrogen pumps

In Europe, this term is related to the ALT-HY-TUDE1 project implemented in France. In this project, this innovative fuel mixture of natural gas and hydrogen Hythane® was proposed as a relevant and pragmatic transition solution to introduce hydrogen into the transport system massively, taking advantage of synergies with compressed natural gas technology and infrastructure.

Another demonstration of Hythane® was held in Malmö (Sweden).

In this project, hydrogen represents only 8% vol., mixed with natural gas, without changing the VOLVO engine.

As no problem was recorded, the mixture will be tested with 20-25% hydrogen in the next stage of the demonstration.

HENG (Hydrogen et al.), first mentioned in the US in 2010, addresses two dominant energy and environmental issues: decarbonization and improved energy management.

In theory, HENG hydrogen-enriched natural gas typically contains 10-20% hydrogen by volume and is compatible with existing gas transportation and distribution infrastructure and end-use.

Blending hydrogen with natural gas is an exciting bridge between our past and future, HENG, being part of efforts to build a low-carbon future for humanity.

This gaseous mixture, called HENG, makes it possible to reduce emissions, improve the efficiency of equipment end-use, and decrease the global carbon

intensity of natural gases. HENG uses existing natural gas pipelines and regional or municipal delivery systems [8].

3. Results and Discussion

In previous projects from Germany, Great Britain, the USA, and Holland, which were implemented, the effects of mixing natural gas with hydrogen were demonstrated on real, existing natural gas networks.

The effects on the materials were followed to determine how higher hydrogen concentrations could affect the network, operational safety, the behavior of the mixture inside the pipe, and compatibility with domestic equipment. Preventive measures for each failure were also examined.

Currently, less than half of the member states of the European Union allow hydrogen to be mixed with natural gas in tiny proportions, between 10% and 2%, and only four countries (Belgium et al.) have exclusively hydrogen pipelines without being connected to SNT and used in limited industrial applications, such as refining.

Producing 1 kg of hydrogen by electrolysis requires about 9 liters of water; water is used directly as a raw material and indirectly as a coolant for the thermoelectric generation of electricity, which is needed to transport, distill, and electrolyze some parts of the water used as a raw material.

The raw material must be pure, and the water used for cooling can be fresh or saline, which does not require desalination or purification.

Considering the potential impact of renewable hydrogen production on water sources, a sustainability criterion that considers high biodiversity sites, falling water levels, and available water remaining on the river body after needs have been met would be helpful.

Hydrogen can be considered a good fuel due to its properties:

- Its use as an energy source does not produce greenhouse gases; the only by-product is water;
- Can be used to produce other gases as well as liquid fuels;
- The existing infrastructure for gas transport and storage can be reused in the hydrogen-natural gas mixture;
- It has a higher energy density than batteries and can be used for long-distance or high-tonnage transport.

Theoretically, hydrogen can be mixed with natural gas for a 10-20% volume share without significant technical challenges and principal investments. In EU member states, the allowed concentration of hydrogen varies between 0.1% by volume and 10% by volume.

Currently, in order for the hydrogen-natural gas mixture to expand and become a solution for reducing CO_2 emissions, the following is being pursued:

-Developing technologies to limit the impact of hydrogen on the materials it comes into contact with;

- Identification and development of new optimized materials for hydrogen transport and its mixing;
- Realization or adaptation of instruments for detecting hydrogen losses or due to their presence;
- Development of real-time energy content assessment methods for calculating the energy input in hydrogen-natural gas mixtures, as well as metrological norms for checking gas concentrations and potential deviations in dynamic conditions;
- Making equipment for injecting hydrogen and mixing it with natural gas;
- Develop pilot projects for both hydrogen blending and pure hydrogen pipelines.

The transformation of natural gas into hydrogen through gas reforming with carbon dioxide capture and sequestration and the transformation of renewable energy into hydrogen through electrolysis allows energy consumers to obtain cost reductions only if the existing natural gas infrastructure is used.

In the case of used pipelines, as is the case of pipelines in Romania that have exceeded their service life, they are susceptible to being in the critical zone; the hydrogen tolerance must be checked individually, and in the case of critical results, to be specified method of intervention.

Decarbonising the grid and accelerating the transition to blending natural gas with hydrogen for domestic applications requires energy policies that support manufacturers' introduction of large-scale domestic gas applications and allow future hydrogen enrichment of more than 20%.

Several projects around the world have demonstrated that at 20 hydrogen, the existing gas network does not require much modification, and the short-term effect of the mixture on materials is not to be worried about. What has yet to be proven is the long-term effect this mixture of hydrogen and natural gas has on materials and equipment, complicating planning for large-scale blends by industry utilities.

It has been demonstrated in the specialized literature that the impact on some gas quality criteria related to combustion (relative density, net and gross calorific values , and the Wobbe index) of the mixture of gases and hydrogen changes as follows:

- As the hydrogen concentration increases, the calorific value decreases linearly. Compared to methane, the lower calorific value and higher calorific value for pure hydrogen decrease to 30% and 32%, respectively;

- The relative density of hydrogen is about eight times lower than that of methane, resulting in a change in the Wobbe index. The decrease from pure methane to pure hydrogen is less severe, as the change in calorific value is largely counteracted by the change in densities;
- The difference in Wobbe indices between CH4 and H2 is only about 9.5%, while the change in calorific value is about 68%;
- The Wobbe index does not decrease over the entire range of mixture space. Instead, it increases with increasing hydrogen concentrations for very high hydrogen fuel mixtures.

The use of a mixture of natural gas and hydrogen aims to decarbonize the natural gas network, primarily if the hydrogen is obtained through renewable sources.

The EU's proposed target is an annual green hydrogen production of 1 million tons in 2024 and 10 million tons in 2030.

4. Data Availability

The data presented in this article is real and collected from the area of interest.

The data can be used by anyone in accordance with applicable international regulations. Data is available in the article and can be provided upon request.

5. Conflicts of Interest

No data or information is presented that could endanger companies or commercial or public companies. There are no conflicts regarding the exposed data. The data taken from the soil samples analyzed and presented in the article are part of oil fields abandoned and handed over to the public domain.

The authors did not benefit from public, private or other resources.

To carry out the research, the authors used the resources provided by University of Petroleum-Gas Ploiesti for the gas properties, equipment by the samples taken and the interpretation of the results.

REFERENCES

[1] https://cdn.wwf.ro/uploads/2023/01/26162703/WWF-Romania-si-Bankwatch_Analiza-Hidrogen.pdf

[2] http://stiintasiinginerie.ro/wp-content/uploads/2014/01/16-ANALIZA-DIFERITELOR-METODE-DE-OB%C5%A2INERE.pdf
[3] Iordache I., Stefănescu I. Obținerea hidrogenului, metode și procedee. AGIR, 2011.
[4] Gupta R.B., Hydrogen Fuel, Production, Transport, and Storage, CRC Press, US, 2009.
[5] Muritala I.K., Guban D., Roeb M., Sattler C., High temperature production of hydrogen: Assessment of non-renewable resources technologies and emerging trends, International Journal of Hydrogen Energy, (2020).
[6] https://www.europarl.europa.eu/factsheets/ro/sheet/62/energia-nucleara.
[7] Martinez-Burgos W.J., Souza Candeo E., Medeiros A.B.P., Carvalho J.C., Andrade Tanobe V.O., Soccol C.R., Bittencourt Sydney E., Hydrogen: Current advances and patented technologies of its renewable production, Journal of Cleaner Production,2021.
[8] Kaur R., Gera P., Jha M.K., Bhaskar T., Biohydrogen (Second Edition) Biomass, Biofuels, Biochemicals, Elsevier, UK, 2019.

EFFECT OF AXIAL MIXING IN MODELLING OF THREE PHASES STEADY STATE GASOLINE HYDROFINING

Laura PETRAS[1,2], Claudia KONCSAG[3], Oana Cristina PÂRVULESCU[1] Tănase DOBRE[1], Iuliana DELEANU[1], Cristian Eugen RĂDUCANU[1]

[1]*Chemical and Biochemical Engineering Department, University POLITEHNICA of Bucharest, 1-7 GheorghePolizu Str., 011061 Bucharest*
[2]*Petromidia Refinery, Navodari Bld 214, Navodari 905700*
[3]*Chemistry and Chemical Engineering Department, Ovidius University 124 MamaiaBld 900527*

Abstract
The reducing as much as possible of the size of a three-phase model of gasoline hyro-refining obliges to accept a cocurent plug flow structure for gas and liquid. The real flow of gas phase and liquid over the fixed bed expressing the catalyst can be considered accepting that each fluid phase flow is affected by axial dispersion. The stationary model thus developed contains a system of five two order differential equations coupled with mass transfer equations for H_2 and H_2S and the S compound whose concentrations on catalyst surface are controlled by chemical reaction

Key words: gasoline hydrofining, three phase model, species mass transfer, catalysis

1. Introduction

Gasoline hydrofining represents the catalytic hydrogenation of commercial gasoline in order to remove sulfur and nitrogen compounds and also to reduce the gasoline content in unsaturated hydrocarbons (alkenes and aromatics). In gasoline hydrofining with suitable catalysts and hydrogen excess, it was found that compounds with nitrogen are hydrogenated faster than those with sulfur. If we also consider that on the catalyst the hydrogenation rates of alkyl sulfides, alkyl disulfides respectively, of aromatic sulfur compounds are the same then we can reduce the hydrofining to a simplified process where we remove the sulfur compounds as a single compound [1,2].

2. Mathematical modeling

In three phases model of hydrofining the catalyst (solid phase) is covered by liquid (liquid phase) which is surrounded by the gas phase, which can be considered as the continuous phase [3]. Considering that at catalytic surface the sulfur compound is converted to hydrogen sulfide the process becomes a complex reaction diffusion process where H_2 and H_2S pass in counter current the liquid and gas phase films towards the catalytic surface where H_2 is consumed and H_2S is generated. Figure 1 shows haw we imagine the H_2 and H_2S concentration state in a local hydrofining location. In more cases related with this described process it accepts the following assumptions:(1) The reactor operates in steady state condition; (2) Gas and liquid flows concurrently: (3) Gas and liquid velocities are constants through the reactor:(4) Constant density of gas and liquid phases: (5) For gas and liquid flow there are not radial dispersion whereas axial dispersion affect the both phases, with D_G and D_L axial dispersion coefficient for gas respectively liquid ; (6) Vaporization and condensation of oil do not take place;

*Corresponding author: email address: laurapetras@yahoo.com

(7) Chemical reaction take place only at the solid catalyst, where S is converted by H_2 to H_2S.
A balance for H_2, H_2S and S compounds respect to a small control volume with dimension *Sdz* , at *z* position in column, leads to the characteristic equations (1) - (5). In order to obtain the surface reaction concentration of reactive species (H_2, H_2S, S compounds) the steady state of process imposes the equality of surface reaction rate with liquid phase species transport rate toward surface. The relations (6) – (8) show that. Now if ad to above partly differential equations the univocity conditions (9) - (15) then it obtains final expression of three phases hydrofining model with axial mixing flow of liquid and gas.

$$\frac{w_g}{RT}\frac{\partial P_{H2}}{dz} = \frac{D_G}{RT}\frac{\partial^2 P_{H2}}{\partial z^2} - K_{cgH2}\sigma_{gl}\left(\frac{P_{H2}}{H_{H2}} - c_{H2l}\right) \quad (1)$$

$$\frac{w_g}{RT}\frac{\partial P_{H2S}}{dz} = \frac{D_G}{RT}\frac{\partial^2 P_{H2S}}{\partial z^2} K_{cgH2S}\sigma_{gl}\left(C_{H2Sl} - \frac{P_{H2S}}{H_{H2S}}\right) \quad (2)$$

$$w_l\frac{\partial C_{H2l}}{dz} = \frac{D_L}{RT}\frac{\partial^2 C_{H2l}}{\partial z^2} K_{cgH2}\sigma_{gl}\left(\frac{P_{H2}}{H_{H2}} - C_{H2l}\right) - K_{lH2}\sigma_{sl}(C_{H2l} - C_{H2s}) \quad (3)$$

$$w_l\frac{\partial C_{H2Sl}}{dz} = \frac{D_L}{RT}\frac{\partial^2 C_{H2Sl}}{\partial z^2} - K_{cgH2S}\sigma_{gl}\left(C_{H2Sl} - \frac{P_{H2}S}{H_{H2S}}\right) + K_{lH2S}\sigma_{sl}(C_{H2Ss} - C_{H2Sl}) \quad (4)$$

$$w_l\frac{dC_{Sl}}{dz} = \frac{D_L}{RT}\frac{\partial^2 C_{Sl}}{\partial z^2} - k_{lS}\sigma_{sl}(C_{Sl} - C_{Ss}) \quad (5)$$

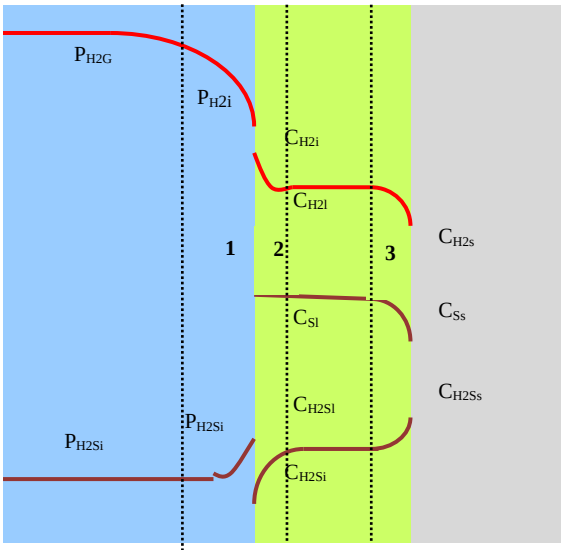

Fig. 1. Concentration profiles for H_2 and H_2S in hydrofining

$$\rho_{vc}v_R(C_{Ss}, C_{H2s}, T) = K_{lH2}\sigma_{sl}(C_{H2l} - C_{H2s}) \quad (6)$$

$$\rho_{vc}v_R(C_{Ss}, C_{H2s}, T) = 0.5K_{lH2S}\sigma_{sl}(C_{H2Ss} - C_{H2Sl}) \quad (7)$$

$$\rho_{vc}v_R\big(\rho_{vc}v_R(C_{Ss}, C_{H2s}) = k_{lS}\sigma_{sl}(C_{Sl} - C_{Ss})\big) = k_{lS}\sigma_{sl}(C_{Sl} - C_{Ss}) \quad (8)$$

$$z = 0 \quad w_g(P_{H2e} - P_{H2i}) = -D_G\frac{dP_{H2}}{dz}\ ; \quad z = H \quad D_G\frac{dP_{H2}}{dz} = 0 \quad (9)$$

$$z = 0 \quad w_g(P_{H2Se} - P_{H2Si}) = -D_G\frac{dP_{H2S}}{dz}\ ; \quad z = H \quad D_G\frac{dP_{H2S}}{dz} = 0 \quad (10)$$

$$z = 0 \quad w_l(C_{H2le} - C_{H2li}) = -D_l\frac{dC_{H2l}}{dz}\ ; \quad z = H \quad D_l\frac{dC_{H2l}}{dz} = 0 \quad (11)$$

$$z = 0 \quad w_l(C_{H2Sle} - C_{H2Sli}) = -D_G\frac{dC_{H2Sl}}{dz}\ ; \quad z = H \quad D_l\frac{dC_{H2Sl}}{dz} = 0 \quad (12)$$

$$z = 0 \quad w_L(C_{Sle} - C_{Sli}) = -D_l\frac{dC_{Sl}}{dz}\ ; \quad z = H \quad D_l\frac{dC_{Sl}}{dz} = 0 \quad (13)$$

The expression of reaction rate is characteristic for concrete catalyst case. This expression shows an Arrhenius dependence upon temperature and upon product of

reactants concentration at catalytic site. For Shel DC-2532 a CoMo based catalyst, suited for mild severity operation at low to moderate operating pressure, the reaction rate, in $kmols_r/kg_cs$, are given [4] by relation (14)

$$v_R(\rho_{vc} v_R(C_{Ss}, C_{H2s}) = \frac{4.27\ 10^9 \exp\left(\frac{131990}{RT}\right) C_{Ss} C_{H2s}^{0.45}}{\left(1+41770\ exp\left(\frac{2761}{RT}\right) C_{H2S\ s}\right)^2} \quad (14)$$

3. Simulation results

The specificity of the model is firstly given by the fact that for integration of partly differential equation system from equations (1) – (5) it must solve, at each integration step, the algebraic system from equations (6) – (8). That is to have in model integration current values for C_{Ss}, C_{H2s}, and respectively C_{H2Ss}.Secondly the specificity is given by the fact that the partly differential equations present conditions at species input in reactor (z=0) and respectively at species exit from reactors (z= H). So various, but real, initial conditions can be used in process model simulations. For correct simulations first of all it must to correctly assign the computation of total mass transfer coefficient for H_2,K_{cgH2}, for H_2S, K_{cgH2S} and for partly mass transfer coefficient of sulfur compounds from liquid to catalyst, k_{lS}. Due to the fact that the hydrodynamics and species diffusion coefficient determine the value of mass transfer coefficients we can approximates the following values:$K_{cgH2} = 5\ 10^{-5}$ m/s, $K_{cgH2} = 0.8\ 10^{-5}$ m/s and $k_{lS} = 1.2\ 10^{-5}$ m/s. Concerning the specific mass transfer surface for gas/liquid, σ_{gl}, and liquid solid, σ_{sl}, for phases contacting, the best simple consideration is in accepting theirs equality and theirs determination upon catalyst particle diameter, That is shown by relation (15). For dispersion coefficients characterizing the gas and liquid phases flow can be assumed the Levenspiel relationship [6], written here, for flow over a spherical catalyst particle having the diameter d_p , as it is shown by relation (16). With table 1 we give data respect to one usual process factors from the above model as well as data regarding the starting conditions of the model integration (values for process variables at the phases input in reactor)

$$\sigma_{gl} = \sigma_{sl} = \frac{6(1-\varepsilon_g-\varepsilon_l)}{d_{pc}} \quad (15)$$

$$Pe_g = \frac{w_g d_p}{D_G} = 2,\ Pe_l = \frac{w_l d_p}{D_L} = 2 \quad (16)$$

Tabel 1

Values of process factors and for initial conditions in model (1) - (13)

	Factor or initial condition name	Symbol	Units	Values
1	Liquid superficial velocity	w_l	m/s	$1.5\ 10^{-5} – 3\ 10^{-5}$
2	Gas superficial velocity	w_g	m/s	$3\ 10^{-4} – 6\ 10^{-4}$
3	Hydrogen gasoline Henry constant [5]	H_{H2}	MPa/($kmols_{H2}$/K $mols_{lq}$)	H_{H2} = exp(2241/T-0.11)
4	Hydrogen sulphide gasoline Henry constant	H_{H2S}	MPa/($kmols_{H2S}$/K $mols_{lq}$)	3.37+0.035(T-413)
5	Working pressure	p	bar	50 - 60
6	Working Temperature	T	^{0}K	653 - 683
7	Bed void fraction	$\varepsilon_g + \varepsilon_l$	m^3/m^3	0.25
8	Liquid void fraction	ε_l	m^3/m^3	0.05
9	Catalyst equivalent diameter	d_{pc}	m	$2.5\ 10^{-4}$
10	Catalyst bulk density	ρ_{vc}	Kg/m^3	830 - 850
11	Estimated catalyst efficiency	η_{efc}	-	0.7 – 0.9

10	Mean mass molecular of gasoline	M_l	Kg/Kmol	140 -200
11	Mean gasoline density	ρ_l	Kg/m^3	840 - 910
12	Initial sulfur content in gasoline	ω_{S0}	$kg_S/kg_{gasoline}$	0.002 -0.003
13	Mole fraction of H_2 in gas feed	y_{H20}	$kmol_{H2}/kmol_{gases}$	1
14	Mole fraction of H_2S in gas feed	y_{H2S0}	$kmol_{H2S}/Kmol_{gases}$	0
15	H_2 concentration in liquid feed	C_{H20}	$kmol_{H2l}/m^3$	0

Figure 2 concentrates the results of one case model integration where process parameters given in table 1 at positions 7 -11 take the values here given. More precisely figure 2 shows the model computed dimensionless species concentration along of catalytic bed having *H* height. The dimensional values of partial pressures and molar concentrations were obtained by dividing the current values resulting from the numerical integration by a maximum value, as it is shown that table 2. It is observed in table 2 that some maximum values of process responses values appear at the input in catalytic bed and at the exit from catalytic bed. In order to highlight the effect of axial mixing, figure 2 also represents (dashed lines) the case where the phase flow is with total displacement pure, so D_G and D_l go to zero In figure 2 the graphic representation type was chosen in order to have all responses in a single figure.

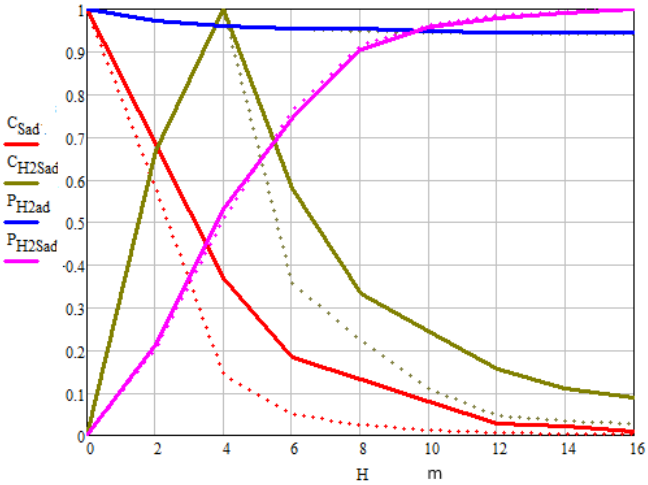

Fig. 2. Evolution of dimensionless process responses for an imposed height of catalyst bed (T= 650 ^{0}K, p= 55 bar, w_l= 2 10^{-5} m/s, w_g=4 10^{-4} m/s, dashed lines: without axial mixing)

Table 2

Maximum values for process responses used for their dimensionless expression

	C_{Smax}	C_{H2Smax}	P_{H2max}	P_{H2Smax}	C_{H2lmax}
Units	kmol/L	kmol/L	MPa	MPa	Kmols/L
Values	0.038	0.00012	5.35	0.00985	0.347
Position	Bed input	H=4 m (Fig.2)	Bed input	Bed exit	Bed exit

Respect to data from figure 2 we note that: i) the effect of axial mixing in the gaseous phase is weak, practically the curves for the partial pressure of hydrogen and for the partial pressure of hydrogen sulfide overlap those specific to the case D_G =0; it is possible that the very high values of the partial pressure of hydrogen and respectively very low values of hydrogen sulfide mask the axial mixing, ii) the effect of axial mixing in the liquid phase is important, finding at the exit from the column (H=16m) a concentration of sulfur compounds and of hydrogen sulfide, quite a lot, over the specific one of the process simulation without considering the axial mixing of the phases, iii) sulfur is removed from gasoline

from 0.038 mol/l to 0.00009 mol/l, without axial mixing, respectively 0.00012 mol/l , when axial mixing is considered, in a fixed bed three phases reactor, with a MoCo catalyst, with a length of 16 m; iv) the intensity of the process seems to be very high in the first 6 m of the reactor; v) the slow decrease of P_{H2} in the reactor is the effect of use in reaction of a big hydrogen excess; vi)the evolution of the H_2S concentration in liquid highlights its rapid generation by reaction (see C_{H2s} value at 4 m) and the fact that its transfer from liquid to gas is quite slow,

4. Conclusions

It has shown that through simplifying modelling based on technologically acceptable considerations, an interesting mathematical model is obtained for gasoline hydrorefining in a three-phase catalytic system.

For numeric integration of model, the calculation expressions are proposed for its parameters, so that it can express the concentration profile of process participants along the catalyst bed.

The example considered in this paper shows that the liquid axial mixing is important so for sulfur advanced removal from gasoline, despite of the fact that process occurs very intense in the first meters of reactor, a very high catalytic bed is required.

REFERENCES

[1] Jimenez F., Nunez M., Kafarov V., *Study and modeling of simultaneous hydrodesulfurization, hydrodenitrogenation and hydrodearomatization on vacuum oil hydrotreatment*, European Symposium on Computer Aided Processes, Editors Pujganer I., Espuna A., Elsevier Science, 2005

[2] Babich, I. V.; Moulijn, J. A. *Science and technology of novel processes for deepdesulfurization of oil refinery streams*: A review, Fuel, 82, 607−631, 2003

[3] Chowdhury R., Pedernera E., Reimert R., *Trickle-bed reactor model for desulfurization and dearomatization of diesel*, AIChE J. 48, 126. 2004,

[4] Baloochy B., Shokri S., Marvasar A. M., *Design and implementation of simulator for hydrotreating reactor in RTO development*, International Journal Chemical Engineering and Applications, 1,4,287-293, 2010

[5] Saajanlehto, M.; Uusi-Kyyny, P.; Alopaeus, V. *Hydrogen solubility in heavy oil systems: Experiments and modeling.* Fuel, 137, 393−404, 2014

[6] Levenspiel O., *Chemical Reactions Engineering, Chapter: The Dispersion Model*, 3th Edition, Wiley, 1998

THE EFFECT OF ACID TO NATURAL GAS STORAGE ROCKS

Alla ZEINAB[1], Sulaiman Khasro Hamza DZAIY[1], Timur CHIȘ[2*], Laurenţiu PRODEA[3]

[1]Ph.D. School, Oil and Gas University, Ploiești, Romania,

[2]Oil and Gas Engineering Department, Oil and Gas University, Ploiești, Romania,

[3]Mechanical Engineering Department, Lucian Blaga University, Sibiu, Romania

Abstract

Natural gas deposits are energy reservoirs of great importance in providing transitional fuel for a future without harmful emissions for the environment and humanity. However, the productive layers within the gas deposits are characterized by the porous and sealing environment, and the flow of natural gas and associated fluids is complex, productivity being dependent on the movement of fluids through the rock pores and associated phenomena. Exploiting gas deposits located in shale (clays) has brought new challenges in studying their productivity dynamics, with very low permeability being an essential factor in obtaining economic flows. That is precisely why hydraulic fracturing is widely used in the exploitation of natural gas deposits, the role of this technique being to increase the production of natural gas, primarily from unconventional deposits (shale and clay).

Key words: Natural gas, acids, rocks

1. Introduction

About 85% of the world's shale gas wells are drilled through vertical and horizontal wells, from which fissures (crevices) are then developed through multiple fracturing [1].

This constant temperature maintenance means that the natural gas is extracted in the state of gas aggregation without being affected by its passage into the biphasic phase [2].

However, both during the exploitation period (when the water associated with the deposit and especially the well condensate) and during their ascent through the extraction pipes, the temperature changes, and then the condensation of wet gases or even the engagement of liquid fractions in the pores of the productive rocks occurs, leading to a decrease in the amount of extracted gas.

These problems (decrease in the productivity of gas wells, penetration of liquid water into treatment facilities, appearance of cryohydrates, accumulation of liquid in the area of extraction wells) lead to significant economic losses [3].

* Corresponding author: timur.chis@gmail.com

2. Materials and Methods

Acidification aims to increase (increase) the permeability of the rocks around the exploitation well to clean its walls of the materials deposited from the digging mud and cement crusts.

Also, in some deposits, it is desired to remove the salts deposited by the deposit waters in the area of the perforations due to the drop in pressure and temperature in the productive layers.

Hydrochloric acid is used in rocks made up of carbonates (limestone, dolomites) and in rocks with cement in the bonds between rock particles.

The treatment of productive strata with hydrochloric acid (HCl) is based on the reaction between it and calcareous rocks and on the solubility of the reaction products [2]:

$$2HCl+CaCO_3=CaCl_2+H_2O+CO_2 \quad (1)$$

$$4HCl+CaMg(CO_3)_2=CaCl_2+H_2O+CO_2+MgCl_2 \quad (2)$$

Reaction 1 occurs when using hydrochloric acid to increase the permeability of calcareous rocks, and reaction 2 is valid in the case of using hydrochloric acid in the case of dolomitic rocks.

The resulting products ($CaCl_2$, $MgCl_2$) dissolve easily in water, and CO_2 remains dissolved in water or behaves as a free gas.

The cracking process consists of the penetration of the acid solution into the walls of the well, after which it penetrates the pores of the rocks, leading to the dissolution of the consolidating material of the rocks and the increase in the diameter of the pores.

Simultaneously with the reaction of increasing the diameter of the pores and the borehole, the crusts deposited on the walls of the boreholes are also cleaned.

To increase the effect of the acid, a gel (gelled acid) is used as an accompanying agent, its action being extended in the depth of the productive layers by the fact that the acid reacts with the walls of the communication channels, after which their gelation takes place and therefore no longer the reaction continues, the acid penetrating even deeper.

Later, a new batch of hydrochloric acid (multiple acidification) is introduced, increasing the diameter of the momentum and mass transfer channels.

The acidification process consists of a chemical reaction followed by the neutralization of the HCl (hydrochloric acid) solution over time.

The decrease in the concentration of HCl was observed over time, thus creating a model for simulating the concentration of hydrochloric acid depending on the reaction time and the lithology of the rock (Table 1 and Table 2).

Table 1

Reaction between HCl (decrease in concentration) and rock samples, depending on lithology

HCl reaction time, minutes	2	4	6	8	10	20	30	40	50	60	70	80	90
Sample 1	25	60	80	85	90	97	99	100					
Sample 2	20	58	75	77	80	96	97	99					
Sample 3	15	40	55	68	73	95	98	99					
Sample 4	14	30	45	55	65	75	90	95	96	97	100		
Sample 5	13	20	35	40	45	65	88	94	95	96	98	99	100
Sample 6	12	18	30	37	43	55	70	75	80	90	96	98	100
Sample 7	10	16	25	30	45	60	80	85	88	91	98	100	
Sample 8	3	5	8	9	11	20	40	45	50	80	90	96	99
Sample 9	2	4	5	8	10	19	38	44	49	60	65	70	80
Sample 10	1	2	3	5	9	15	25	35	47	55	60	62	70

Table 2

Characteristics of the analyzed samples

Sample	Calk ($CaCO_3$)	Dolomite	Anhydrite	Total	Porosity, %
1	68,00	31,00	0,35	99,35	14,6
2	76,00	15,00	6,00	97,00	8,12
3	88,50	7,00	1,45	96,95	16,50
4	98,20	0,50	0,33	99,03	0,30
5	51,70	35,00	12,7	99,40	1,30
6	41,00	51,00	7,80	99,80	11,30
7	12,00	77,80	9,70	99,50	17,00
8	45,00	40,60	11,30	96,90	4,30
9	2,6,00	60,55	34,00	97,15	3,20
10	6,80	57,80	35,00	99,60	4,55

It is found that the complete neutralization process of hydrochloric acid is 30-50 minutes for limestone and 30-90 minutes for liming with 10-12% SO_4Ca.

The rate of acid neutralization is a function of the amount and quality of acid used per unit area.

In the analysis carried out on some calcareous rocks from the gas exploitation in the Mediaș area, we found that a relationship of the type can be used (Table 3 and Table 4):

$$t = Kd + c \tag{3}$$

Where:
t is the duration of neutralization, minutes,
d - represents the channel diameter, cm,
K is an acid neutralization coefficient
c is a correction coefficient

Table 3

Numerical relationships of hydrochloric acid reaction with rock lithology

Sample	Numerical relationship (y represents decrease in concentration of HCl solution and x represents reaction time between HCl and rock)	R^2
1	$y = -2E\text{-}06x^6 + 0{,}0003x^5 - 0{,}0153x^4 + 0{,}408x^3 - 5{,}8373x^2 + 43{,}246x - 41{,}32$	0,9989
2	$y = -5E\text{-}06x^6 + 0{,}0006x^5 - 0{,}0305x^4 + 0{,}7354x^3 - 9{,}1681x^2 + 57{,}17x - 63{,}211$	0,9992
3	$y = 2E\text{-}06x^6 - 0{,}0002x^5 + 0{,}0061x^4 - 0{,}0468x^3 - 0{,}8426x^2 + 17{,}869x - 16{,}965$	0,9995
4	$y = -5E\text{-}08x^6 + 1E\text{-}05x^5 - 0{,}0011x^4 + 0{,}0513x^3 - 1{,}223x^2 + 15{,}746x - 14{,}356$	0,9974
5	$y = -6E\text{-}09x^6 + 2E\text{-}06x^5 - 0{,}0002x^4 + 0{,}0087x^3 - 0{,}2669x^2 + 6{,}358x + 1{,}2834$	0,9956
6	$y = -1E\text{-}09x^6 + 5E\text{-}07x^5 - 8E\text{-}05x^4 + 0{,}0063x^3 - 0{,}2656x^2 + 6{,}2865x - 0{,}3951$	0,9965
7	$y = -1E\text{-}08x^6 + 2E\text{-}06x^5 - 0{,}0002x^4 + 0{,}0086x^3 - 0{,}2402x^2 + 5{,}8694x - 2{,}3173$	0,9951
8	$y = 1E\text{-}08x^6 - 3E\text{-}06x^5 + 0{,}0003x^4 - 0{,}0149x^3 + 0{,}3208x^2 - 1{,}5906x + 6{,}7297$	0,9918
9	$y = 3E\text{-}09x^6 - 8E\text{-}07x^5 + 9E\text{-}05x^4 - 0{,}0051x^3 + 0{,}1355x^2 - 0{,}2886x + 2{,}8832$	0,9962
10	$y = 2E\text{-}09x^6 - 3E\text{-}07x^5 + 2E\text{-}05x^4 - 0{,}0001x^3 - 0{,}0053x^2 + 0{,}9144x - 1{,}3176$	0,9993

We note that the logarithmic equations of the solution concentration decrease as a function of the reaction time between hydrochloric acid (HCl) and rock have the higher accuracy coefficient, a and b being the correction parameters depending on the concentration in $CaCO_3$ (Table 5).

$$t = a\, ln(d) + b \tag{4}$$

Table 4

Numerical relationships of hydrochloric acid reaction with rock lithology-linear equation

Concentration of $CaCO_3$	The linear equation (t represents the decrease in the concentration of the HCl solution and d represents the reaction time between the HCl and the rock)	R^2
50 %	t = 3,0824d + 15,298	R^2 = 0,9011
60 %	t = 3,0059d + 29,706	R^2 = 0,7796
70 %	t = 8,1453d + 23,633	R^2 = 0,89
80 %	t = 13,261d + 38,005	R^2 = 0,8552

Table 5

Numerical relationships of hydrochloric acid reaction with rock lithology-logaritmic equation

Concentration of $CaCO_3$	The logarithmic equation (y represents the decrease in the concentration of the HCl solution and x represents the reaction time between the HCl and the rock)	R^2
50 %	t = 23,874ln(d) + 8,6561	R^2 = 0,9669
60 %	t = 24,961ln(d) + 20,123	R^2 = 0,9617
70 %	t = 27,41ln(d) + 31,731	R^2 = 0,9962
80 %	t = 27,977ln(d) + 55,407	R^2 = 0,9789

3. Results and Discussion

3.1. The influence of environmental factors on the rate of neutralization of hydrochloric acid, used in the acidification of productive layers in order to increase the recovery factor

3.1.1. Influence of the temperature of the productive layer and/or of the acid solution

Raising the temperature of the acid solution increases the reaction rate between the HCl and the rock.

For this fact, we analyzed the effect of changing the temperature of hydrochloric acid on some collecting rocks.

An increase in the neutralization rate of 1.38-8.67 of the acid solution is observed in the reaction with the analyzed rock, depending on the type of rock and the temperature of the fracturing fluid (Table 6).

3.1.2. The influence of the acid solution on the reaction rate

In industrial practice, acidification of productive layers is carried out with acid solutions containing between 8 and 15%.

Using a solution with a lower concentration requires large amounts of liquid, and cracking occurs only over short distances. In the case of a higher concentration, it will lead to the formation of viscous solutions consisting of $CaCl_2$ and $MgCl_2$, sometimes even leading to pore blocking.

On a calcareous rock, we analyzed the influence of the concentration of hydrochloric acid on the neutralization time.

In this case, we created logarithmic equations to evaluate the behavior of the reaction speed as a function of the concentration of hydrochloric acid (Table 7).

Table 6

Duration of neutralization of a 10% acid solution in contact with reservoir rocks

Sample	50% from the initial concentration			75 % from the initial concentration		
	20 ^{0}C (1)	60 ^{0}C (2)	The report 1/2	20 ^{0}C (1)	60 ^{0}C (2)	The report 1/2
1	13	1,5	8,67	22,1	3,4	6,50
2	4,5	1,8	2,50	7,5	4,7	1,60
3	5,8	3,2	1,81	10,1	5,3	1,91
4	6,2	4,5	1,38	11,3	7,6	1,49
5	14,5	5,8	2,50	24,7	9,2	2,68
6	39	15,8	2,47	55,8	27,4	2,04
7	55	22,4	2,46	85,6	48,9	1,75

Table 7

Numerical relations of reaction of different concentrations of hydrochloric acid with some rocks from the Transylvanian Basin - logarithmic equations

HCl concentration	The logarithmic equation (y represents the decrease in the concentration of the HCl solution and x represents the reaction time between the HCl and the rock)	R^2
5 %	y = 27,64ln(x) + 26,453	R^2 = 0,9679
10 %	y = 17,425ln(x) + 49,362	R^2 = 0,9295
15 %	y = 13,22ln(x) + 57,596	R^2 = 0,8064

3.1.3. The influence of pressure on the reaction rate

During the chemical reaction, CO_2 appears as a result, which can be gas or (under pressure from the productive layers) can dissolve in water (Table 8).

However, releasing CO_2 from the solution will cause the solution to bubble, so some reaction products will separate faster.

Table 8

Numerical relations of reaction of hydrochloric acid with limestone at various values of (Transylvania Basin)

Pressure value (atm)	The polynomial equation (y represents the decrease in concentration of HCl solution and x represents the reaction time between HCl and rock, hours),	R^2
1	$y = 39x + 60$	$R^2 = 1$
5	$y = 6E\text{-}05x^6 + 0{,}0028x^5 - 0{,}1581x^4 + 2{,}5254x^3 - 17{,}931x^2 + 59{,}884x + 5{,}1172$	$R^2 = 0{,}9994$
7,5	$y = 0{,}0008x^6 - 0{,}0274x^5 + 0{,}3426x^4 - 1{,}7879x^3 + 3{,}0092x^2 + 6{,}846x + 4{,}3704$	$R^2 = 0{,}987$
10	$y = 0{,}0006x^6 - 0{,}0208x^5 + 0{,}276x^4 - 1{,}5795x^3 + 3{,}1568x^2 + 4{,}5021x + 2{,}9789$	$R^2 = 0{,}9919$
20	$y = 0{,}0003x^6 - 0{,}0089x^5 + 0{,}0967x^4 - 0{,}3051x^3 - 0{,}8041x^2 + 6{,}3136x + 2{,}1543$	$R^2 = 0{,}9942$
40	$y = 0{,}0002x^6 - 0{,}0056x^5 + 0{,}0506x^4 - 0{,}0562x^3 - 1{,}194x^2 + 5{,}8593x + 1{,}0736$	$R^2 = 0{,}9954$

In both experiments, a 10% HCl solution with 1% formalin was used, the temperature of the solution being 20ºC and using 4.3 ml/cm^2 of rock surface (Table 9). We notice that as the pressure increases, the reaction rate decreases quickly.

Table 9

The numerical relations of the reaction of hydrochloric acid with dolomite at various values of (Transylvania Basin)

Pressure value (atm)	The polynomial equation (y represents the decrease in concentration of HCl solution and x represents the reaction time between HCl and rock, hours),	R^2
1	$y = 10x + 80$	$R^2 = 1$
5	$y = -7E\text{-}05x^6 + 0{,}0132x^5 - 0{,}3828x^4 + 4{,}5955x^3 - 27{,}152x^2 + 80{,}966x - 25{,}1$	$R^2 = 0{,}9985$
6,5	$y = 0{,}0035x^6 - 0{,}1205x^5 + 1{,}5523x^4 - 9{,}1238x^3 + 21{,}3x^2 + 5{,}4458x + 5{,}9$	$R^2 = 0{,}9996$
7,5	$\mathbf{y} = 0{,}0015x^6 - 0{,}0498x^5 + 0{,}6273x^4 - 3{,}8683x^3 + 12{,}119x^2 - 13{,}764x + 13{,}867$	$R^2 = 0{,}9972$
10	$y = -0{,}0004x^6 + 0{,}0149x^5 - 0{,}2117x^4 + 1{,}5027x^3 - 5{,}4099x^2 + 10{,}727x + 1{,}3333$	$R^2 = 0{,}9982$
20	$y = -0{,}0013x^6 + 0{,}0434x^5 - 0{,}587x^4 + 3{,}8717x^3 - 12{,}722x^2 + 20{,}708x - 4{,}3333$	$R^2 = 0{,}9982$
40	$y = -0{,}0019x^6 + 0{,}0647x^5 - 0{,}8722x^4 + 5{,}7616x^3 - 19{,}036x^2 + 30{,}27x - 10{,}233$	$R^2 = 0{,}9976$
60	$y = -0{,}0022x^6 + 0{,}0764x^5 - 1{,}0209x^4 + 6{,}6545x^3 - 21{,}675x^2 + 33{,}85x - 12{,}933$	$R^2 = 0{,}9973$

3.1.4. The effect of inhibitors on the rate of reaction of hydrochloric acid in contact with reservoir rock

In order to ensure the deepest cracks (crevices), it is necessary to carry out treatments of the used hydrochloric acid, with the aim of delaying the reaction speed of the acid (in order to remain in contact with the rock collecting the hydrochloric acid as much as possible).

The techniques used to ensure a higher response time are as follows:

a. Decrease in the temperature of the acid solution,

b. The use of additives (inhibitors).

In the laboratory I used various concentrations of hydrochloric acid on a calcareous rock and also lowered the solution temperature from 20ºC to 0ºC and -20ºC (Table 10).

Table 10

Numerical relations for determining the percentage decrease in the concentration of the HCl solution (in contact with the calcareous rock) as a function of the time elapsed since the beginning of the experiment

Temperature of hydrochloric acid solution, ^{0}C	The polynomial equation (y represents the decrease in HCl concentration, % compared to the initial concentration and x represents the reaction time between HCl and rock, min),	R^2
-20	$y = -0{,}0005x^4 + 0{,}0304x^3 - 0{,}5445x^2 + 4{,}6781x - 1{,}9186$	$R^2 = 1$
0	$y = -0{,}0004x^5 + 0{,}0296x^4 - 0{,}6711x^3 + 5{,}9069x^2 - 12{,}333x + 17{,}168$	$R^2 = 1$
+20	$y = -0{,}0005x^4 + 0{,}0304x^3 - 0{,}5445x^2 + 4{,}6781x - 1{,}9186$	$R^2 = 1$

I also introduced acetic acid, benzene and glycerol into a solution of HCl (10% concentration) as an inhibitor of the reaction rate (Table 11).

It is observed that in the case of limestones, the use of additives (inhibitors) of the reaction leads to the extension of the contact time which increases with the addition of acetic acid and decreases if we add alcohol (glycerol).

We also built a numerical model based on logarithmic equations of the type:

$$y = a\,ln(x) - b \tag{5}$$

Where a and b are reaction constants and depend on the characteristics of the additive used and its concentration.

The decrease in the temperature of the hydrochloric acid solution brings us a rapid decrease in the concentration of the solution compared to the initial one (a process that is difficult to achieve in site conditions).

The equations of variation of the decrease in HCl concentration, % (compared to the initial concentration) as a function of the reaction time between HCl and rock, are of polynomial form, of order 4 or 5.

Table 11

Numerical relations for determining the percentage decrease in the concentration of the HCl solution (in contact with the calcareous rock) as a function of the time elapsed since the beginning of the experiment

Type of acid solution, ^{0}C	The polynomial equation (y represents the decrease in HCl concentration, % compared to the initial concentration and x represents the reaction time between HCl and rock, min),	R^2
Acid solution 10 % HCl	y = 27,567ln(x) - 0,5119	R^2 = 0,9434
Acid solution 10 % HCl and 0,5 % alcool (glycerol)	y = 29,584ln(x) - 6,9194	R^2 = 0,9579
Acid solution 10 % and 2 % acid acetic	y = 27,71ln(x) - 6,3885	R^2 = 0,9548
Acid solution 10 % and 3 % acid acetic	y = 23,995ln(x) - 6,1036	R^2 = 0,9235
Acid solution 10 % and 1 % benzene	y = 26,376ln(x) - 5,7283	R^2 = 0,8974

3.1.5. The effect of anhydrite on the acidification of calcareous rocks

The dissolution process of calcium carbonate ($CaCO_3$) is affected by anhydrite inclusions (calcium sulfate $CaSO_4$).

This phenomenon is due to the precipitation of gypsum sediments ($CaSO_4 \cdot H_2O$) as a result of the interaction between hydrochloric acid and calcium carbonate [4].

$$2HCl+CaCO_3=CaCl_2+H_2O+CO_2 \quad (5)$$

Normally, after the interaction between the rock and the acid, the calcium chloride must remain in suspension in the water and then be cleaned.

But when the limestone is contaminated with ahydrite, there is a reduction in the dissolution process, the complete neutralization time being longer by 1 ½ hours if we have a contamination of 12% and 4 hours if the contamination is 34%.

$$2HCl+CaSO_4+CaCO_3=CaCl_2+ (CaSO_4 \cdot H_2O)+CO_2 \quad (6)$$

The experiments that were carried out to determine the simultaneous reaction between HCl solutions of different concentrations, $CaCO_3$ and $CaSO_4$ from the rock showed us the following aspects:

- When the rock can contain 33% or 50% anhydrite, gypsum is deposited ($CaSO_4 \cdot H_2O$) in the amount of 0.5 or 0.8 kg $CaSO_4/m^3$ of acid solution,
- In the case of rocks containing a maximum of 20% CaSO4, the maximum concentration of gypsum becomes 0.075 per 100 ml of solution and the saturation concentration (which is 0.07 g per 100 ml) is not exceeded.
- Reducing the acid solution to 50% will lead to simultaneous dissolution of $CaCO_3$ and $CaSO_4$.

In order to create a numerical model regarding the influence of the mineralogical composition on the reaction speed of the acid solution for some rocks (analyses performed at 20 ºC), we processed the data obtained on the rocks in table 12.

Table 12

The mineralogical composition of the rocks treated with hydrochloric acid solution in order to establish the decrease in its concentration depending on the time of

Sample	Content of $CaCO_3$	Content of $CaMg(CO_3)_2$	Content of $CaSO_4$	Total Carbonates %	Porosity,
					%
1	68,48	31,08	0,44	100	14,6
2	73,45	18,91	5,65	98,01	8,12
3	89,65	7,15	2,39	99,19	16,54
4	98,62	0	1,38	100	0,24
5	53,79	33,02	13,1	99,91	1,36
6	35,09	57,71	6,2	99	11,45
7	11,3	79,86	7,82	98,98	17,02
8	43,32	41,28	13,45	98,05	4,28
9	3,52	63,78	31,25	98,55	3
10	8,31	53,73	32,65	94,69	4,6
11	98,7	0,55	-	99,25	1
12	13,62	81,77	2,58	97,97	8
13	11,55	87,33	0,87	99,75	8

As a result of the penetration of hydrochloric acid into rocks with a calcium carbonate content of less than 20%, gypsum precipitation does not occur and therefore the blocking of the strata.

At 2.5 mm channels and pressures of 10-60 kgf/cm^2 precipitation also does not occur.

Also, the SO_3 content must not exceed 10% to avoid gypsum deposits, but if this is found, then the hydrochloric acid solution must have a maximum concentration of 10% (Table 13).

Table 13

Numerical relations for determining the percentage decrease in the concentration of the HCl solution (in contact with the calcareous rock) as a function of the time elapsed since the beginning of the experiment

Sample	The polynomial equation (y represents the decrease in HCl concentration, % compared to the initial concentration and x represents the reaction time between HCl and rock, min),	R^2
1	$y = 0,0044x^3 - 0,4398x^2 + 12,236x + 8,2727$	1
2	$y = 0,0083x^3 - 0,8479x^2 + 24,065x - 88,164$	1
3	$y = 0,0031x^3 - 0,335x^2 + 10,477x - 1,4$	1
4	$y = 0,0031x^3 - 0,335x^2 + 10,477x - 1,4$	1
5	$y = 0,0008x^3 - 0,1144x^2 + 5,7818x - 6,1455$	1
6	$y = 0,0002x^3 - 0,0646x^2 + 4,7282x - 6,0545$	1
7	$y = -0,0006x^3 + 0,0234x^2 + 1,9482x + 11,745$	1
8	$y = 1E\text{-}06x^4 - 0,0004x^3 + 0,0362x^2 + 0,5792x - 2,5321$	1
9	$y = 1E\text{-}06x^4 - 0,0004x^3 + 0,0362x^2 + 0,5792x - 2,5321$	1
10	$y = 8E\text{-}05x^3 - 0,0068x^2 + 1,0185x - 1,5418$	1
11	$y = 0,0021x^3 - 0,2315x^2 + 7,9094x + 7,9818$	1
12	$y = -4E\text{-}05x^4 + 0,0095x^3 - 0,6502x^2 + 16,54x - 59,432$	1

3.2. Acidification of productive layers consisting of sandstones and non-calcareous sands

For the acidification of these types of reservoir rocks, hydrochloric acid has no or little effect.

That is precisely why the use of hydrofluoric acid is foreseen, which will react with the petrographic components after the following chemical reactions [3]:

$$HF + SiO_2 = SiF_4 + H_2O \quad (7)$$

$$HF + CaCO_3 = CaF_2 + CO_2 + H_2O \quad (8)$$

The equations above show us that the reaction with silicon dioxide leads to the formation of silicon fluoride which will be released into the deposit (as a gas) as well as calcium fluoride (which will deposit).

Reactions with aluminum silicate rocks will occur after the chemical reaction [3]:

$$CaAl_2Si_2O_8+16HF = CaF_2 + 2AlF_3 + 2SiF_3 + H_2O \quad (9)$$

4. **Conclusions**

The analyses carried out in this paper confirm the following:

a. The mixture of HCl and HF when it penetrates the productive rock, their reactivity takes place with the clay elements, carbonates, and quartz that constitute the rock of the layer and the drilling fluids, cement, and salts existing in the contact zone and ensures the enlargement of the fluid transfer channels oil tankers,

b. The solubility of clays in a mixture in which HF is found in a proportion of 3% by volume is 2-3 times higher than their solubility in a fluid containing hydrochloric acid in the proportion of 15%,

c. Under the action of the mixture of HCl and HF, the clays dehydrate quickly, and they can be easily removed,

d. The quartz sand reacts with the acid mixture faster; the more dispersed it is,

e. For a mixture of 12% HF in a solution of HCl (with a concentration of 10%), the fraction of sand with grains of 0.250-0.176 mm dissolves in a proportion of 33%,

f. For a 24% carbonate content, the solubility of sandstones (immersed in a solution containing 10-15% HCl and 3% HF) after 24 hours was 44% compared to 28.8% for an HCl solution,

g. The dissolving power of the acid mixture increases proportionally with the HF content in the solution,

h. At atmospheric pressure, the reaction between the mixture of acids and rock has an increased reactivity in the first 2-4 hours and is completed after 14 hours,

i. Increasing the temperature of the acid solution from 20 ºC to 80 ºC leads in the first 2-4 hours to an increase in the solubility of the sandstones by 5-6%.

Natural gas is the cleanest and most economical fossil fuel. The physicochemical quality of the gases extracted from fossil deposits makes them very useful in industrial (chemical) processing, and they play an increasingly important role in the national and world economies.

Considering transition gas (transition energy), it proves that the 21st century will be the time of natural gas.

Most natural gas fields are characterized by low permeability and prone to water flooding (due to the need for rapid extraction due to competitive market prices).

That is precisely why, in many cases, the recovery factor is low. Given the increase in gas quantities from year to year, it is necessary to discover new deposits,

exploit the existing ones at higher rates of the recovery factor, and, above all, exploit the gas deposits stored in rocks with low permeability (clays and oil shales).

Therefore, improved gas recovery methods are vital to the national economy and society.

Enhanced gas recovery refers to industrial approaches, technologies, or processes that improve the gas recovery factor.

By primary gas recovery, we mean using extraction techniques based on the expansion of deposits (of their pressure).

By secondary (or enhanced) recovery, we mean the application of techniques to increase the final recovery factor, such as injecting chemicals (polymers), CO_2, water, etc.

In recent times, enhanced (tertiary) natural gas recovery technologies have gained momentum, among them mentioning [4]:

a. Horizontal directional drilling of extraction wells (drilling of a vertical well and from a certain depth horizontal drilling in several directions and of different lengths, in order to ensure more excellent contact between the productive formation and the extraction well),

b. Hydraulic Fracturing of low permeability layers. This process consists of the creation (under pressure) of communication channels (flow paths) of petroleum fluids by using a fracturing fluid (which is pumped into the geological formation at a pressure that facilitates the production of artificial cracks),

c. Hydraulic Fracturing in several stages (multiple Fracturing) consists of first fracturing the most distant productive formation and then simulating the productive layer along its entire length. Fracturing fluids can be water-based and mixed with alcohol, chemical agents, etc.

d. Pneumatic Fracturing consists of the injection of a gas jet (air, nitrogen, or specific gas mixtures) that can create cracks in the constituent rocks of the gas reservoir,

e. Fracturing is due to the use of explosives, which provide for the forming of rocks through propellants or explosive ammunition. This fissure-creation system consists of shooting the productive layer with bullets and, therefore, creating communication channels or using explosives to ensure the detonation and cracking of the reservoir rocks. It is a valuable method (water and chemicals are no longer used) but with a low yield, being feasible only over short distances,

f. Electric Fracturing is based on the thermal effect of electric current and, therefore, the deformation and cracking of rocks,

g. Cryogenic Fracturing is a little-used method, the cracks being made by injecting fluid with a low temperature and therefore, as a result of the contact with the rock, it will lead to the contraction of the contact surface and the production of cracks,

h. Cracking with liquefied carbon dioxide is the newest method proposed for use; this technique, also succeeded in storing this gas,

i. Mechanical cutting of rocks by a flexible cutting cable. This technique leads to rapid increases in productivity through the use of cables that can be routed between two productive wells,
j. Use of microorganisms to improve methanogenesis.

5. Data Availability

The data presented in this article is real and collected from the area of interest.

The data can be used by anyone in accordance with applicable international regulations. Data is available in the article and can be provided upon request.

6.Conflicts of Interest

No data or information is presented that could endanger companies or commercial or public companies. There are no conflicts regarding the exposed data. The data taken from the soil samples analyzed and presented in the article are part of oil fields abandoned and handed over to the public domain.

The authors did not benefit from public, private or other resources.

REFERENCES

[1] Lee, J. & Wattenbarger, R.A., *Gas Reservoir Engineering*; SPE Textbook Series Volume 5; USA 1996; ISBN 1-55563-073-1,

[2] McCain, W.D., *The properties of petroleum fluids*; PennWell Publishing Company; USA 1990; ISBN 0-87814-335-1,

[3] Zeinab A., Pozo A.O., Claudia Maria Brezeanu M.C., Chis T. (2023) *Novel acid soluble abrasive material for abrasive jet perforation through coiled tubing and ts-tool for carbonate gas well – Yard test*, Romanian Journal of Petroleum & Gas Technology VOL. IV (LXXV) • No. 2/2023, pp. 97-108, DOI: 10.51865/JPGT.2023.02.10, http://jpgt.upg-ploiesti.ro/wp-content/uploads/2023/09/10_RJPGT_2023-timur-chis-4-final.pdf,

[4] Zeinab A., Pozo Al. O., Chis T., Gutiérrez J. U., (2023), *Hydraulic Coiled Tubing Tractor Technology Extends the Accessibility of Coiled Tubing in Horizontal Wells, allowing better well intervention – Case study*, Engineering and Technology Journal, http://www.everant.org/index.php/etj/issue/view/169,

LABORATORY ANALYSIS OF OILFIELD WATER EXTRACTION FROM EMULSIONS

Reem Sabah MOHAMMED[1], Timur CHIȘ[2*], Dumitru CHISĂLIȚĂ[3]

[1]Ph.D. School, Oil and Gas University, Ploiești, Romania,

[2]Oil and Gas Engineering Department, Oil and Gas University, Ploiești, Romania,

[3]Transilvania University, Brasov, Romania

Abstract

The water-connected dangers in refining, oil exploration, and dissemination are deliberated. Subsequently, the oil produces deliver completed 90% of transportation liveliness in practically all republics; oil source interjects might have thoughtful belongings, not individual on movement, but correspondingly on the food distribution and manufacture, medical care, heating, manufacturing, national security, and other energetic occupations of the contemporary societies. Once the oil is discovered in uncommon water areas, the water possessions develop harassed. Off-shore oil examination generates risks for the maritime lifecycle, while oil dissemination and transportation determination produce cumulative risk for the ecosystem in case of accidents or leakages. Petroleum manufacturing commonly categorizes crude oil by its geographic position, thickness, and sulfur content. A heavy crude oil has a high density, and a light crude oil has a stumpy thickness. An oil well produces principally crude oil through some softened natural gas. Since the compression is subordinate at the surface to underground, selected gas will originate out of the solution and will be either burned or healthier. Crude oil is also found in semi-solid form mixed with sand and water, as in the Athabasca oil sands in Canada, anywhere it is frequently mentioned as crude bitumen. Bitumen is a black, sticky, tar-like procedure of crude oil that is so heavy and thick that it must be impassioned or thinned before its determined flow. In the study on water source quality, the particle size suspended solid concentrations and oil content in the water source are mainly considered.

Key words: water, oilfield, emulsion

1. Introduction

Worldwide energy demand is gradually increasing due to anthropogenic activities.

As per the Key World Energy Statistics (2022), crude oil production in developing countries will increase from 40 mb/day (2023) to 50 mb/day in 2050.

In the most accurate context, the increase in investments in the oil industry is foreseen to be 0.9 trillion USD.

* Corresponding author: timur.chis@gmail.com

Natural and fossil fuel sources gradually increased to 31% of oil, 29% of coal, 21% of natural gases, 10% of waste and biofuel, 54% nuclear, 2% hydro, and other essential energy sources like solar, wind, geothermal, and heat until 2013 (https://www.energysector.in/world-energy/key-world-energy-statistics) (figure 1).

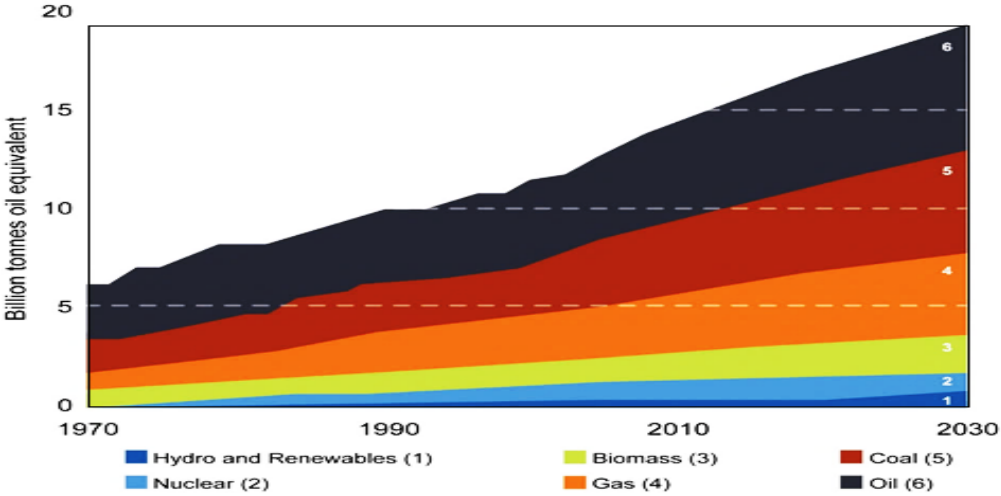

Fig.1 World Energy Consumption by fuel type (IEA: World Energy Outlook, 2006).

Petroleum energy demand is increasing gradually due to transportation development and anthropogenic activities; therefore, gas and Oil fields are more important for the country's economic and political effectiveness [1].

The water flooding method is widely used for secondary oil recoveries after the primary oil recoveries from reservoirs [2].

Water flooding is where water is injected into the oil reservoirs through water pumping.

After that, the water is forced out of the Oil into the other reservoir sections known as producers.

Therefore, the produced fluids are progressively increased due to water injection. In the research result, Craig (1971) observed that the admiration of water injection is principally outstanding due to its displacement efficiency, mobility, availability, and ease of injection [3].

In addition to the water flooding processes, it becomes inefficient to endure these procedures since the cost of eliminating and disposing water surpasses the net income produced by oil production [4].

Oil recoveries are the primary concern to engineers, as they are used to recover secondary Oil from different oil reserves that are flooded by water [5].

The main concern about the process is the high rate of oil recoveries using low water production.

The water drive capacity maintains the oil withdrawal rate in addition to the level of the reservoir pressure.

The Callaway method was used for water flooding design to evaluate the maximum level of recoverable reserves (figure 2)

$$\text{Npwf} = V_p, \frac{1 - S_{wc}}{\text{B}_{oi}} . \{1 - R_p - \frac{\text{B}_{oi}}{\text{B}_{of}}, (1 - E_{vo} . E_D)\} \qquad \text{(Eq.1)}$$

Where, $V_p$representing the volume of the flooding reservoir, B_{oi} indicates the original formation of the volume factor, RB/STB, B_{of} is representing the FV factor during the water flooding, S_{wc} is denoted that the saturation or fraction of the connate water, $R_p$is denoted that the fraction of the Original Oil in Place (OOIP) of Primary recovery efficiency, E_{vo} indicates the Overall volumetric sweep efficiency, fraction of reservoir volume, E_D is representing the maximum unit of the displacement efficiency, fraction and the Npwf indicates the water flooding reserves, STB.

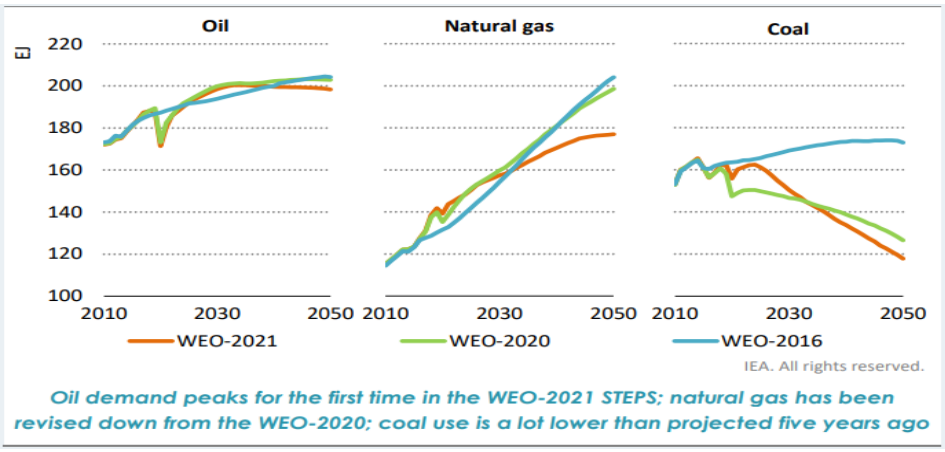

Fig.2 Oil, natural gas and coal demand in the Stated Policies Scenario in World Energy Outlook 2021, 2020 and 2016. (Source: World Energy outlook, 2021, Available website: https://iea.blob.core.windows.net/assets/4ed140c1-c3f3-4fd9-acae-789a4e14a23c/WorldEnergyOutlook2021.pdf)

The principal repossession approach expends the rock liquid, regular flow mechanisms, and gas expansion plus solution gas determination permission around 80% or more of the original oil in place (OOIP); subsequently, the pressure in the reservoir has been exhausted.

A massive expanse of the hydrocarbon remains unrecovered in the exhausted reservoirs worldwide.

Billions of barrels of supplementary oil might have been improved, and water flooding was concluded to be the most significant technique for enlightening recovery after oil reservoirs.

Water flooding frequently occurs; subsequently, reservoir (pressure) diminution consumes.

It is recurrent that the gas cap and saturation procedures in an explanation gas determination reservoir are outstanding in this pressure depletion.

The cumulative reservoir pressure from the injected water will initially force the free gas to dissolve into the oil.

The oil production frequency of the water injection will develop ostensibly after the water injection has attained fill-up of the gas space [6].

The thoroughgoing oil production proportion as the reservoir is re-pressurized is contingent upon the reservoir physiognomies and the injection rate. Sustained water injection determination eventually leads to a “breakthrough” of the injected water at the production wells [6].

2. Materials and Methods

The water-connected dangers in refining, oil exploration, and dissemination are deliberated.

Subsequently, oil producers deliver 90% of transportation lifelines in practically all republics.

Oil source interjects might have thoughtful belongings, not individual on movement but correspondingly on food distribution and manufacture, medical care, heating, manufacturing, national security, and other energetic occupations of contemporary societies.

Once the oil is discovered in uncommon water areas, the water possessions develop harassed.

Off-shore oil examination generates risks for the maritime lifecycle, while oil dissemination and transportation determination produce cumulative risk for the ecosystem in case of accidents or leakages.

Petroleum manufacturing commonly categorizes crude oil by its geographic location, thickness, and sulfur content.

A heavy crude oil has a high density, and a light crude oil has a stumpy thickness.

An oil well produces principally crude oil through some softened natural gas.

Since compression is subordinate at the surface rather than underground, some of the gas will originate out of the solution and be either burned or healthier.

Crude oil is also found in semi-solid form mixed with sand and water, as in the Athabasca oil sands in Canada, and anywhere else, it is frequently referred to as crude bitumen.

Bitumen is a black, sticky, tar-like substance made from crude oil. It is so heavy and thick that it must be ignited or thinned before it can flow.

In the study on water source quality, the particle size suspended solid concentrations and oil content in the water source are mainly considered.

The Natural gas hydrate in the underwater mainland permafrost and boundary coatings have been documented as an eccentric natural gas reserve.

In these approaches to hydrate sediment gas production, like thermal stimulation, depressurization, and a combination of chemical inhibitor stimulation of these methods, percolation possessions regulate fluid flow in hydrate residues through chemical transfer and heat.

The importance of permeability throughout gas production has led to widespread examinations of relative and absolute permeability in hydrate sediments.

Certain industrialized numerical prototypicals are used to examine the belongings of various arguments, like absolute, permeability reduction index, relative permeability, and porosity, throughout the gas production from porous media comprising hydrates.

The datasets showed that diminishing the grain size and permeability decreases the proponent and increases the hydrate dissociation rate.

This recommended that the permeability reduction index and comparative permeability model, created on the changed hydrate formation types in the porous media, were of great prominence for approximating gas production.

Fig 3 indicates that a big enough particle size of suspended solid in injected water might cause rock permeability loss.

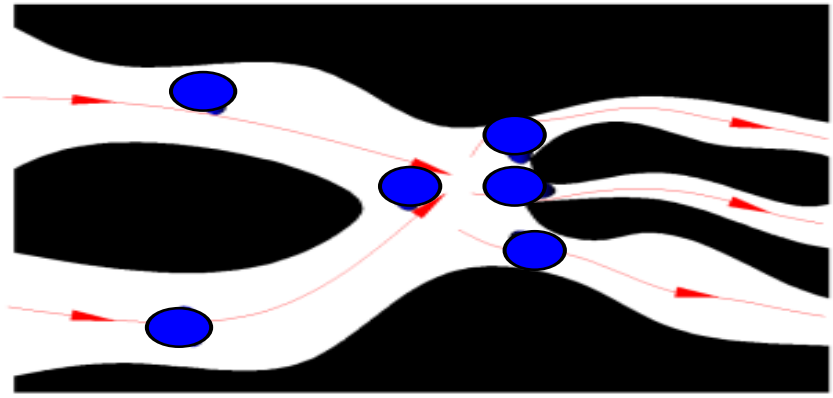

Fig 3. Sketch map for particle size effect on rock permeability.

Fig 4 and Fig 5 show the test results of 10 core samples (reelevates to the Oil Production Reserves) where 5 core samples were with particle size from 0.5μm to 14.5μm and other 5 core samples were with particle size from 0.5μm to 3.1μm.

Both types of test years are added where five different types of core IDs were observed and Permeability (mD) and Porosity (%).

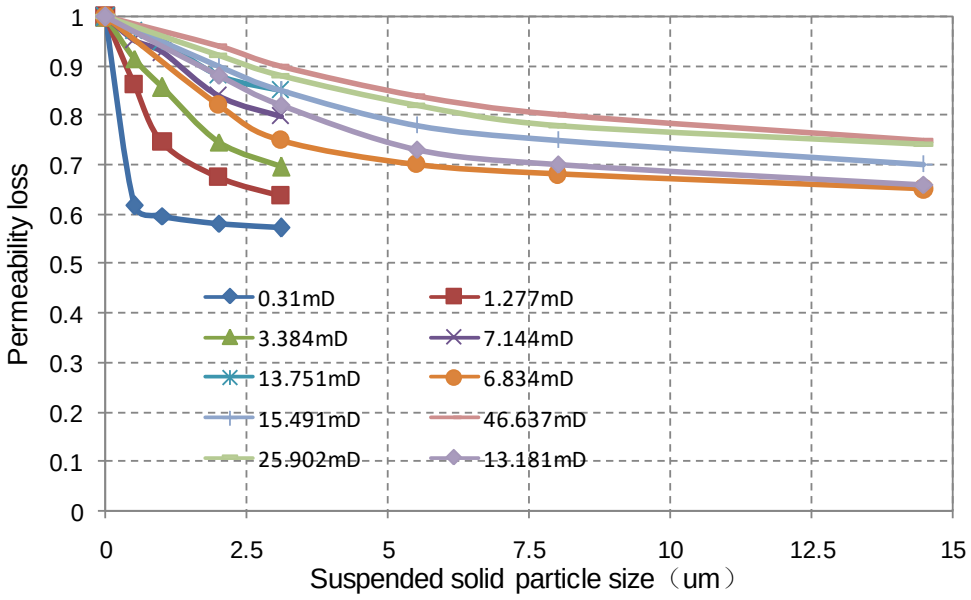

Fig 4. Core permeability loss vs. suspended particle sizes.

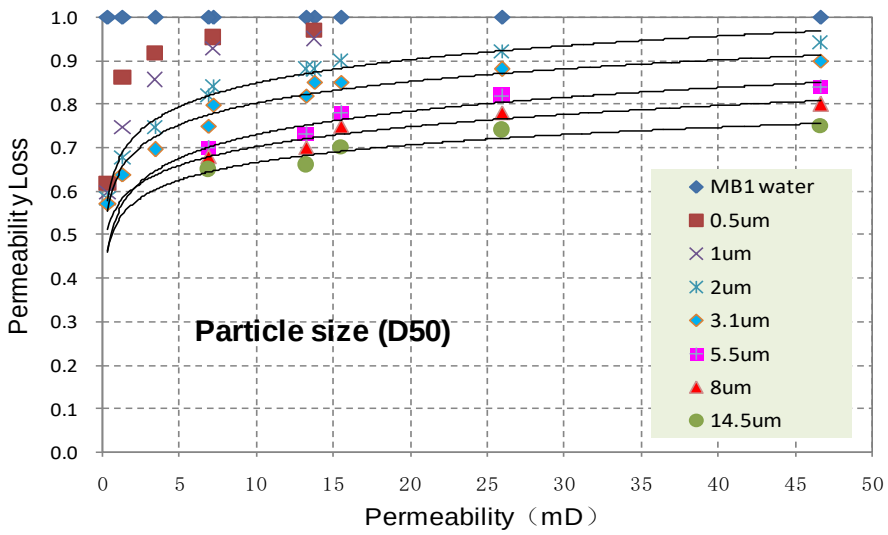

Fig 5. Permeability loss vs. core permeability for different particle sizes.

Generally, the smaller particle size of suspended solid in water could be acceptable for rock reservoir with lower permeability.

For example, D50 ≤5.5μm could be acceptable for k≤10md reservoir, if permeability loss ≤30%.

Fig 6 is a sketch map showing different particle size and different total suspended solid in injected water.

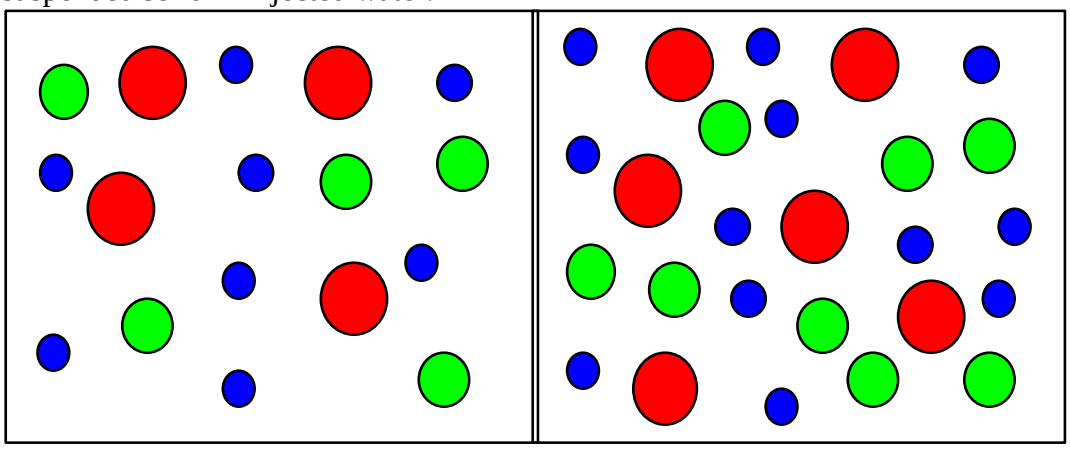

Fig 6. Sketch for particle size and total suspended solid in water

Fig 7 shows 10 core sample test results of different total suspended solid (TSS) and 5 core samples were with TSS from 0 to 30mg/l and the other 5 samples were with TSS from 0 to 10mg/l.

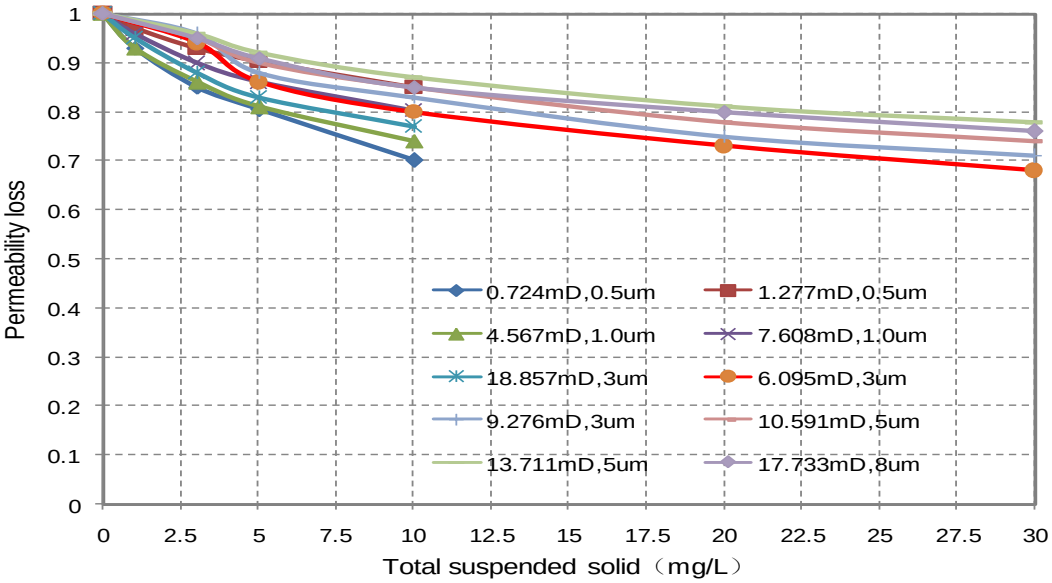

Fig 7. Permeability loss vs. total suspended solid for different permeability.

Generally, the lower total suspended solid in the injection water could be acceptable for rock reservoir with lower permeability.

For example, TSS ≤30mg/l could be acceptable for k≤10md reservoir, if particle size around (D50) 5.5μm and the reservoir permeability loss ≤30%.

Fig 8 and Fig 9 show the test results of different oil contents of 9 core samples and 5 core samples were with oil content from 0 to 50mg/l and the other 4 samples were with oil content from 0 to 20mg/l.

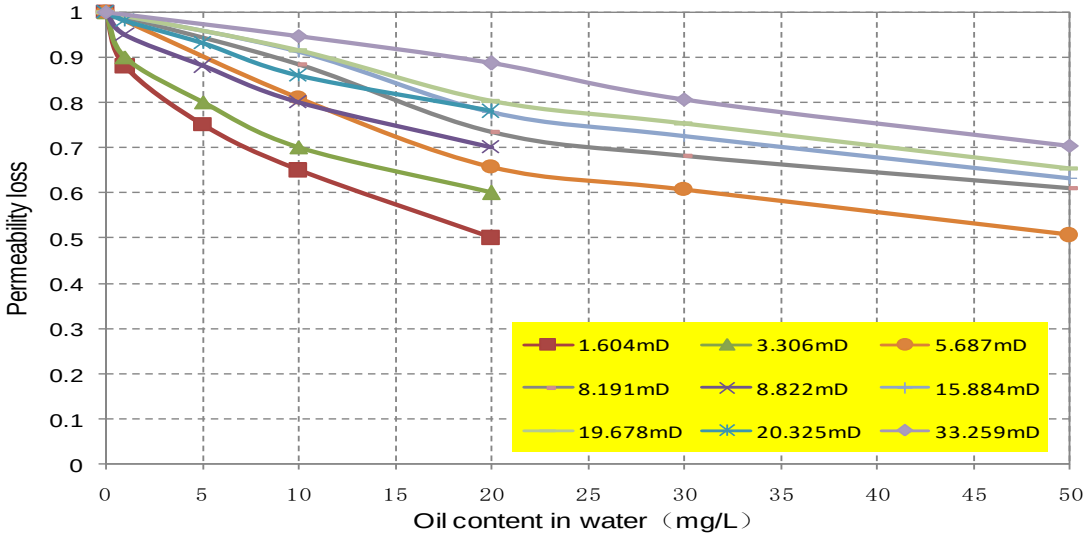

Fig 8. Core permeability loss vs. oil content in water.

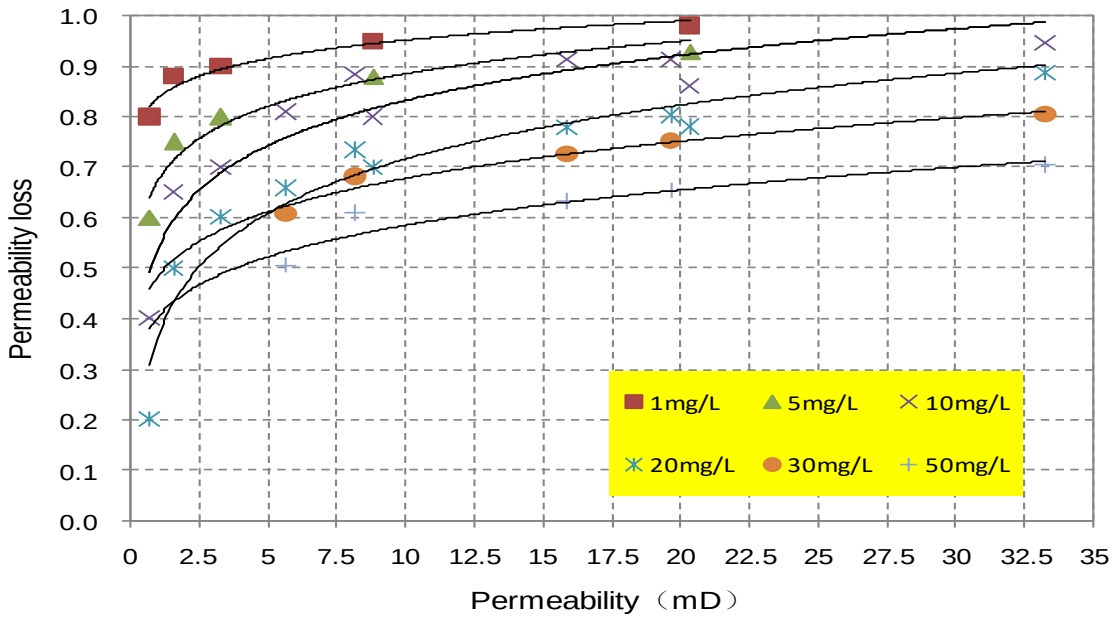

Fig. 9. Core permeability loss vs. permeability for different oil content.

Generally, the lower oil content in the injection water could be acceptable for rock reservoir with lower permeability.

For example, oil content ≤20mg/l could be acceptable for k≤10md reservoir, if permeability loss ≤30%.

Some parameters were observed for this investigation where Salinity, Ca_{2+}, SO_4^{2-}, Mg^{2+} those parameters were investigated with none different aspect like EDH, Pilot water, EDS, Misson water and Fresh.

Fig 10 shows their salinity and Ca_{2+}, SO_4^{2-}, Mg^{2+} contents.

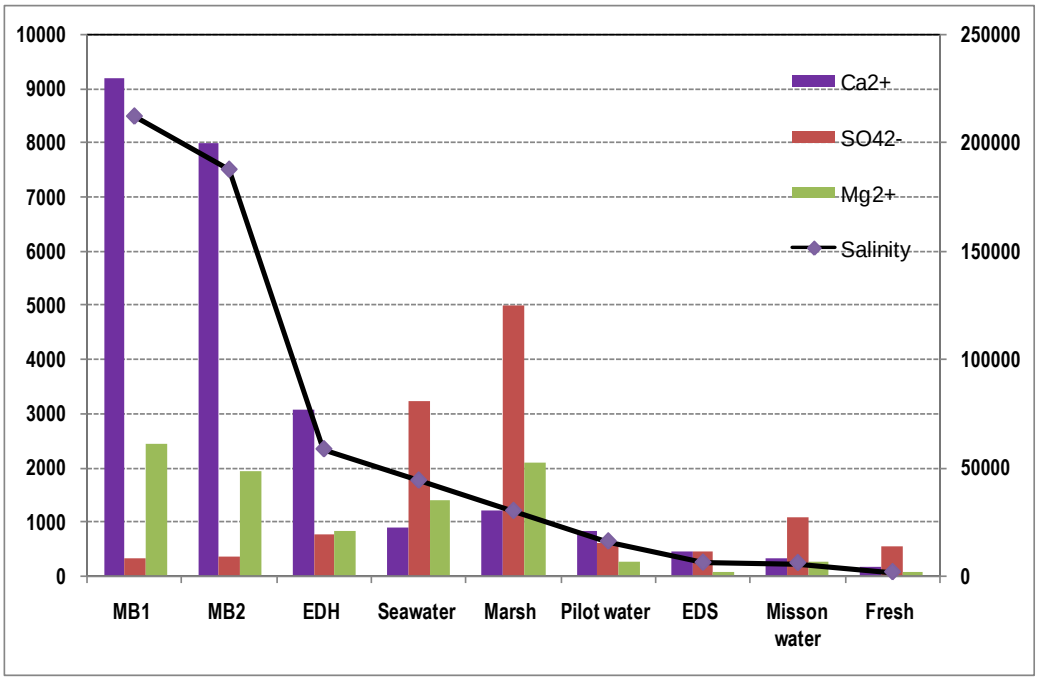

Fig 10. Salinity, Ca_{2+}, SO_4^{2-}, Mg^{2+} contents in the water.

For Mishrif reservoir water-flooding, preliminary conclusion is that in terms of low salinity water, Ca^{2+}, SO_4^{2-}, Mg^{2+} contents and reservoir scaling, 7 kinds of potential water source are acceptable.

But about 7 kinds of water source, some information such as particle size distributions and TSS of EDH, EDS, seawater, marsh, pilot water and treated fresh water, also TSS of Misson plant water etc. are unknown and needed to be measured.

4. **Conclusions**

1) Mishrif rock with weak water, weak salt, weak velocity, weak stress sensitivities and medium-strong acid sensitivity. The main reason is that the main composition of reservoir rock is calcite (97%), a small amount of dolomite (2.4%) and clay mineral (less than3%).

2) Mishrif rock wett-ability is mainly oil-wet and seems has a tendency of oil-wet, medium-wet and water-wet from the upper MB1-2 or MB2 to the lower MC1-4.
3) Generally, a reservoir with higher permeability and bigger porosity has higher movable fluid saturation (Smf). For Mishrif reservoir rock, Smf is 55～75% for K ≤10md and 70～90% for K＞10md.
4) Pilot water-flooding efficiency is around 65% and Sw at intersection point is around 0.52. Compared with formation water-flooding, pilot water-flood has 4% increase in E_D and 0.3 higher in Sw at intersection point. And other potential water sources efficiencies are over 60%.
5) The water-flooding characteristics shows that the ultimate oil recovery is about 65%, around 10% recovery during free-water period, 15% recovery during water cut from 20% to 80% and 30% recovery during water cut from 80% to 98%.
6) Compared to formation water, lower salinity pilot water could improve rock water phase permeability, decrease displacing pressure, decrease oil/brine interfacial tension, alter rock wett-ability from oil-wet to water-wet and dissolve some minerals in water and increase oil recovery.
7) Small particle size of suspended solid in water is acceptable in low permeability rock. For example, particle size D50 ≤5.5μm is acceptable in order to reservoir permeability loss ≤30% for K≤10md reservoir.
8) Low TSS in water is acceptable in low permeability rock. For example, TSS ≤30mg/l with D50 about 5.5μm particle size is acceptable in order to permeability loss ≈30% for K≤10md reservoir.
9) Low oil content in water is acceptable in low permeability rock, for example, oil content ≤20mg/l is acceptable in order to the permeability loss ≈30% for K≤10md reservoir.
10) In terms of low salinity, Ca^{2+}, SO_4^{2-}, Mg^{2+} contents in water and formation scaling, 7 kinds of potential water source are acceptable and in terms of particle size of suspended solid in water, Misson plant water is also acceptable for Mishrif reservoir water-flooding.
11) Carry out water-flooding experiments using about 0.2m long core and/or whole diameter core sample.
12) Analyze ions content, TSS and particle size distributions of EDS, EDH, treated fresh water, Marsh, separated water and Middle Kirkuk formation water samples.
13) Study the effects on water-flood efficiency for different ions concentration such as Ca^{2+}, SO_4^{2-} in water to optimize the injection water quality.
14) Continue to study the potential water compatibilities with reservoir rock, including Middle Kirkuk formation water.
15) Continue to study the characteristics of water-flooding at different injection pressure, injection velocity and injection PV etc.

5. Data Availability

The data presented in this article are real and collected from the area of interest.

The data can be used by anyone in accordance with applicable international regulations. Data is available in the article and can be provided upon request.

6. Conflicts of Interest

No data or information is presented that could endanger companies or commercial or public companies. There are no conflicts regarding the exposed data. The data taken from the soil samples analyzed and presented in the article are part of oil fields abandoned and handed over to the public domain.

The authors did not benefit from public, private or other resources.

REFERENCES

[1] Crawford, H.R.; Neill, G.H.; Bucy, B.J.; Crawford, P.B. Carbon Dioxide - A Multipurpose Additive for Effective Well Stimulation. *Journal of Petroleum Technology* **1963**, *15*, 237–242, doi:10.2118/571-pa.

[2] CRAIG, F.C. The Reservoir Engineering Aspects of Waterflooding. *Monograph Series, Society of Petroleum Engineers of AIME* **1971**.

[3] Stegemeir, G. Review of: "Larry W. Lake, Enhanced Oil Recovery" (Englewood Cliffs, NJ: Prentice Hall, 1989), 550 Pp., $64.00. *Energy Sources* **1990**, *12*, 97, doi:10.1080/00908319008960187.

[4] Ayoub, M.A.; Shabib-Asl, A.; AbdellahiZein, A.M.; Elraies, K.A.; Bin MohdSaaid, I. Recovery Optimization of an Oil Reservoir by Water Flooding under Different Scenarios; a Simulation Approach. *Research Journal of Applied Sciences, Engineering and Technology* **2015**, *10*, 357–372, doi:10.19026/rjaset.10.2499.

[5] Thakur, G.C. The Role of Reservoir Management in Carbonate Waterfloods. *All Days* 1998.

[6] Hubbert, M.K. Physical Principles of Oil Production 1950.

EFFECT OF TEMPERATURE AND EMULSIFIER DOSAGE ON WATER SEPARATION FROM CRUDE OIL EMULSION

David I. NECULA[1], Nicolae G. PANAINTE[1], Ancaelena E. STERPU[1*]

[1]OVIDIUS University of Constanţa

Abstract:
Crude oil emulsions are formed during the extraction process, especially due to the violent mixing of crude oil with water. Emulsions formed in this way can create problems in refineries, such as corrosion of processing or transport equipment.
Demulsification is a method of separating emulsions from water in crude oil into the constituent phases and which can be achieved by mechanical, thermal, electrical or chemical methods (using demulsifiers). Thermal and chemical demulsification methods are often used together for a better efficiency of water separation from crude oil emulsion because the demulsifier under the increasing temperature, accelerates the emulsion breaking process. Demulsifiers displace the natural stabilizers present in the interfacial film around the dispersed water droplets in the emulsion.
In this work, three different crude oil emulsions were prepared with different brine concentration in crude oil as follow: 10%, 15% and 20% (v/v). Of these three emulsions, only the 10% sample was selected for the experiment due to its high stability. Also, the separation time and the percentage of water decanted from different crude oil emulsions was determined at different temperatures (30, 40, 50 and 60ºC) and for different concentrations of demulsifier in emulsion (1%, 2%, 3%, 4% and 5%). The demulsifier selected for this work is a commercial type used in industrial applications, consisting of a mixture of C_9 aromatics hydrocarbons. The bottle test method was used to measure the water separation from crude oil emulsions. Also, a Bresser 5201000 LCD Digital Microscope, with 40x magnification level, was used to observe the water droplets distribution in crude oil emulsion. The results show that the efficiency of water separation from water-in-oil emulsions increases with increasing temperature and demulsifier concentration. Consequently, for a faster demulsification rate, a higher temperature is recommended, but not exceeding 60°C, as above this value there is a risk of losing the lighter fractions of crude oil through vaporization.

Key words: Crude oil, demulsification, emulsion, demulsifier, bottle test.

1. Introduction

Emulsions are heterogeneous systems that are formed from an immiscible liquid in the form of droplets called the dispersed phase, which is dispersed in another liquid called the continuous phase [1]. Crude oil emulsions are divided into three categories: oil-in-water (W/O) type, also called hydrophobic emulsions, water-in-oil (O/W) type, also known as hydrophilic emulsions, and multiple emulsions, which are water-oil-water type (W/O/W). This third category consists in fine water droplets dispersed in larger oil droplets, which are also dispersed in an aqueous continuous phase [2-4]. Crude oil emulsion are usually the result of drilling and transportation of oil, in the presence of accompanied water [5, 6].

*Corresponding author: email adrress: asterpu@univ-ovidius.ro

Under the oil processing conditions, a significant portion of this water can disperse in the form of fine droplets in the oil phase.

Crude oil is a complex mixture of hydrocarbons such as alkanes, naphthenes, aromatic compounds, as well as phenols, carboxylic acids, sulfur compounds, nitrogen compounds, and metals. Additionally, besides the hydrocarbons mentioned earlier, crude oil also contains heavy fractions with a high content of heavy compounds like resins and asphaltenes. The formation of crude oil emulsions is largely due to the presence of resins and asphaltenes, which can build a rigid film at the oil/water interface, acting as natural emulsifiers and providing high stability to the emulsion by preventing the water droplets coalescence. [7].

Crude oil emulsions pose significant challenges to the efficient production, transportation, and storage of petroleum products. These emulsions not only reduce the operational efficiency of equipment such as pumps, heat exchangers, and heaters but also contribute to the corrosion of pipelines. Furthermore, the physical properties of crude oil, including density, viscosity, and volume of spilled materials, undergo variations due to the presence of these emulsions. As a consequence of these changes, solid sludge, primarily composed of heavy fractions like asphaltenes, can precipitate, further complicating the production and storage processes [8].

Emulsions, while thermodynamically unstable, exhibit kinetic stability, allowing them to persist over extended periods [9]. The demulsification process is a solution for separating the crude oil emulsions. It involves the separation of water from the oil phase, facilitated by demulsifiers that disrupt the interfacial surface of water droplets, promoting their coalescence and subsequent removal through a settling process. The efficacy of the demulsification process is gauged by the rate of emulsion separation and the percentage of water that can be separated post-demulsification [10].

There are various methods for separating water from crude oil emulsions, such as coagulation [11], air flotation [12], ultracentrifugation [13], membrane filtration [14], and floculation [15]. Different demulsification methods, including physical, chemical, and biological approaches, have been employed to approach this issue. Desalters encompass thermal, electrical, and mechanical equipment, with examples such as knockout drums, two-phase separators, desalters, and settling tanks. Despite their effectiveness, the high operating and maintenance costs associated with physical methods often render them economically challenging. Consequently, chemical methods are frequently combined with physical techniques to expedite the separation process. On the other hand, biological methods leverage enzymes, bacteria, or fungi to achieve water-in-oil separation, representing a novel and promising technology in the industry [9].

From the available demulsifiers, chemical demulsifiers are predominantly favored by the industry due to their ability to achieve rapid and efficient separation of water-in-oil emulsions. Acting as surface-active agents, these chemical demulsifiers reduce interfacial tension, facilitating the flocculation and coalescence processes essential for effective demulsification [10, 16].

In this study, the influence of demulsifier dosage and temperature on the demulsification process of crude oil was investigated. The demulsifier used in the experimental part is an industrial one, consisting of a mixture of C9 aromatic hydrocarbons. The structure of the emulsions was analyzed microscopically using the Bresser 5201000 LCD digital microscope, with 40x magnification level.

2. Experimental

Materials and apparature:

For the experimental part of this work an Irakian EBCO type crude oil was provided from a petroleum refinery. Its main properties are presented in Table 1.

Table 1

The main properties of EBCO Irakian crude oil

Property	**Value**
API	32.52
Density, kg/m3	863.28
Water content [%(v/v)]	0.12
Sediment [%(w/w)]	0.01
Organic chlorides [mg/kg]	2.29
Anorganic chlorides - CLORA [mg/kg]	10.57
Anorganic chlorides - ASTM [mg/kg]	33.55
Pour point [°C]	-11.34
Total sulphur [%(w/w)]	1.35
Asphaltenes [%(w/w)]	1.41
Viscosity al 37.8 [°C] [cSt]	9.47
CCR [%(w/w)]	5.80
Total acidity [mgKOH/g]	0.22
Sulphur in VR [%(w/w)]	3.37
CCR in VR	19.15
Asphaltenes in RV [%(w/w)]	6.98
SR Diesel congelation [°C]	-12.25
Gases [%(w/w)]	0.76
Light naphtha [%(w/w)]	5.73
Heavy naphtha [%(w/w)]	9.42
SR naphtha [%(w/w)]	16.22
SR kerosene [%(w/w)]	11.69
SR gasoil [%(w/w)]	23.62
Light vacuum distilate [%(w/w)]	12.59
Heavy vacuum distilate [%(w/w)]	14.81

SR vacuum distilate [%(w/w)]	27.40
Vacuum residue [%(w/w)]	18.76
Loss [%(w/w)]	0.92
SR vacuum residue [%(w/w)]	19.68
White products yield [%(w/w)]	52.23
Black products yield [%(w/w)]	47.09

The demulsifier used in this work is a commercial one with confidential composition and it is also provided from a local petroleum refinery. This type of demulsifier is a complex organic oil-soluble desalting aid and it's a mixture of C9 aromatic hydrocarbons, with density = 921 kg/m^3 at 16°C and kinematic viscosity = 3 cSt at 38°C. It ca be fed either neat or diluted with aromatic solvent. Treatment rate varies depending on the system, crude types and monitoring on the desalter operation.

The morphological aspect of crude oil emulsion was examined by using a Bresser 5201000 LCD digital microscope, with 40x magnification level. This apparatus incorporates a digital camera and an LCD screen directly into the microscope, allowing users to view specimens without the need for an external monitor or computer.

Preparation of brine: The brine used to obtain the crude oil emulsion samples was prepared by dissolving an amount of sodium chloride calculated with Eq. (1) in distilled water [17]. The main scope of this method is to produce a stable crude oil emulsion with a known constant salinity. The salinity 20% was used as reference.

$$\text{Salinity, } Y = 8.3566X - 0.3582 \qquad (1)$$

where Y = salinity, %w
X = sodium chloride concentration, g/100ml

Preparation of crude oil emulsion: Three samples of crude oil emulsions were prepared by mixing the brine with crude oil to obtain different brine concentration in crude oil as follow: 10% (10 ml brine + 90 ml crude oil), 15% (15 ml brine + 85 ml crude oil and 20% (20 ml brine + 80 ml crude oil).

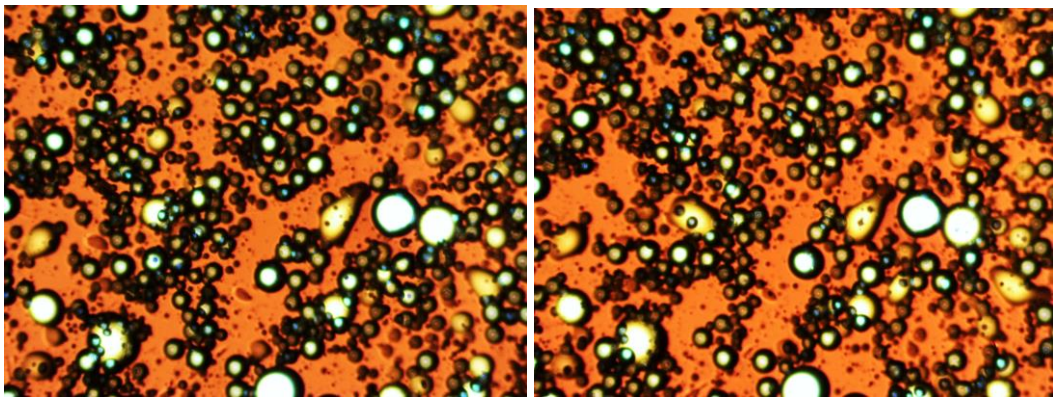

a)

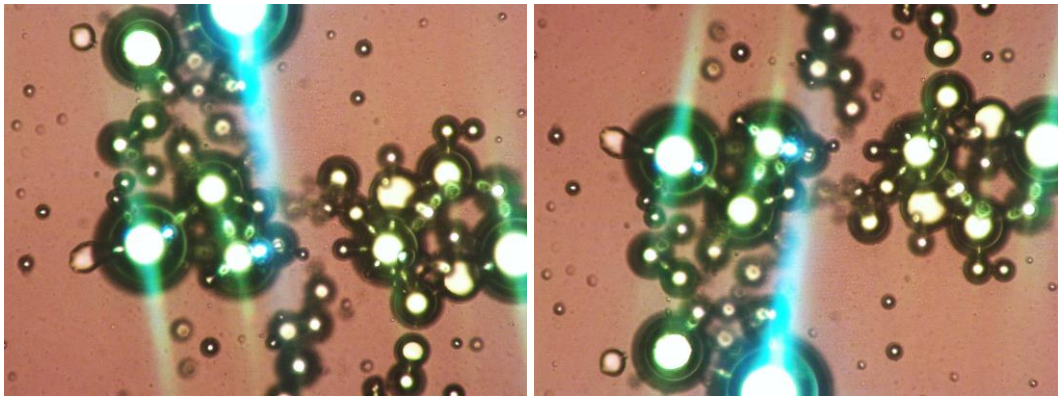

b)

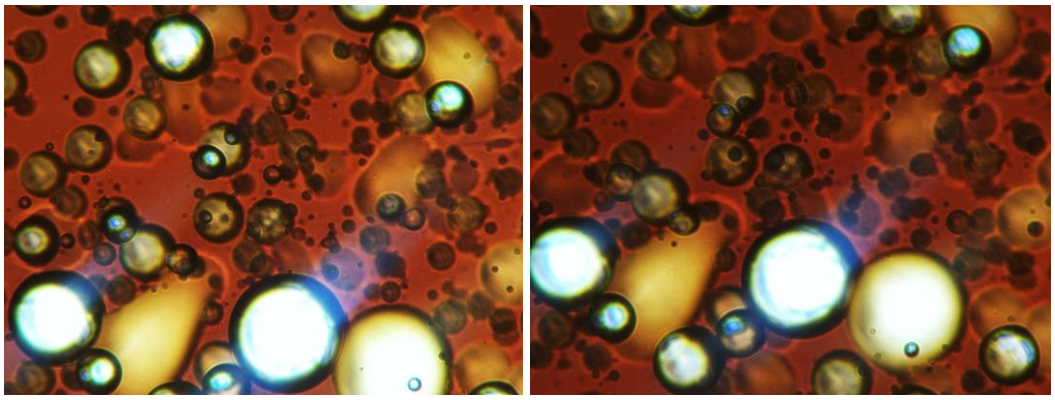

c)

Fig.1. Optical photographs of crude oil emulsion at different brine content: a) 10% brine, b) 15% brine and c) 20% brine

The emulsification process was carried out in a mixing vessel provided with a propeller type stirrer, at high rotation speed, for 1 hour, at 20°C. Then the obtained emulsion was left for 48 hours to ensure there is no separation of water before adding the demulsifier. The 20% water content sample was separated after almost 3 hours and the 15% water content sample was completely separated after almost 5 hours. As a result, the 10% water content sample was selected to be used in the demulsification process. Some optical photographs of crude oil emulsions with a) 10%, b) 15% and c) 20% water content are presented in Fig.1.

Demulsification procedure: In this study, a commercial demulsifier was selected to investigate its effectiveness in separating water from the crude oil emulsion under the effects of different parameters such as temperature and demulsifier dosage.

Temperature varied from 30°C, 40°C, 50°C to 60°C in order to examine the effect of temperature on the demulsification process. Demulsifier in the range of 1 - 5 ml was added to 100 ml of crude oil emulsion to study the performance of demulsifiers at different dosages (1, 2, 3, 4 and 5%).

Bottle test: Bottle test is conducted to measure the amount of water decanted from crude oil emulsion during demulsification process. The bottles were shaken 100 times manually to ensure the complete mixing between the crude oil emulsion and demulsifier. The bottles were then immersed in the water bath at a constant temperature for water decanted to occur by settling in 3 hours. The percentage of water separation can be determined using Eq. (2) [18]:

$$\%\text{water separation} = \frac{\text{volume of seration water, ml}}{original\ volume\ of\ water\ in\ emulsion, ml} * 100 \qquad (2)$$

3. Results and discussions

Effect of demulsifier dosage: For the experimental part, 5 samples of emulsion oil with 10% water were prepared and treated with 1, 2, 3, 4, and 5% vol of demulsifier at room temperature (20°C). The samples, along with the demulsifier, were manually agitated 100 times to ensure thorough mixing. After agitation, the samples were left to stand for 48 hours to allow water separation by decantation. After decantation, the volume of separated water from each sample was measured (Fig. 2).

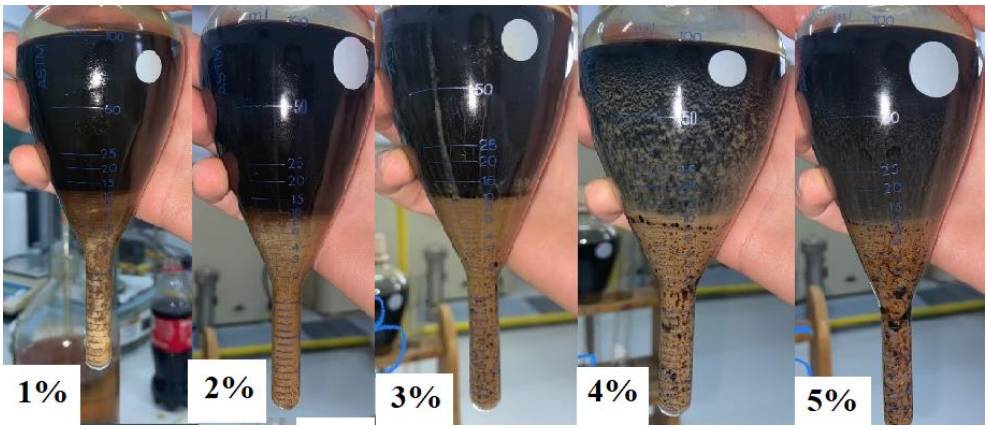

Fig.2. Water separation for different demulsification dosage: 1, 2, 3, 4 and 5%

In Fig.3, the percentage of water separation from each sample is represented based on the percentage content of demulsifier and the demulsification time. As can be seen from this figure, the volume of decanted water in the demulsification process increases with the increasing dosage of demulsifier in the samples. Additionally, it is observed that the water separation occurred more quickly as the demulsifier content of the sample was higher. As a result, after 35 minutes from adding the demulsifier, water separation was complete in all five samples.

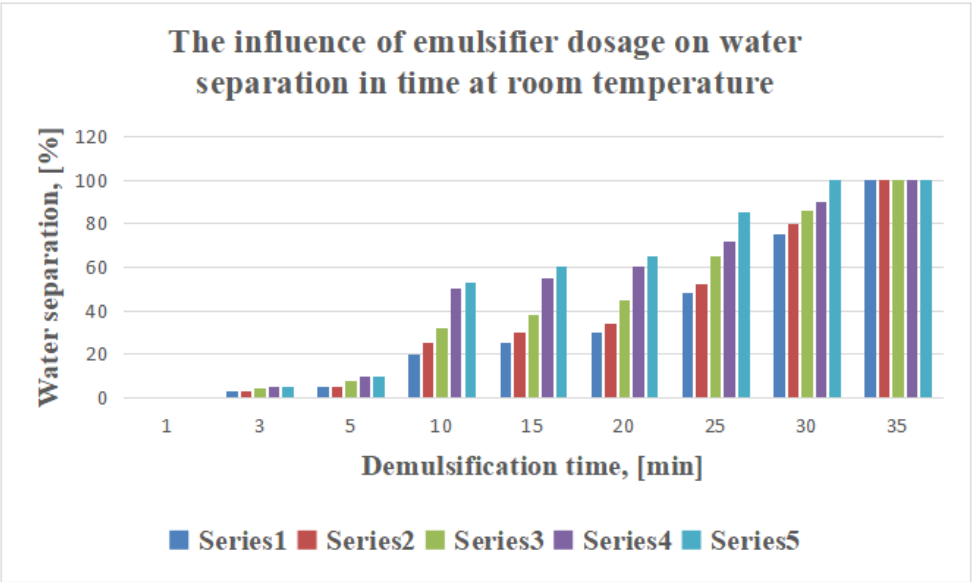

Fig.3. Variation of water separation percentage in time at different demulsification dosage: 1, 2, 3, 4 and 5%, at room temperature

Effect of temperature:

To study the influence of temperature on the demulsification process, 4 sets of 5 samples each were prepared similarly to the previous section, meaning each set of 5 samples of crude oil emulsion with 10% water was subsequently treated with 1, 2, 3, 4, and 5% demulsifier. This time, each set of 5 samples (with 1 - 5% demulsifier) was heated in a water bath at different temperatures, such as: 30, 40, 50, and 60°C. For each set, the amount of decanted water was measured over time. The results of the determinations are presented in Figs. 4 - 7. In these figures, it can be observed that with an increase in the demulsification temperature, the amount of decanted water increases and the separation time decreases, with separation occurring almost instantaneously at 60°C. Consequently, for a faster demulsification rate, a higher temperature is recommended, but not exceeding 60°C, as above this value there is a risk of losing the lighter fractions of crude oil through vaporisation.

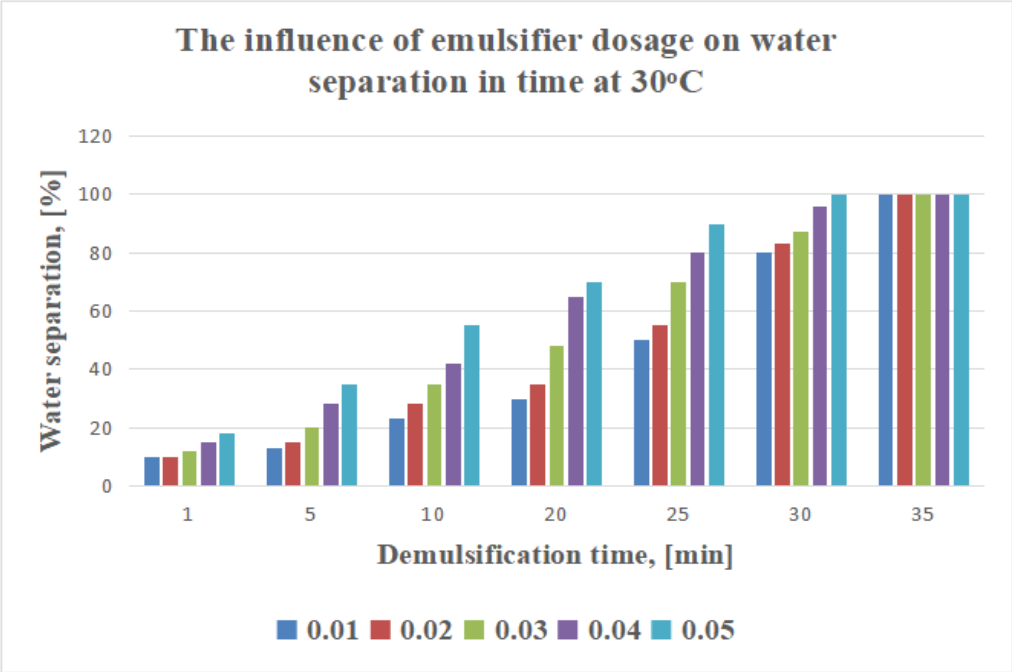

Fig.4. Water separation percentage in time at different demulsification dosage: 1, 2, 3, 4 and 5%, at 30°C

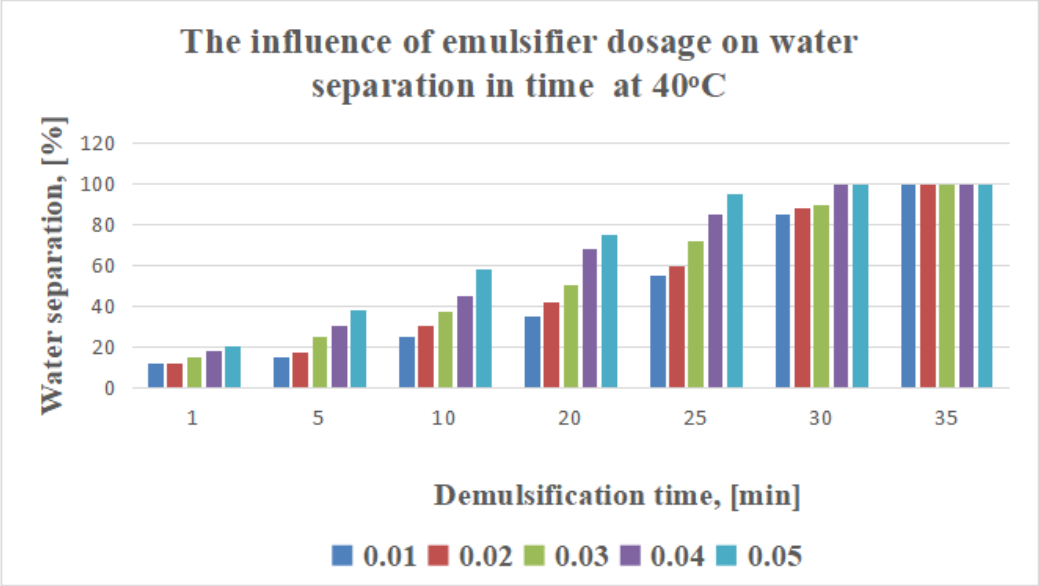

Fig.5. Water separation percentage in time at different demulsification dosage: 1, 2, 3, 4 and 5%, at 40°C

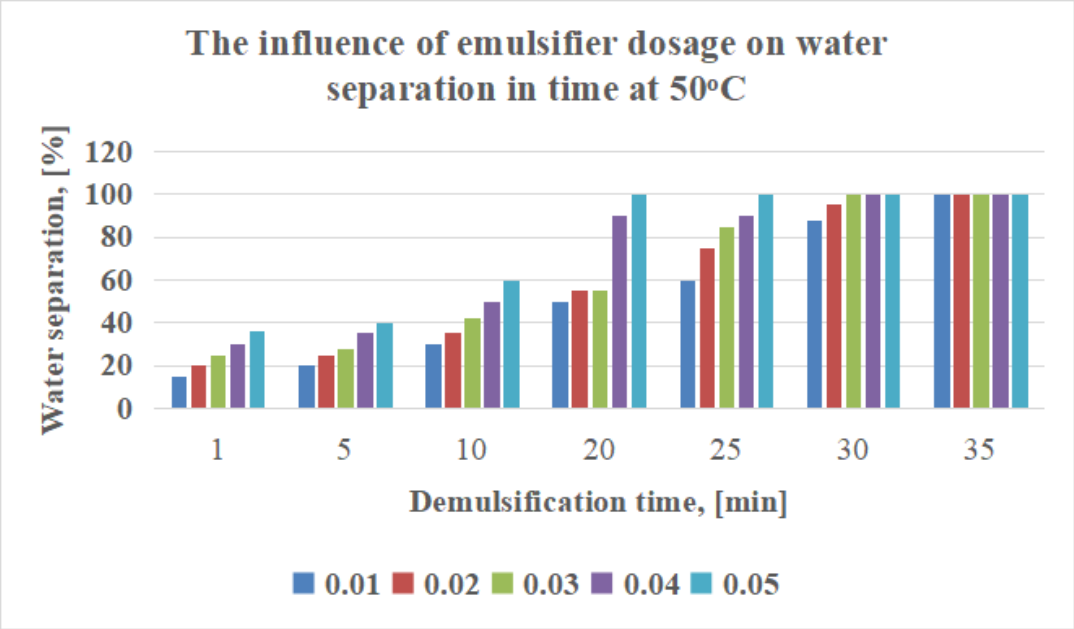

Fig.6. Water separation percentage in time at different demulsification dosage: 1, 2, 3, 4 and 5%, at 50°C

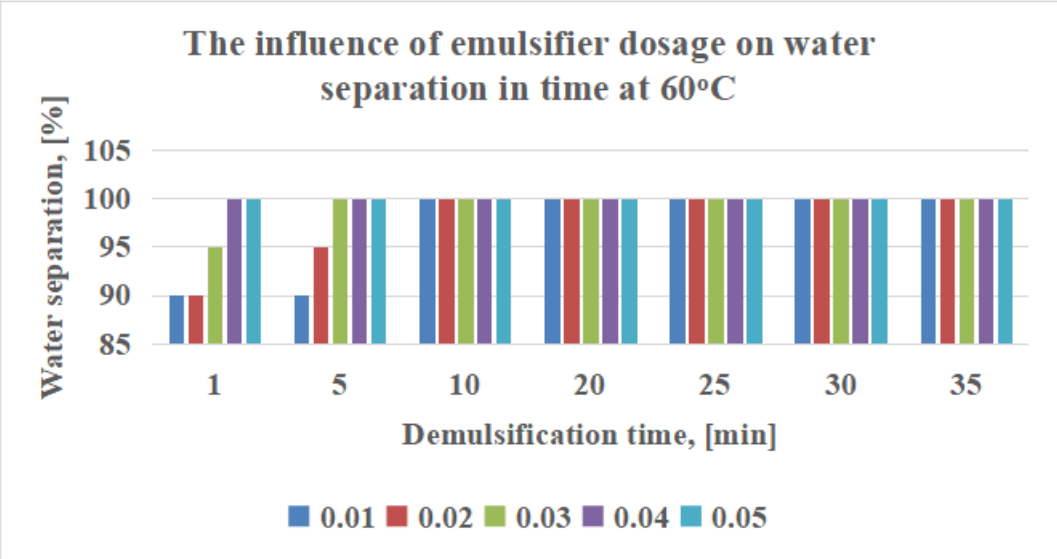

Fig.7. Water separation percentage in time at different demulsification dosage: 1, 2, 3, 4 and 5%, at 60°C

The favorable effect of increasing temperature on the demulsification process can also be explained due to the decrease in the viscosity of the continuous phase of the emulsion with the temperature increase. As a result, the mobility of water droplets will increase, leading to a higher possibility of their coalescence, and this will result in a increased rate of settling of the water formed by the coalescence of the droplets. Moreover, with the increase in temperature, the emulsifier films formed from the resins present in crude oil around the water droplets become less rigid and will break more easily, favoring their coalescence and increasing the amount of decanted water.

4. Conclusions

Crude oil typically contains waxes, resins, and asphaltenes which contribute to the formation of stable emulsions when mixed with water. The stability of the formed emulsion persists due to the presence of these emulsifiers at the interface between the dispersed water droplets and the continuous oil phase, preventing droplet coalescence. Such formed emulsions will have a negative impact on the petroleum processing industry.

This study aims to investigate the influence of factors such as demulsifier dosage and temperature on the demulsification process of crude oil. The demulsifier used in the process is a commercial one, used in petroleum industry consisting of a mixture of C9 aromatic hydrocarbons.

From the experimental study, the following observations were made:

- The most stable crude oil emulsion was the one with a 10% brine content. The others, with 15% and 20% content, separated after a while, approximately 3 and 5 hours respectively. Therefore, the 10% brine emulsion was chosen for the experimental study.
- The amount of separated water from the emulsion and the demulsification rate increase with the increase in demulsifier dosage in the demulsification process.
- With an increase in temperature, the demulsification rate and the amount of separated water from the emulsion also increase.
- Consequently, higher concentrations of demulsifier are recommended, within economic limits, and higher demulsification temperatures, but not exceeding 60°C, as above this value, the lighter fractions of oil can be lost.

Looking ahead, for future research, we aim to expand the study on the crude oil demulsification process by testing different environmentally friendly demulsifiers, such as coconut oil and certain vegetable oils.

REFERENCES

[1]. Saat M. A., Chin L. H. and Wong C. S. , Treatment of crude oil emulsion using coconut oil and its derivative as green demulsifiers, *Materials Today: Proceedings*, https://doi.org/10.1016/j.matpr.2020.01.253

[2]. Abed S. M., Abdurahman N. H., Yunus R. M., Abdulbari H. A., and Akbari S., ―Oil emulsions and the different recent demulsification techniques in the petroleum industry-A review,‖ IOP Conf. Ser. Mater. Sci. Eng., vol. 702, no. 1, (2019), 1–13, doi: 10.1088/1757-899X/702/1/012060

[3]. Raya S. A. , Mohd Saaid I. , Abbas Ahmed A. , and Abubakar Umar A. , ―A critical review of development and demulsification mechanisms of crude oil emulsion in the petroleum industry,‖ J. Pet. Explor. Prod. Technol., vol. 10, no. 4, (2020), 1711–1728, doi: 10.1007/s13202-020-00830-7.

[4]. FeitosaF. X., Alves R. S., and de Sant'Ana H. B., ―Synthesis and application of additives based on cardanol as demulsifier for water-in-oil emulsions, *Fuel*, vol. 245, no. September 2018, (2019), 21–28 doi: 10.1016/j.fuel.2019.02.081.

[5]. Hajivand P. and Vaziri A., Optimization of demulsifier formulation for separation of water from crude oil emulsions, *Brazilian Journal of Chemical Engineering*. 1, (2015), 107-118.

[6]. Saad M. A., Kamil M., Abdurahman N., Yunus R. M., and Awad O. I., An Overview of Recent Advances in State-of-the-Art Techniques in the Demulsification of Crude Oil Emulsions, *Processes*. 7. (2019). 470.

[7]. Lissant, K.J., *Demulsification-Industrial Application*, Surfactant Science Series, Vol. 13, Marcel Dekker, New York 1983.

[8]. Fingas M , Water-in-oil emulsion formation: a review of physics and mathematical modelling, Spill Sci. Technol. Bull. 2 (1) (1995) 55–59.
[9]. Zolfaghari R., Ahmadun Fakhru'l-Razi, Abdullah L.C., Elnashaie S.S.E.H., Pendashteh A., Demulsification techniques of water-in-oil and oil-in-water emulsions in petroleum industry, *Sep. Purif. Technol.* 170 (1) (2016) 377–407.
[10]. Kokal S., Crude oil emulsions: a state-of-the-art review, SPE Prod. Facil. 20(1), (2005), 5–13.
[11]. Zhang, Z. Q., Xu, G. Y., Wang, F., Dong, S. L., and Chen, Y. J. Demulsification by philippic dendrimer copolymers. *J. Colloid Interface Sci.* 282, (2005), 1–4.
[12]. Rajak, V. K., Relish, K. K., Kumar, S., Mandal, A., Mechanism and kinetics of separation of oil from oil-in-water emulsion by air flotation. *Pet. Sci. Technol.* 33, (2015), 1861–1868.
[13]. Liu, J. J., Engineering research on handling heavy aging oil with thermal chemical deposition and centrifugal separation. *Appl. Mech. Mater.* 448–453, (2014), 3058–3061.
[14]. Kumar, S., Guria, C., and Mandal, A. Synthesis, characterization and performance studies of polysulfone/bentonite nanoparticles mixed-matrix ultra-filtration membranes using oil field produced water. *Separ. Purif. Technol.* 150, (2015), 145– 158.
[15]. Bratskaya, S., Avramenko, V., Schwarz, S., and Philippova, I. Enhanced flocculation of oil-in-water emulsions by hydrophobically modified chitosan derivatives. *Colloids Surf. A*: *Physicochem. Eng. Aspects* 275, (2006), 168–176.
[16]. Falode O., Aduroja A., Christy O., Development of local demulsifier for water in-oil emulsion treatment, *Int. J. Sci.: Basic Appl. Res.* 24 (4531) (2015) 301– 320.
[17]. Mat H., Samsuri A., Rahman W.A., Aizan W., Othman N., Chieng Y.Y., Jong S.C., Zulkania A., Study on Demulsifier Formulation for Treating Malaysian Crude Oil Emulsion, Project Report, Universiti Teknologi Malaysia, Skudai, Malaysia, 2005.
[18]. Hajivand P., Vaziri A., Optimization for demulsifier formulation for separation of water from crude oil emulsions, *Braz. J. Chem. Eng.* 32 (1) (2015) 107–118.